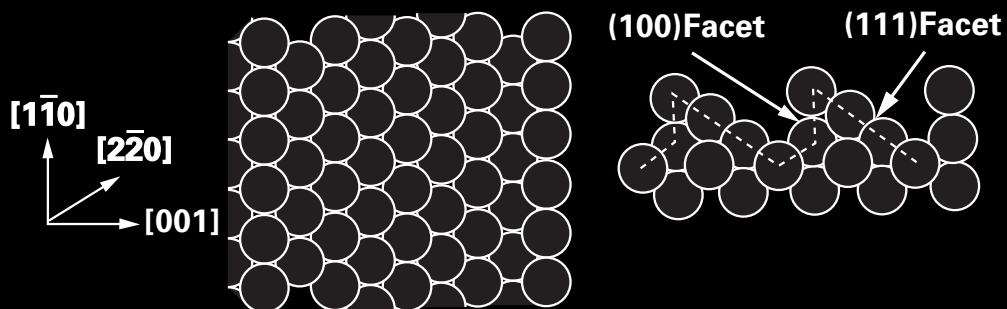


(110-1x2 Surface)



Study of Nanoparticles at UTSA: One Year of Using the First JEM-ARM200F Installed in USA

Alvaro Mayoral^{†,†††}, Rodrigo Esparza[†], Francis Leonard Deepak^{†,††}, Gilberto Casillas[†], Sergio Mejía-Rosales^{††††}, Arturo Ponce[†] and Miguel José-Yacamán[†]

[†] Department of Physics and Astronomy, University of Texas at San Antonio

^{††} International Iberian Nanotechnology Laboratory, Avda Mestre Jose Veiga

^{†††} Laboratorio de Microscopías Avanzadas (LMA), Instituto de Nanociencia de Aragón (INA), Universidad de Zaragoza, c/Mariano Esquillor, Edificio I+D

^{††††} Center for Innovation and Research in Engineering and Technology, and CICFIM-Facultad de Ciencias Físico-Matemáticas, Universidad Autónoma de Nuevo León

Contents

Study of Nanoparticles at UTSA: One Year of Using the First JEM-ARM200F Installed in USA	1
Exploring Biological Samples in 3D Beyond Classic Electron Tomography . . .	6
Application of Scanning Electron Microscope to Dislocation Imaging in Steel	11
Atmospheric Scanning Electron Microscopy (ASEM) Realizes Direct EM-OM Linkage in Solution: Aqueous Immuno-Cytochemistry	17
Information Derived from PGSE-NMR ~Ion Diffusion Behavior, Molecular Association, Molecular Weight/Composition Correlation of Synthetic Polymers~	23
Development of JEM-2800 High Throughput Electron Microscope.	31
Introduction of New Products	37

Cover micrograph

HAADF-STEM image of a gold decahedral particle oriented near a five-fold axis. Around the particle a cobalt oxide layer is growing. One of the (110) facets of the nanoparticles shows the 1×2 surface reconstruction corresponding to a missing atom row. Cobalt atoms occupy the empty gold atom positions. This is probably one of the best examples of epitaxial growth. (See page 5)

The first results from our group that have been obtained using the newly installed aberration-corrected STEM microscope (JEOL JEM-ARM200F) are reported. Studies were carried out on noble metal nanoparticles and their corresponding alloys and/or core-shell structures. In this paper we focus on some of the exciting areas of research that have been under investigation in our group. These include studies on Au nanoparticles, bimetallic Au-Co nanoparticles and core-shell Au-Pd nanoparticles. In addition, studies that were carried out on very small clusters namely Pd-Ir and other similar systems have also been highlighted in this report.

Introduction

The University of Texas at San Antonio organized recently an Electron Microscopy core facility named the "Kleberg Advanced Microscopy Facility". The most relevant instrument is a JEOL JEM-ARM200F (with FEG) with probe aberration correction; this instrument was the first one installed outside Japan and is operational since February 2010. In this paper we report some of the results after one year of its operation.

Experimental

For the electron microscopy analysis, the nanoparticles samples were dispersed in ethanol and a drop of this suspension was deposited onto a holey carbon grid. The samples were characterized using the aberration (C_s) corrected JEOL JEM-ARM200F (ARM) 200 kV FEG-STEM/TEM, equipped with a CEOS C_s corrector on the illumination system. The probe correction was performed through a dodecapole corrector (CEOS GmbH) aligned through the

CESCOR software, to finally obtain a twelve-fold Ronchigram with a flat area of 50 mrad. The pixel spacing was calibrated using Si [110] lattice images in the HAADF mode, and confirmed by using gold standard particles. Images were commonly recorded for 10 to 16 s. The probe current used for acquiring the HAADF as well as the BF-STEM images was 9C (23.2 pA) and the CL aperture size was 40 μm . High angle annular dark-field (HAADF) STEM images were acquired with a camera length of 8 cm/6 cm and the collection angle of 50-180 mrad/67-250 mrad was used. The BF-STEM images were obtained using a 3 mm/1 mm aperture and a collection angle of 11 mrad/3.8 mrad was used (camera length in this case was 8 cm). The HAADF as well as the BF images were acquired using a digiscan camera. In order to reduce the noise of the images and to obtain clearer images the raw data was filtered using the 2D Wiener filter and the Richardson-Lucy/Maximum Entropy algorithm implemented by Ishizuka. The EDS analysis was performed using EDAX instrumentation attached to the JEOL-ARM microscope. Spectra, line scans as well as chemical maps for the various elements were obtained using the EDAX Genesis software. For the EDS analysis the probe size used was 6C (145 pA) and the CL aperture size was 40 μm . One- and two-dimensional elec-

One UTSA Circle, San Antonio, Texas 78249, USA

miguel.yacaman@utsa.edu



tron energy loss spectroscopy (EELS) analysis was performed with a GIF-Tridiem spectrometer. The probe size used was 6C (145 pA) and the CL aperture size was 40 μm (camera length – 6 cm).

Results and Discussion

Monometallic nanoparticles

Nanoparticles are a fundamental part of nanotechnology. In fact, metal nanoparticles were used since the 1940's to improve the quality of gasoline. The surprisingly high catalytic activity of particles in the nano size range was recognized early and hence it was used extensively [1]. However, for many years it was assumed that the only role of the particles was to provide a higher surface area. The recent explosion of interest in nanotechnology has made clear the fundamental physical principles behind the particle behavior. The nanoparticles are intermediate between clusters (a few atoms) and bulk systems. In fact clusters are different from nanoparticles in the fact that most of the atoms are on the surface. In a particle although an important fraction of the atoms are on the surface there is still a core of non-surface atoms.

The use of HAADF-STEM has opened up new and exciting possibilities to understand nanoparticles. The atomically resolved images in combination with EDS and EELS data provide a very powerful set of tools capable of understanding the atomic behavior.

One of the most common findings in nanoparticles is that the crystal structure is different from that of the bulk. The most commonly observed case is the formation of the five fold symmetry structures such as the icosahedron and decahedron [2-4]. A very fundamental problem is to understand how these structures become stable. **Fig. 1** shows

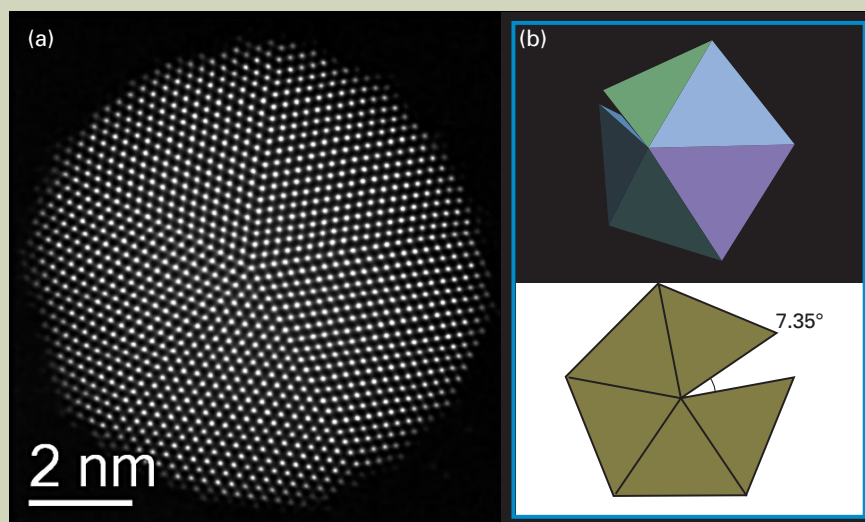


Fig. 1 (a) Au decahedra oriented along the 5-fold axis of the particle, (b) geometry angular deficiency in the decahedra. For a decahedron, the angle between adjacent (111) plane is 7.35° on projection of (110) orientation.

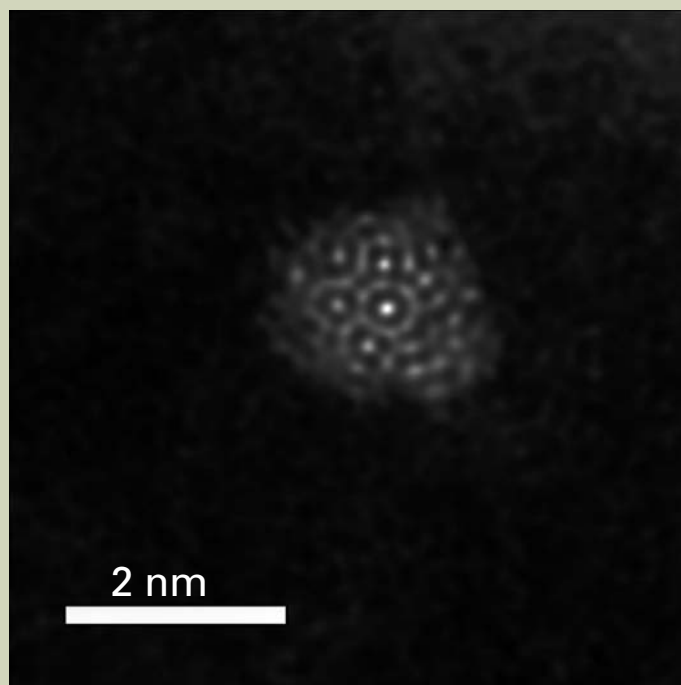


Fig. 2 The smallest icosahedra observed so far in which the five-fold symmetry is apparent.

an example of a gold decahedral particle in which the atomic columns are revealed by the HAADF-STEM image. A periodic strain can be observed along the one of the twin boundaries and this is related to the fact that if we pack five fcc regular tetrahedra in a cyclic twinning (see Fig. 1b) a gap of $7^\circ 35'$ will be produced. The strain on the particle will be necessary to accommodate the gap. It is possible from images of this kind, to measure the strain more accurately. In **Fig. 2**, we show one of the smallest icosahedra so far observed in which the fivefold symmetry is apparent.

Bimetallic nanoparticles

The properties of metallic nanoparticles can be improved by adding a second metal [5].

Indeed many of the most useful nanoparticles are bimetallic, one important problem is to determine its detailed structure and chemical composition. In our group since the last few years we have been carrying out a very extensive research program on bimetallic nanoparticles. We have studied a number of systems including Au/Pd, Au/Co, Au/Pt, Pd/Pt and Au/Ag among many others. Normally it is assumed [2] that nanoparticles with two metals will show a structure which is either core-shell or an alloy. In the first case, one metal will be the core and the second metal will be the shell surrounding the core. However experimental results from our group clearly indicate [6, 7] that the structure is much more complex, than a simple alloy or core shell structure. We will describe these details in the following sections.

Z contrast

When studying nanomaterials with two different elements, the most interesting case being those of transition and noble metals, the TEM techniques are somewhat limited since the contrast is more related to coherent scattering. Thus one of the major limitations is the diffraction contrast which will be easily observed (if present). Bright field images might give some information if there is strain or change of orientation between the core and shell structure. However, STEM-HAADF is the most important technique in the study of bimetallic nanoparticles. The intensity of the signal which is generated

will be proportional to the atomic number and the contrast due to the atomic composition will be clearly observed. In order to illustrate this effect we have made calculation of the intensity of columns of atoms of different elements with the same number of atoms. We have carried out multislice calculations using the software developed by HREM Inc.[8] The results are shown in **Figs. 3(a)** and (b). We have plotted a relative contrast of a number of elements where the Z contrast is apparent. On the other hand the intensity goes as $I \sim Z^{1.45}$. With the probe corrected aberration a resolution of 0.8 Å can be achieved therefore variations of the composition at atomic scale can be observed.

Experimental examples of bimetallic particles

When applied to real nanoparticles that have been obtained in our laboratory, the atomic contrast is clearly observed. **Fig. 4** (a) and (b) shows an Au/Pd nanoparticle grown by chemical synthesis (6). The variation in the composition is clearly observed (Fig.4(b)), the central core is an alloy rich in Pd, then a second layer of alloy rich in gold and finally a exterior shell which is an alloy rich on Pd. It is possible to plot the chemical composition along the particle using EDS and EELS, the result of which is shown in **Fig. 5** and **Fig.6**. EDS line scan in the case of the three-layer Pd-Au-Pd nanoparticles

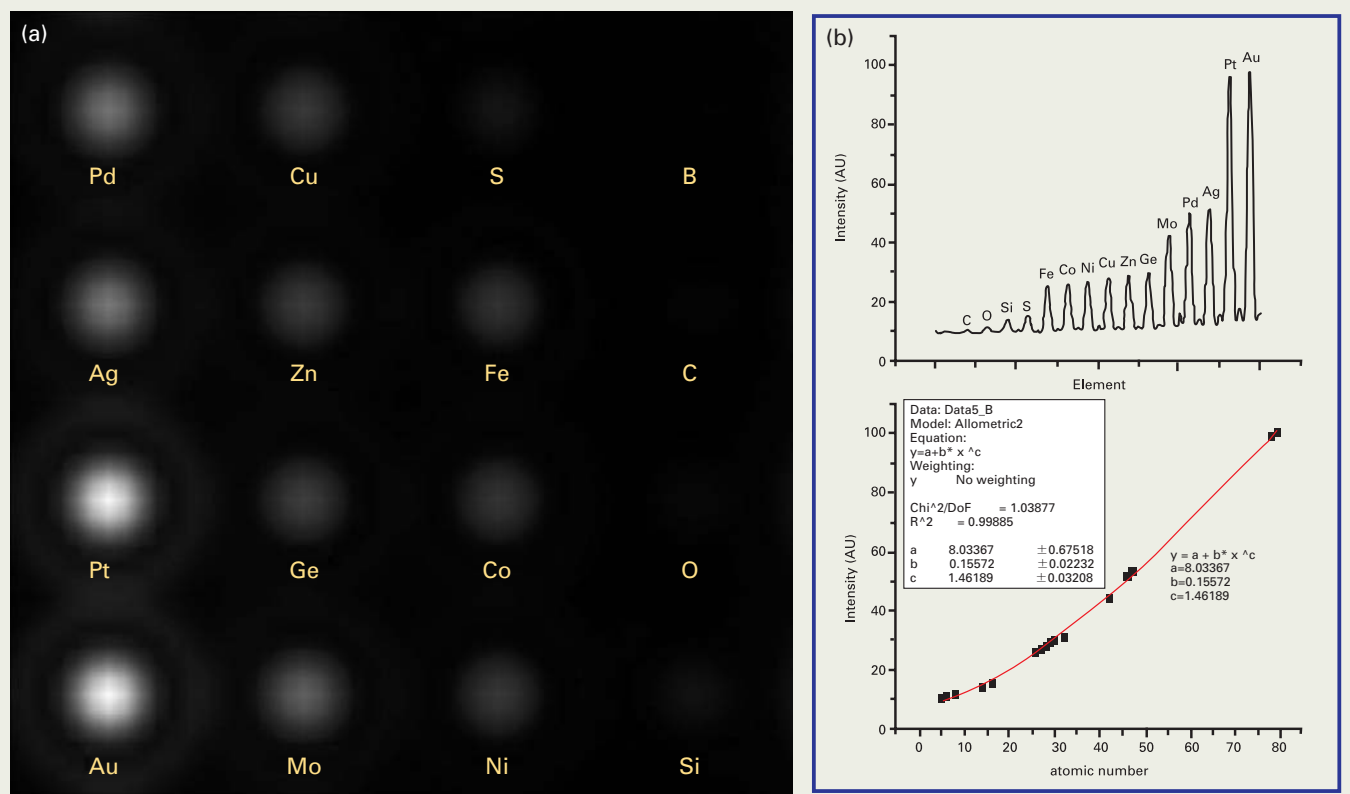


Fig. 3 (a) Calculations of the relative HAADF-STEM contrast of different elements (columns with the same number of atoms). The atomic number contrast is very clear, (b) Variation of the intensity of the contrast with the atomic number.

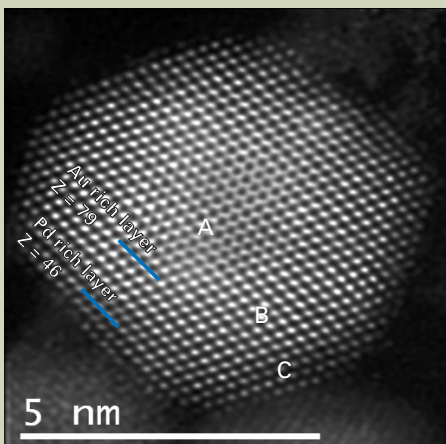


Fig.4 A truncated cuboctahedra three-layered (Pd-Au-Pd) nanoparticle.

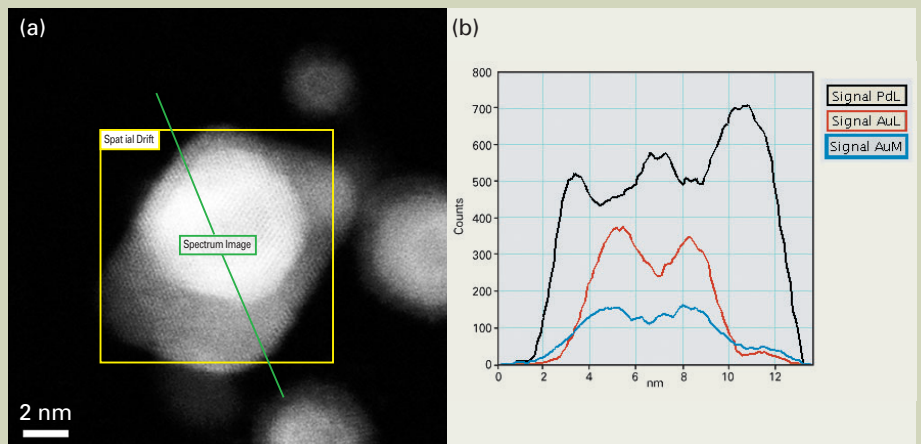


Fig. 5 (a) and (b) Characterization of the Au and Pd elemental distribution across the nanoparticle by STEM-EDS line-scanning technique across the individual three-layer nanoparticle. The Pd-L and the Au-L,M line scan signals can be clearly seen varying in intensity along the different regions of the nanoparticles. (a) Shows the analyzed area and the direction of analysis.

reveal the following interesting features as can be seen in Fig. 5. The Pd-L and the Au-L,M signals can be clearly traced across the region of the individual Pd and Au layers with the maximum intensity of the signals varying between the respective layers (Fig. 5(b)). The corresponding EELS map of Pd reveals clearly the presence of Pd in the core and in the outermost shell of the tri-layered nanoparticles as is shown in Fig. 6. These results clearly confirm the complex chemical nature of the bimetallic particles. In addition it is possible even to distinguish layer by layer, when it is Pd rich or Au rich as shown in Fig. 7. Thus it is worthy to mention that in case of these nanoparticles occasionally four-layered structure are seen.

Shown in Fig. 7, is the case of the four layered nanoparticles wherein it can be seen that near the surface there is an extra layer of atoms of gold and this suggests a four layered structure. This is a different case from the previously mentioned three-layered nanoparticles and has not been reported till date.

A very interesting result is shown in Fig. 8, wherein two Au/Pd particles that have coalesced are forming an elongated structure. Most remarkably the 3 layer structure is preserved by the coalescence. This means that during the initial coalescence process the Pd atoms diffuse along the boundary. However many bright spots, corresponding to gold atoms can be observed on the region common

to the two particles.

Surface reconstruction in nanoparticles

One of the most interesting discoveries of the surface science research back in the seventies was that, the surfaces of crystals can have a different atomic arrangement than those of the bulk [9]. This phenomenon is known as surface reconstruction and in the mid 80's Marks *et al.* [10] showed that indeed surface reconstruction is also observed in gold nanoparticles. In our group we have been investigating the conditions in which surface reconstruction appears. We have observed inter-

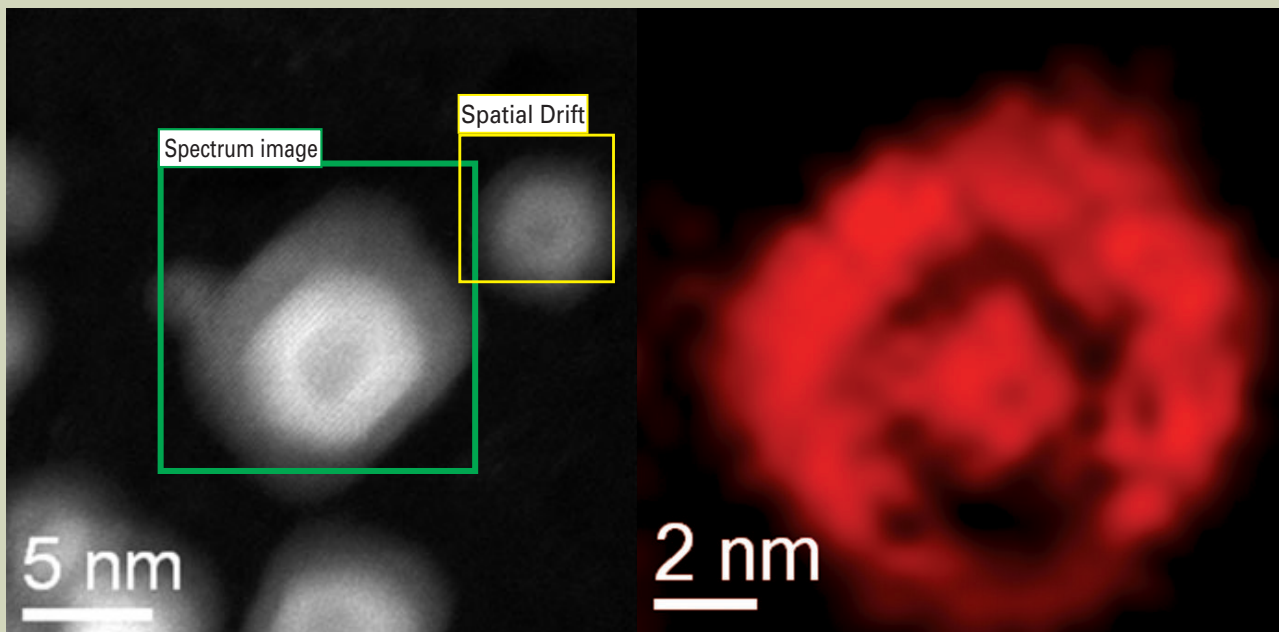


Fig. 6 EELS map of Pd reveals clearly the presence of Pd in the core and in the outermost shell of the tri-layered nanoparticles.

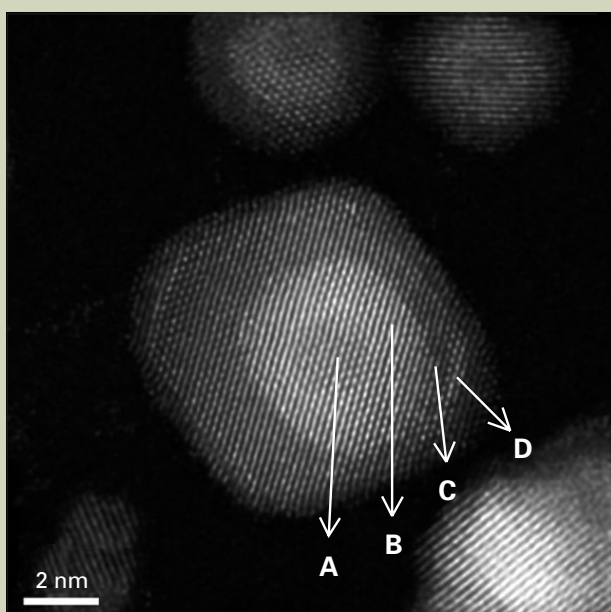


Fig. 7 Aberration-corrected STEM images of the four layered Au/Pd nanoparticles. The contrast of the four distinct regions (marked A, B, C and D) can be clearly seen.

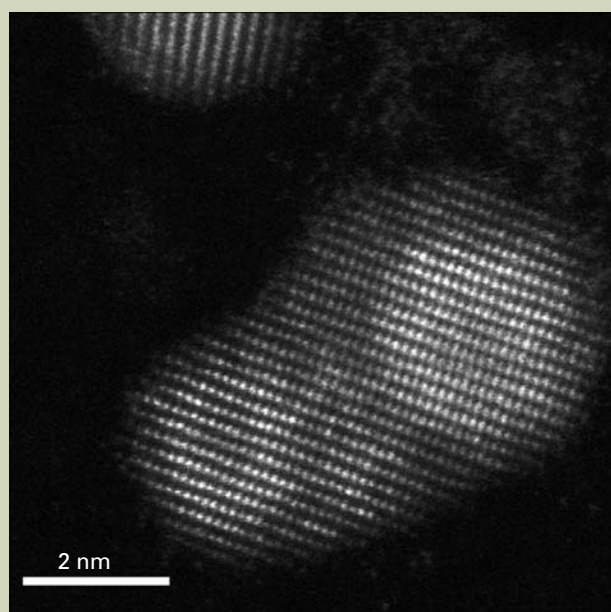


Fig. 8 Coalescence of two/three-layered Pd-Au-Pd nanoparticles. Notice also the Au intercalation into the Pd layer.

faces of Au with Co. Shown in **Fig. 9** (a) is the $\langle 110 \rangle$ surface of a Au/Co nanoparticle. The bright atoms correspond to gold and the light atoms correspond to Co. It can be observed that gold shows a (1×2) reconstruction. A model of the reconstructed surface in the missing row is shown in Fig. 9(b) (compare the image Fig. 9a and the model Fig. 9b). The interesting result is that 10 atoms accommodate on the places of the missing gold atoms. This kind of analysis suggests ways in which surfaces can be tailored for improved catalytic activity.

Observation of individual atoms/clusters

It is indeed interesting to note that the ultimate resolution of observing individual atoms/small clusters have been achieved using the ARM. Shown in **Fig. 10**, are the very small clusters of Pd-Ir (inside the circle). The size of the cluster is just about ~ 2 nm. It is interesting to note that based on the Z contrast, the two different atoms can be distinguished very clearly (Pd, $Z = 46$, Ir = 77). In addition in the vicinity of these small clusters it is also possible to locate individual atoms of Ir/Pd (outside the circle).

Conclusions

This paper summarizes the most important results on noble metal nanoparticles obtained

from our group over the last year with the new ARM microscope. It is clear from the discussion provided, on the results that have been obtained concerning metal nanoparticles/bimetallic and core-shell nanoparticles and other related systems, that it has indeed been an exciting one year. With unprecedented advantages in terms of resolution and using the HAADF-STEM imaging in combination with additional spectroscopic tools associated with it, namely EDS and EELS it has been possible to unravel some of the fundamental questions in the case of nanoparticles. Indeed with all these new developments, we can look forward to many such more exciting areas of research in the coming years.

Acknowledgements

The authors would like to acknowledge THE WELCH FOUNDATION AGENCY PROJECT # AX-1615. "Controlling the Shape and Particles Using Wet Chemistry Methods and Its Application to Synthesis of Hollow Bimetallic Nanostructures". The authors would also like to acknowledge the NSF PREM Grant # DMR 0934218, Title: Oxide and Metal Nanoparticles - The Interface between life sciences and physical sciences. The authors would also like to acknowledge RCM Center for Interdisciplinary Health Research CIHR. The project described was supported by Award Number

2G12RR013646-11 from the National Center for Research Resources. The content is solely the responsibility of the authors and does not necessarily represent the official views of the National Center for Research Resources of the National Institutes of Health. Finally, the authors would like to thank Dr. Eduardo Pérez-Tijerina from UANL for providing of some of the samples included in this paper.

References

- [1] G. Somorjai, *Chem. Rev.*, **96**, 1223 (1996).
- [2] A. L. Mackay, *Acta Crystallogr.*, **15**, 916 (1962).
- [3] J. L. Rodriguez-Lopez, J. M. Montejano-Carrizales, M. Jose-Yacaman, *Modern Physics Letters*, **20**, 725 (2006).
- [4] L. D. Marks, *Reports on Progress in Physics*, **57**, 603 (1994).
- [5] R. Ferrando, J. Jellinek, R. L. Johnston, *Chem. Rev.*, **108**, 845 (2008).
- [6] D. Ferrer, D. A. Blom, L. F. Allard, *J. Mat. Chem.*, **18**, 2442 (2008).
- [7] D. Ferrer, A. Torres-Castro, X. Gao et al. *Nano Lett.*, **7**, 1701, 2007.
- [8] K. Ishizuka, N. Uyeda, *Acta Cryst. A*, **33**, 740 (1977).
- [9] H. Wagner. *Springer Tracts in Modern Physics (Springer, Berlin)*, **85**, (1979).
- [10] L. D. Marks, *Phys. Rev. Lett.*, **51**, 1000 (1983).

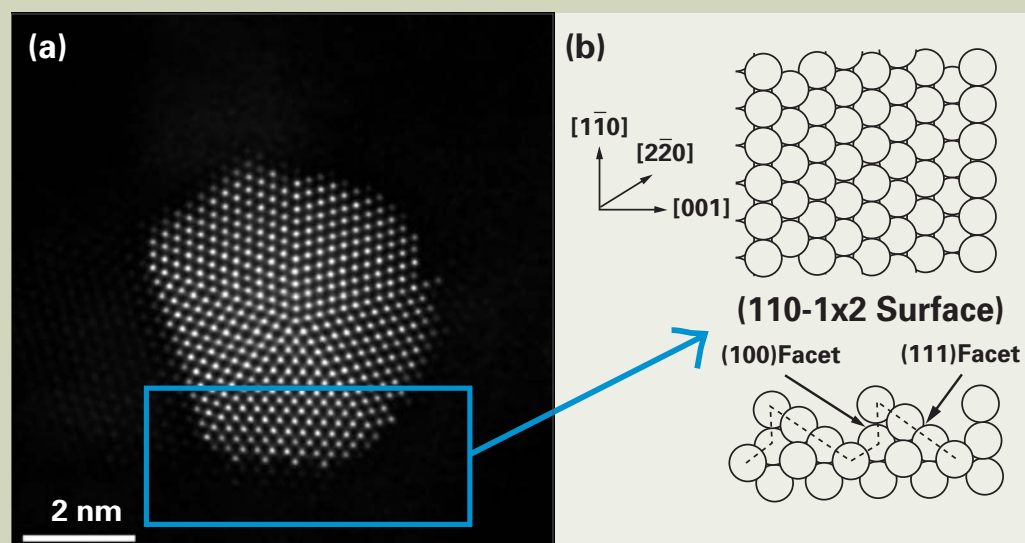


Fig. 9 (a) Image of surface reconstruction observed in Au-Co nanoparticles and (b) the corresponding model showing the 1×2 reconstruction.

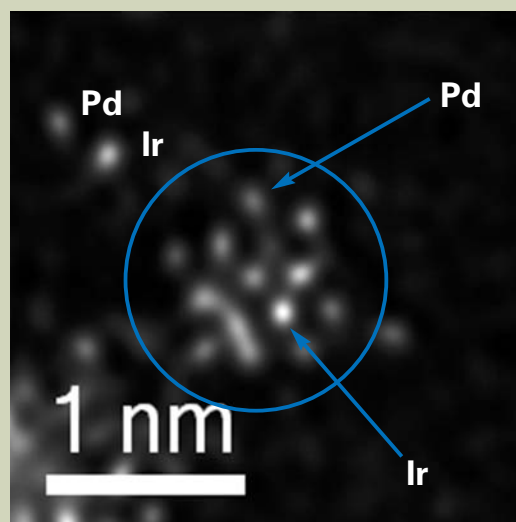


Fig. 10 Clusters of Pd-Ir are shown (inside the circle). It is possible to distinguish each element based on the Z contrast (Pd = 46, Ir = 77). Notice also the presence of individual atoms (outside and close to the circle).

Exploring Biological Samples in 3D Beyond Classic Electron Tomography

Marcel Cunha, Cédric Messaoudi and Sergio Marco

Institut Curie, Centre de Recherche and INSERM

Developments of electron tomography methods are of great importance to unravel the tridimensional organization and the interior detail of objects of nanometric scale. Here we describe two recently developed approaches to surpass some of the milestones of contemporary electron tomography: The low signal to noise ratio of tomograms and the detection of chemical elements in 3D. The techniques applied rely on STEM tomography and EFTEM tomography, capabilities of the 200kV electron microscope JEOL JEM-2200FS equipped with an in-column energy filter and STEM detectors. In the resin embedded samples tested, STEM-HAADF tomography was applied with success to improve the signal to noise ratio and determine cytoskeletal structures on mammalian kidney cells (LLC-PK1). For elemental detection, EFTEM tomography revealed the precise location and 3D arrangement of iron particles bound to cell wall of the pathogenic fungus *Fonsecaea pedrosoi*. Both techniques resulted in datasets clear enough for direct interpretation and threshold-based segmentation.

Introduction

Imaging techniques of tridimensional reconstructions provide details of the interior of reconstructed objects otherwise inaccessible. Such methods allow the quantification of volumes and might give access to the information of the different elements constituting the object. They are used in many fields such as archeology, geophysics, material sciences, quality control and biology. In medicine, these methods represented by X-ray tomography [1], single photon emission computed tomography [2], magnetic resonance imaging [3] or positron emission tomography [4] are regularly used for exploration and diagnosis. In cell biology, volume reconstruction methods provide a more accurate vision of the relationships between cellular structures

and organelles leading to a better understanding of life processes [5]. Thus, methods to obtain 3D information of objects are nowadays indispensable for large aspects of modern science.

3D reconstruction methods are usually based on the stacking of images obtained from sections of the studied object or on the combination of data from its projections. The electron microscopy techniques available nowadays which use the first approach are destructive to the specimen, since they are based on the progressive slicing by knives or by sample erosion by an ion beam. The second approach, used for electron tomography, is based on the analysis of the projections of a thick specimen (from 100 to 1000 nanometers), which is preserved and could be used for successive and complementary analyses. This is one reason that makes approaches based on reconstruction techniques from projections largely favored. These methods require image formation by the use of any kind of penetrat-

ing wave generated by a tomograph which also records the projected images [6]. To study samples at nanometric scale, the transmission electron microscope (TEM) is presently the most used tomograph although other alternatives are slowly being applied to life sciences, such as those based on synchrotron radiation [7]. Volume reconstructions methods based on the combination of TEM images acquired from a single specimen tilted at different angles are called transmission electron tomography (TET) [8]. The automation of image acquisition using TEMs started a quarter of century ago and was perfected more recently with the use of fast computers and sensitive and larger digital cameras sensors. This enabled TET as a routine in a reasonable number of well-equipped electron microscopy laboratories. In biology, TET has recently been combined with cryo-fixation methods [9,10] consisting in the freezing of samples at speed, pressure and temperature conditions to reach a quality of ice

U759 Orsay, F-91405 France

sergio.marco@curie.fr

known as the vitreous state of the water. Since cells are mainly composed by water, its non-crystalline vitreous state formation by cryo-fixation allows a preservation of cellular structures in a close-to-native state. Cryo-fixation can then be followed by a replacement of water for resins (cryo-substitution) or by direct observation of the sample into the electron microscope at liquid nitrogen or lower temperatures (cryo-electron microscopy and cryo-electron tomography when combined with electron tomography). Cryo-electron tomography (CET) [11] is one of the most informative 3D approaches in structural cell biology, despite its limitations on sample size and resolution, which is approximately 5 nm for most used TET conditions, is currently becoming more and more popular among biologists, but it is still far from being widely used in biology labs.

In parallel to the development of CET, other electron tomographic approaches, valid for both resin embedded biological specimens and material sciences samples, are in progress. For this, the two main challenges are: (I) to increase the quality (resolution and signal-to-noise ratio) of the 3D reconstructions; and (II) to get 3D chemical distribution of elements. The first is considerably important to define small cellular structures like cytoskeletal filaments and other protein-made supramolecular structures and its subunits without the need to isolate such from the cellular environment. The latter is becoming increasingly interesting for biologist to help to unravel the role of elements (e.g. Iron, phosphorous) related to its location in the cell and its association with other cellular structures or organelles.

The improvement of the TET approaches in resin embedded samples goes presently through its combination with Scanning Transmission Electron Microscopy in its different modes (STEM-BF, ADF or HAADF) [12] allowing the enhancement of the signal-to-noise ratio of the projections; and also through its combination with Energy filtered TEM (EFTEM) to go further than the structural information by obtaining 3D chemical maps. STEM and EFTEM are frequently used in material sciences [13] but they are less common in the study of biological specimens. In this manuscript, we illustrate the potential that combining these two imaging modes with electron tomography has in biology by two examples consisting in the visualization of cytoskeleton elements in mammalian cells and the iron localization around a fungal cell wall.

The cytoskeleton [14] is not only the cellular scaffold, but also plays essential roles in a series of cellular phenomena like cellular division, cell growth, movement and intracellular transport of organelles. In eukaryotic cells, the cytoskeleton contains three main kinds of filaments: (I) actin filaments, constituted by double helix of 7 nm of diameter; (II) intermediate filaments, having about 10 nm of diameter; and (III) microtubules, which are cylinders of about 25 nm diameter. A high number of contemporary questions regarding the above cited phenomena are related to the precise determination of cytoskeleton structures in cell

and the relation of its tridimensional structure with nearby organelles or associated proteins.

Cellular structures are not only related to the cellular constitution and maintenance but also to interaction with other cells, from the same or other organism. The interaction between different organisms may result in growth of one in detriment of the other designing infection. The virulence of pathogenic fungi depends on several factors, and an important one is the presence of a pigment named melanin, mostly located on the fungal cell wall, providing strength and shape to the cell and related to resistance of antifungal treatments [15,16]. Since melanin interacts with iron forms, its spatial localization can be tackled by studying the 3D distribution of iron exogenously added via cationized ferritin. This requires the computation of 3D maps of iron by EFTEM tomography (EFTET).

Experimental, Results and Discussion, etc.

Data acquisition and image analysis

Images were acquired on a JEOL JEM-2200FS equipped with an in-column energy filter and a ssCCD 2k × 2k Gatan camera. For standard TET, Z-loss tilted series were acquired using an energy window of 10 eV. In the case of STEM-HAADF tomography images were recorded via JEOL's TEMography software suite for STEM. For EFTEM tomography tilt series at 0, 20, 560, 590, 620, 650, 680 and 710 eV were acquired also with JEOL's acquisition software suite. Image alignment was performed using Etomo [17,18] and TomoJ [19,20] depending on the addition or not of fiducial markers (5nm gold beads). 3D reconstructions were performed in Etomo or TomoJ using WBP or ART algorithms respectively both using a GPU accelerated implementation. For EFTET, background subtraction and image reconstruction were performed after multivariate analysis using an ImageJ plug-in developed by our group (unpublished software).

Comparison between standard TET and STEM-HAADF tomography

Brush border microvilli cells derived from proximal tubule of porcine kidney epithelium (LLC-PK1) were used for visualization of cytoskeleton elements by STEM and STET. A standard procedure consisting to fix samples with phalloidin and aldehydes, post-fix with tannic acid and osmium (TOTO), dehydrate and embedding in epon resin was applied before obtaining 100 nm thick sections.

Since contrast in STEM-HAADF is directly related to the atomic number of the elements present in the sample (Z-contrast image), this imaging mode is able to produce data presenting higher signal-to-noise ratio than standard TEM in stained biological

samples (Figure 1A,B). However, in most of 2D studies performed in stained biological samples, the SNR improvement does not justify the use of STEM. For instance, in our data set, different components of the cytoskeleton such as microtubules or actin could be identified in both cases. In addition, for an equivalent surface, the acquisition time required to record STEM images is larger than that required in standard TEM mode. Nevertheless, the SNR enhancement that can be achieved by STEM-HAADF is useful to improve 3D reconstructions computed by electron tomography because it improves image alignment (without fiducial markers) and leads to less noisy reconstructions allowing a reliable and reproductive volume interpretation.

The setup of STEM-HAADF tomography is becoming more user friendly with the new suites of software for the handling of the microscope as well as for the steps of calibration of acquisition parameters and focusing. STEM images suppose that all the points of the sample are placed at the same focal plane during the scanning. This condition does not occur during tomographic acquisition due to sample tilting, which implies a significant focus difference between the upper and the lower region of the specimen in the perpendicular direction to the tilt axis. These focus variations should be dynamically corrected, line by line, by the acquisition software [21]. The dynamic correction of focus, area by area, results in STEM-HAADF tomographic tilt series in which all the points in all the images have been acquired in focus. This, together with SNR improvement, leads to final reconstructions in which the stained biological objects are more contrasted in STEM-HAADF tomography than in standard TET, as they appear as white objects against an uniform dark background (Figure 1C,D). Therefore, the reconstructed volumes are suitable for objective segmentation methods such as thresholding [22] which, instead of relying on the subjective manual tracing of contour lines, are based in the assignation of colors or grey levels as function of the voxel values (Figure 2).

EFTEM tomography

Fonsecaea pedrosoi cells from 5-day old cultures were filtered in a 40–60G porous plate filter followed by centrifugation (13,600g, 30 min, 4°C) to isolate the conidial forms. Fungal conidia were fixed with 2.5% glutaraldehyde in PBS, exhaustively rinsed with PBS, and incubated in the presence of 10 µg/mL cationized ferritin, at pH 7.2, for 1 h at room temperature. Cells were postfixed for 30 min in 1% osmium tetroxide, dehydrated in acetone, and embedded in Epon [23]. 150 nm thick sections were used for observations under the electron microscope by TET and in EFTET.

The main advantage of EFTET is that it complements the structural information obtained by standard TET by providing the 3D localization of studied chemical elements. Therefore the process today is almost fully automatized, one drawback in

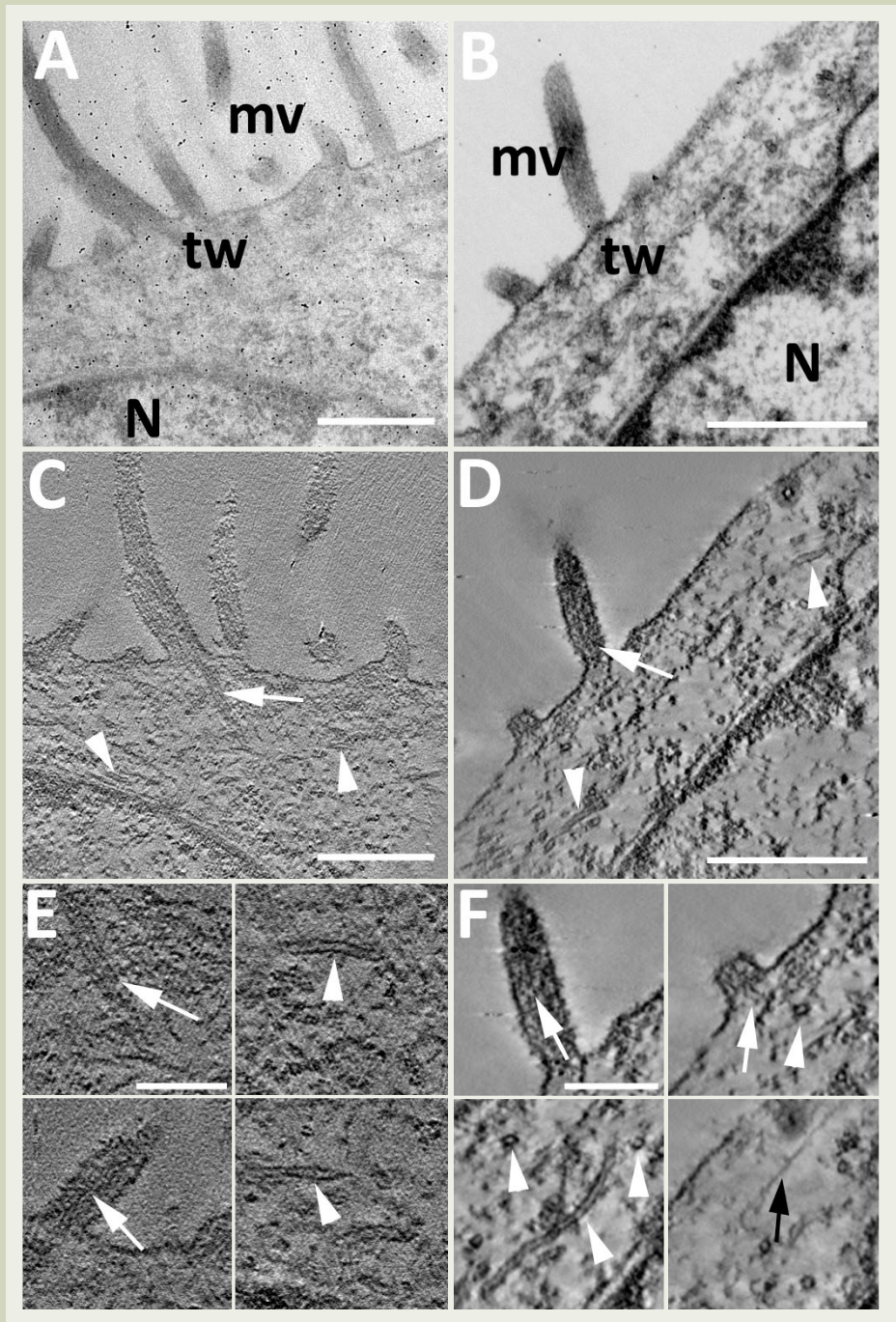


Fig. 1 Comparison between TET and STEM-HAADF tomography. A) 0° tilt image TEM; B) 0° tilt image STEM in a similar region of the same sample from the cell shown in (A). C) Virtual section extracted from TET tomogram computed from tilt series corresponding to (A). D) Virtual section extracted from STEM-HAADF tomogram computed from the tilt series corresponding to (B). E) Virtual cropped sections of areas of interest from (A). F) Virtual cropped sections of areas of interest from (B). N=nucleus, tw= terminal web, mv=microvilli. White arrow=actin filament; white arrowhead=microtubules; black arrows=intermediate filaments. Scale bars: A-D 500 nm, E-F 200 nm.

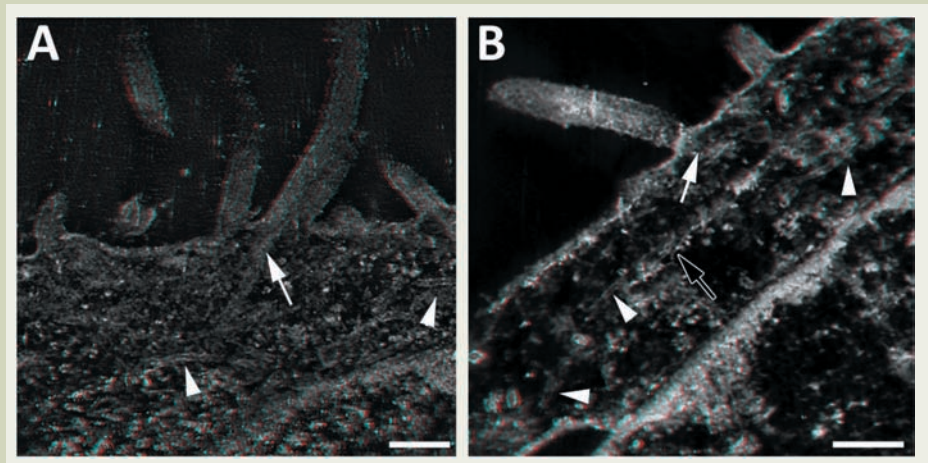


Fig. 2 Anaglyph from threshold segmentation TET and STET. White arrow=actin filament; white arrowhead=microtubules; black arrows=intermediate filaments. Scale bars 200 nm. Require red-cyan anaglyph glasses.

EFTET is that acquisition is time consuming due to the need of a high number of images to be acquired at different energy loss values for each tilt angle (Figure 3). In addition, this may result in a high electron dose incident on the sample. Objects too sensitive to radiation might not be ideal for EFTET studies, although working at liquid nitrogen or lower temperature may reduce the negative effects of the radiation damage [24]. In the case of EFTET, one important procedure is computation of the reconstruction, since image alignment must be very precise, what can be increasingly difficult due to the low signal-to-noise ratio frequently occurring in data from biological samples. An additional improvement to achieve a good EFTEM tomogram is associated to the prerequisite of unspecific background subtraction which should be based on robust algorithms because it can lead to the overestimation of characteristic signal of the studied element. The use of different law models for background subtraction and of multivariate statistical analysis (MVA) can prevent for this overestimation allowing the computation of accurate maps [25]. Despite these obstacles for the inexperienced user, EFTET should be encouraged since it allows the study of the distribution of specific chemical elements in the sample volume, and its use become justified to prevent incorrect interpretations only based on contrast. Once 3D chemical maps are correctly computed, the returned information gives access to precise elemental positioning in a sample [26].

In our samples, as the TEM image shown in Figure 3, different dark particles can be observed associated to the fungal cell wall. These particles are usually interpreted as

ferritin aggregates which are associated with melanin pigments. However, the computation of the 3D electron map after the use of MVA (Figure 4) demonstrates that not every electron dense area correspond to iron. This map was validated by the quantification of the signal measured at different regions of the sample.

Conclusions

This study has shown that STEM-HAADF tomography is suitable and should be encouraged for the study of small, low contrasted, resin embedded biological samples since provide an improvement of the SNR on reconstructed volumes. This results in the observation of delimited borders against a near-homogenous background on the 3D reconstructions, facilitating the interpretation of the images or allowing them to be used for automatic or semi-automatic segmentation. Regarding EFTEM tomography, it adds the important information of the 3D localization of defined chemical elements which complements the structural data obtained by standard TET. Both, STEM-HAADF and EFTEM tomographies are techniques that will be more applied in future researches in cell biology and microbiology and they are also an important basis for approaches that are currently in development which allow the specific labeling of proteins, by specific heavy metal associated clonable tags [27].

Acknowledgements

Authors want to thanks Dr. Monique

Arpin from the Institut Curie in Paris (France) for providing LLC-PK1 cells. Dr. Sonia Rozental from the Universidade Federal do Rio de Janeiro (Brazil) for the kind donation of fungal samples. The "Fondation pour la Recherche Médicale" for the fellowship of MC, and "Region Ile de France" for its contribution on the purchase of the JEOL JEM-2200FS microscope used for every experiment reported in this manuscript.

References

- [1] Seeram E., Computed Tomography: Physical Principles, Clinical Applications, and Quality Control (CONTEMPORARY IMAGING TECHNIQUES), 3rd edition, Saunders Elsevier, (2008).
- [2] Wernick M.N. and Aarsvold J.N., Emission Tomography: The Fundamentals of PET and SPECT, Elsevier Academic Press, (2004).
- [3] Liang Z. & Lauterbur P.C., Lauterbur., Principles of Magnetic Resonance Imaging: A Signal Processing Perspective, IEEE Press Series in biomedical Engineering, (2000).
- [4] Christian P. E. Christian & Kristen M. Waterstram-Rich, Nuclear Medicine and PET/CT Technology and Techniques, Springer, (2007).
- [5] Bárcena M. Koster A.J. Electron tomography in life science. *Semin Cell*

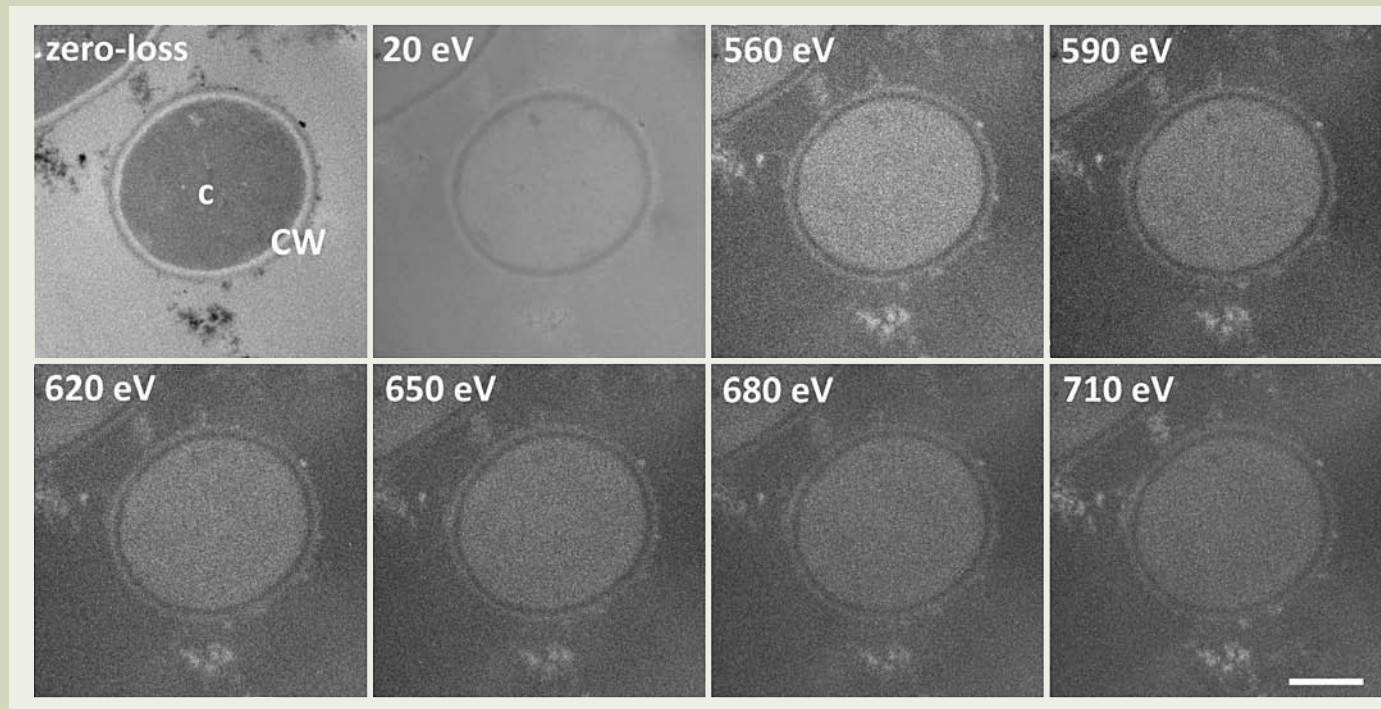


Fig. 3 Untilted images extracted from *F. pedrosoi* tomographic series. A) 0° tilt-images recorded at different energies values between 0 and 710 eV. C= cytoplasm, CW= cell wall. Scale bars 400 nm.

- Dev Biol.* **20**(8), 920-930 (2009).
- [6] Herman, G.T., Fundamentals of computerized tomography: Image reconstruction from projection, 2nd edition, Springer, (2009).
- [7] Larabell C.A. Nugent K.A. Imaging cellular architecture with X-rays. *Curr Opin Struct Biol.* **20**(5), 623-31 (2010).
- [8] Frank J., Electron Tomography: Methods for Three-Dimensional Visualization of Structures in the Cell, Springer, (2006).
- [9] Vanhecke D., Graber W. Studer D. Close-to-native ultrastructural preservation by high pressure freezing. *Methods Cell Biol.* **88**, 151-64 (2008).
- [10] Dubochet J., Adrian M., Chang J. J., Homo J. C., Lepault J. McDowell A. W., Schultz P. Cryo-electron microscopy of vitrified specimens. *Q Rev Biophys.* **21**(2), 129-228 (1988).
- [11] Mader A., Elad N. and Medalia O. Cryoelectron tomography of eukaryotic cells. *Methods Enzymol.* **483**, 245-65 (2010).
- [12] Friedrich H., McCartney M.R. Buseck P.R. Comparison of intensity distributions in tomograms from BF TEM, ADF STEM, HAADF STEM, and calculated tilt series. *Ultramicroscopy* **106**(1), 18-27 (2005).
- [13] Midgley P.A. Weyland M. 3D electron microscopy in the physical sciences: the development of Z-contrast and EFTEM tomography. *Ultramicroscopy* **96**(3-4), 413-31 (2003).
- [14] Frixione E. Recurring views on the structure and function of the cytoskeleton: a 300-year epic. *Cell Motil Cytoskeleton.* **46**(2), 73-94 (2000).
- [15] Ikeda R., Sugita T., Jacobson E.S. Shinoda T. Effects of melanin upon susceptibility of *Cryptococcus* to antifungals. *Microbiol Immunol.* **47**(4), 271-277 (2003).
- [16] Franzen A.J., Cunha M.M., Miranda K., Hentschel J., Plattner H., da Silva M.B., Salgado C.G., de Souza W. Rozental S. Ultrastructural characterization of melanosomes of the human pathogenic fungus *Fonsecaea pedrosoi*. *J Struct Biol.* **162**(1), 75-84 (2008).
- [17] Kremer J.R., Mastronarde D.N., McIntosh J.R. Computer visualization of three-dimensional image data using IMOD. *J Struct Biol.* **116**(1), 71-6 (1996).
- [18] <http://bio3d.colorado.edu/imod/>
- [19] Messaoudi C., Boudier T., Sanchez Sorzano C.O. and Marco S. TomoJ: tomography software for three-dimensional reconstruction in transmission electron microscopy. *BMC Bioinformatics.* **8**, 288 (2007).
- [20] <http://u759.curie.u-psud.fr/software-su759.html>
- [21] Biskupek J., Leschner J., Walther P. and Kaiser U. Optimization of STEM tomography acquisition - a comparison of convergent beam and parallel beam STEM tomography. *Ultramicroscopy* **110**(9), 1231-1237 (2010).
- [22] Sezgin M. and Sankur B. Survey over image thresholding techniques and quantitative performance evaluation, *Journal of Electronic Imaging.* **13**(1), 146-165 (2004).
- [23] Cunha M.M., Franzen A.J., Alviano D.S., Zanardi E., Alviano C.S., De Souza W. and Rozental S. Inhibition of melanin synthesis pathway by tricyclazole increases susceptibility of *Fonsecaea pedrosoi* against mouse macrophages. *Microsc Res Tech.* **15**, **68**(6), 377-84 (2005).
- [24] Aronova M.A., Sousa A.A., Zhang G. and Leapman R.D.. Limitations of beam damage in electron spectroscopic tomography of embedded cells. *J Microsc.* **239**(3), 223-232 (2010).
- [25] Quintana C., Marco S., Bonnet N., Risco C., Gutiérrez M.L., Guerrero A. and Carrascosa J.L.. Optimization of phosphorus localization by EFTEM of nucleic acid containing structures. *Micron.* **29**(4), 297-307 (1998).
- [26] Weyland M., Yatesa T.J.V., Dunin-Borkowska R.E., Laffonta L. and Midgley P.A., Nanoscale analysis of three-dimensional structures by electron tomography. *Scripta Materialia,* **55**(1), 29-33 (2006).
- [27] Mercogliano C.P. DeRosier D.J.. Concatenated metallothionein as a clonable gold label for electron microscopy. *J Struct Biol.* **160**(1), 70-82 (2007).

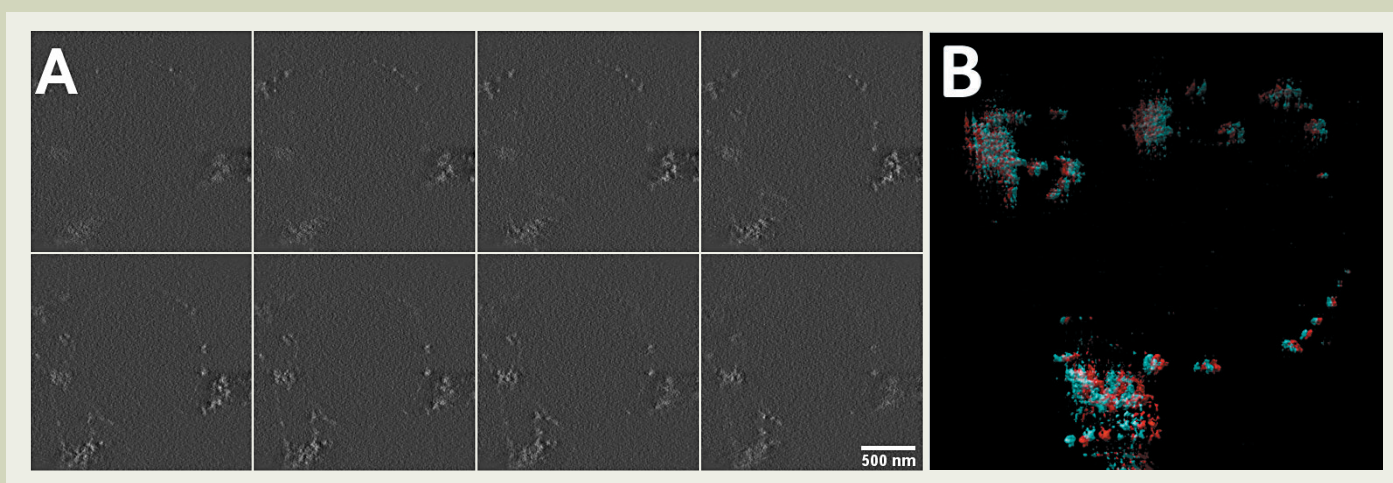


Fig. 4 Iron localization in *F. pedrosoi* by EFTEM tomography after addition of ferritin for melanin detection. A) Sections of the reconstructed iron map after MVA filtering extracted each 16 nm. Scale bar 500 nm. B) Anaglyph of threshold based segmented iron map. Require red-cyan anaglyph glasses.

Application of Scanning Electron Microscope to Dislocation Imaging in Steel

Masaaki Sugiyama[†] and Masateru Shibata^{††}

[†] Advanced Technology Research Laboratories,
Nippon Steel Corporation

^{††} SM Business Unit, JEOL Ltd.

Dislocation imaging using the scanning electron microscope with super hybrid lens will be demonstrated to investigate the dislocation cell walls and single dislocations inside cells introduced by shear deformation in conventional steel. The resolution of the dislocation by electron channeling contrast imaging method is similar to that obtained by conventional TEM observation, and a new approach for the study of dislocations which is possible to detect the heterogeneity of the deformation microstructure will be expected on the view point of the advantage of SEM-BSE techniques. There are two different imaging configurations for doing ECCI, one is a fore-scatter geometry, and the other is a back-scatter one. In the present study, the latter case is utilized, which has advantages for little restriction to the sample size and shape and several applications to the stage design in SEM. Since there are some discussions in the contrast mechanism, the improvement of the backscattering electron detector will bring us several ideas for the application of microscopy to the dislocation study with a combination of the conventional TEM technique.

Introduction

With the increase of the use of high-strength steel, the formability control of steel materials with complex phases becomes important, resulting in the requirement for the understanding of the local defect structure, such as dislocations and several boundaries based on both experimental and computational aspects. The characterization of dislocations and other defects has been mainly studied using transmission electron microscopy (TEM) utilizing diffraction imaging contrast and this has brought us a great success in understanding local dislocation structure and further several interaction models among dislocations and other defects such as solute atoms, impurities, clusters, and precipitation. On the other hand, most structure materials, such as steels, consist of polycrystals, and

their mechanical properties must be considered using a more macroscopic view, taking in the picture of the whole material, including the effect of grain boundary, the crystallography of grains, and other heterogeneities of microstructure. The TEM thin-foil analysis of dislocations has some limitations regarding these multi-scale formation and deformation aspects, due to the thin-foil effect and some difficulty in the preparation of TEM thin foils themselves, including the heterogeneous large area.

Recently, in order to examine the dislocation structure over a larger area of the materials in question, the electron channeling contrast imaging (ECCI) technique using scanning electron microscopy (SEM) has been discussed in various papers. The theory underlying channeling contrast, of course, goes back to the beginning of TEM contrast interpretation in the 1960's, and it is considered that the defect regions in dislocations should give rise to a modulation of the back-scattered electron (BSE) intensity. In the 1990's, several examples in

attempt to obtain dislocation imaging using SEM with and without a field emission gun, along with the imaging and contrast simulation of the clusters for misfit dislocations at the interface, were demonstrated, for example, in strained Si-Ga layers on silicon [1]. Taking into account the effects of surface stress relaxation, back-scattered electron intensity within electron channeling contrast images of dislocations has been also calculated using a two-beam dynamical diffraction model and the simple treatment of multiple scattering [2]. The imaging of screw dislocations near the surface of Si, Ni, and Ga thin films using the ECCI method have been also studied in the 1990's, in which the $\mathbf{g} \cdot \mathbf{b} = 0$ criterion for the dislocation image has been discussed [3]. Based on these results, it was established that the intensity of back-scattered electrons is strongly dependent on the orientation of the incident beam with respect to the crystal lattice. Thus, it was pointed out that the information regarding the crystal orientation and its diffraction conditions

20-1 Shintomi, Futtsu, Chiba 293-8511, JAPAN

sugiyama.masaaki@nsc.co.jp

observed was necessary to understand the dislocation structure using the ECCI method, and the electron channeling patterns (ECP's) and electron backscatter diffraction (EBSD) method were extensively investigated at the same time [4].

In the 1990's, on the other hand, the dislocation images obtained using the ECCI method did not provide sufficient contrast regarding the resolution, which was necessary in order to investigate the dislocation structure for the deformed steel materials. As a result, the dislocation cell structure composing of a set of dislocations introduced under fatigued experiments has been mainly investigated regarding the application of the ECCI method [5]. The study of dislocation structure using the ECCI method has not been achieved for use as a conventional method when compared to TEM for the routine imaging and analysis of dislocations. However, with the progress of instrumentation in the SEM fields in around the 2000's, the imaging of individual dislocations has been gradually achieved over a wide range of conditions using the ECCI method utilizing a standard commercially available SEM, using a straightforward experimental configuration, in which the sample is tilted with high angles such as 60 or 70 degrees [6,7].

In high tilting sample geometry using fore-scatter electrons, it is easy to compare crystal orientation data, such as EBSD, because of the same sample stage geometry, however, it is not so convenient for *in situ* observation, such as in a deformation experiment, as well as for large bulk samples after being deformed, in which experiments have been expected in the research

field for the deformed microstructure of structure materials. There are two ways progress on the ECCI techniques with fore-scatter and back-scatter geometry measurements. In comparison with data obtained by TEM and SEM, the contrast change of edge dislocations in FeAl alloy has been investigated under conditions of $\mathbf{g} \cdot \mathbf{b}=0$ and $\mathbf{g} \cdot \mathbf{b} \times \mathbf{u}=0$ criteria in 2001 [8]. However, the image formation process in ECCI was not so simple, and the overall image quality for ECCI was not as high as that for TEM.

The strong and clear contrast for single dislocations by the ECCI method must be obtained. In 2006, dislocation images observed for a crack tips and edges under low tilting conditions have been reported in deformed NiAl single crystal using a CamScan 44 FE SEM [9]. In contrast to TEM, electron channeling imaging of dislocations is optimized with $s=0$, and the image contrast falls off rapidly with both positive and negative deviations from the perfect Bragg's condition. The dislocation contrast using ECCI is very sensitive for the Bragg's condition, resulting in the misunderstanding for distribution of dislocations, in comparison with the thin foil observation under TEM. In order to consider the simple channeling condition, the fore-scatter geometry for the ECCI method is now superior that the back-scatter one. The careful study using single crystals of 4H-SiC [10] and GaN [11] have been carried out using the fore-scatter geometry detector, and the experimental diffraction parameters and contrast features are determined for the threading screw dislocations. It is concluded from the study of 4H-SiC that the combined influences of the dif-

fraction vector, Burgers vector, and deviation parameter on channeling contrast are found to be markedly similar to the corresponding parameters controlling TEM diffraction contrast [10].

With the progress on the basic approach for the mechanism of dislocation imaging, the applying of SEM instead of TEM will be expected to observe dislocations, because of a lot of advantages on the flexibility for the observation condition. In order to overcome the problems of the actual application of the ECCI method in the field of conventional materials, it is valuable to improve the detector of the back-scattered electron signals and other instrumental conditions. In the present paper, it is demonstrated that single dislocations in deformed and non-deformed steels have been observed with strong contrast and in a wide range of areas using a new detector for back-scattered electrons made by JEOL Ltd.

ECCI Experimental Configuration

The observation of dislocations has been carried out using a JEOL JSM-7001F with super hybrid lens and a Schottky thermal field emission gun operated at 0.1-25keV. A new detector such as an Si detector for back-scattered electrons has been mounted on the pole piece of the objective lens, as illustrated in **Figure 1**. Since the intensity of the back-scattered electrons from the surface in this configuration is smaller than that in the high tilting condition (60-70°), the large collection angle is preferable to

obtain a good contrast of ECCI. The new detector is possible to set a condition of short working distance (WD) by 2mm, the observation conditions are estimated under several conditions, as indicated on the table in Figure 1. The maximum detection solid angle (Ω) is obtained by 2.7str. under the working distance of 3mm. The present experiment for the ECCI technique was carried out using short working distances from 3 to 4mm.

When increasing at a large tilting angle for the sample, it is possible to expand the working distance than 5mm, similar to the conventional SEM. The EBSD for the orientation measurement and the EDS for the composition analysis were carried out using both detectors equipped on the SEM. The other advantage for the design of super hybrid lens is to achieve the minimum external magnetic and electrostatic field on the sample position under the observation, resulting in the easy alignment of the stigmatism and focusing even for strong magnetic materials such as steel.

The steel used in this study consists of conventional low carbon steel with and without a crystal orientation texture. In comparison with the dislocation microstructure, both observation using TEM and SEM were carried out for the electro polished samples with 3mm in diameter, using the SEM stage for a thin foil TEM sample. The surface of a bulk steel plate was also electro polished to observe the dislocation microstructure by the ECCI method, after mechanical polishing. It is not necessary to take account too much for surface conditions of steel, that is, a slight surface oxide film is not affected to the contrast of ECCI, which is a large advantage against the low voltage observation less than 1keV of the thin film surface microstructure on the top

of sample.

Dislocation Cell Walls and Single Dislocations Using the ECCI Method

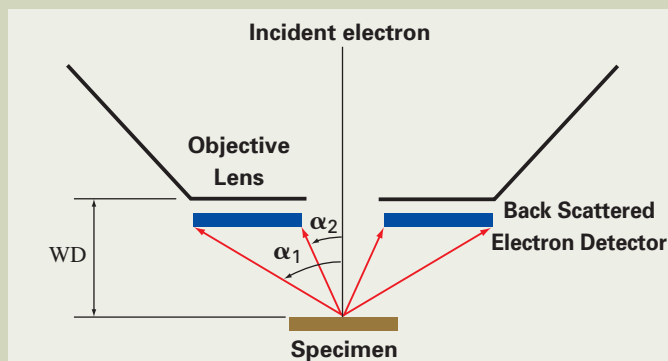
In metals, dislocations have been introduced during deformation as a result of activated process of slip system in relation to the crystal structure. The most of steels used for the structure materials such as automobiles, ships, and buildings etc. are composed of the ferrite phase with a body centered cubic crystal structure, in which screw dislocations are mainly introduced during the deformation at room temperature. The burgers vector of a screw dislocation is $\langle 111 \rangle$ direction and the slip planes are parallel to $\{110\}$ plane in BCC structure.

The most excellent elongation behavior in the thin plates is of γ -fiber plates with the $\{111\}$ texture in the BCC ferrite phase, which are mainly applied as the panel plates of the automobile body. When the simple shear deformation test has been carried out for the model bulk plate with $\{111\}$ texture, it is known that a characteristic directional dislocation cell walls parallel to $\{110\}$ planes have been formed with an increasing of the shear deformation [12]. **Figure 2** is a SEM-BSE micrograph showing dislocation cell walls introduced after 60% simple shear deformation to the ferrite steel with $\{111\}$ texture orientation. The magnification observed was 2,000 times, and the accelerated voltage was 25kV and WD was equal to 4mm. The dislocation cell walls are clearly seen on the whole grains, and the morphology of them is one directional lamellar structure, which is correspondence to the observation result in the thin foil

TEM analysis. On the other hand, the perpendicular cell walls appear close to the triple junction, as seen in the center part of the photograph. It is considered that the other slip system on $\{110\}$ planes was activated under the deformation. This is an example showing the heterogeneity of the deformation, and in comparison with the grain orientation relationship and each dislocation cell walls in the large area using ECCI method, it will be possible to get the information about the heterogeneity of the microstructure developed under deformation.

Since the electron diffraction pattern is not obtained in the conventional SEM, the crystal orientation information using the EBSD measurement was investigated. **Figure 3** is a series of SEM-BSE micrographs (a,b) and the corresponding EBSD orientation maps (c,d). The black right upper part of Fig.3 (a) is a square vacant region used as a marking, which was formed by focused ion beam fabrication. The normal direction of the center grain marked by yellow square is confirmed to be $\langle 111 \rangle$ direction, judging from the ND direction mapping in Fig.3(c). For above the photograph (a) and (b), the direction was determined to be parallel to $\langle 10 -1 \rangle$ direction by the EBSD mapping in Fig.3(d). Based on the analysis, the crystal orientation information in the center grain is determined as indicated in Fig.3 (b). As clearly seen in Fig.3 (b), the formation of two directional traces of dislocation cell walls with (01-1) and (-110) plane are confirmed, which are reasonable planes predicted from the activated principle slip systems in BCC ferrite steel.

Using the present SEM-BSE system, morphology of single dislocations between dislocation cell walls is clearly distinguished using the ECCI method with more high mag-



Acc (kV)	WD (mm)	α_1 (°)	α_2 (°)	$\alpha_1 - \alpha_2$ (°)	Ω (str)
10 ~ 25	2	80	64	16	1.7
10 ~ 25	2.5	72	45	27	2.5
10 ~ 25	3	64	30	34	2.7
10 ~ 25	4	51	20	31	2.0

Fig. 1 Schematic diagram showing geometry of specimen and back scattered electron detector in FE-SEM with super hybrid lens. In the table, accelerating voltages (Acc), working distance (WD), take-off angles, and detection solid angles are also listed.

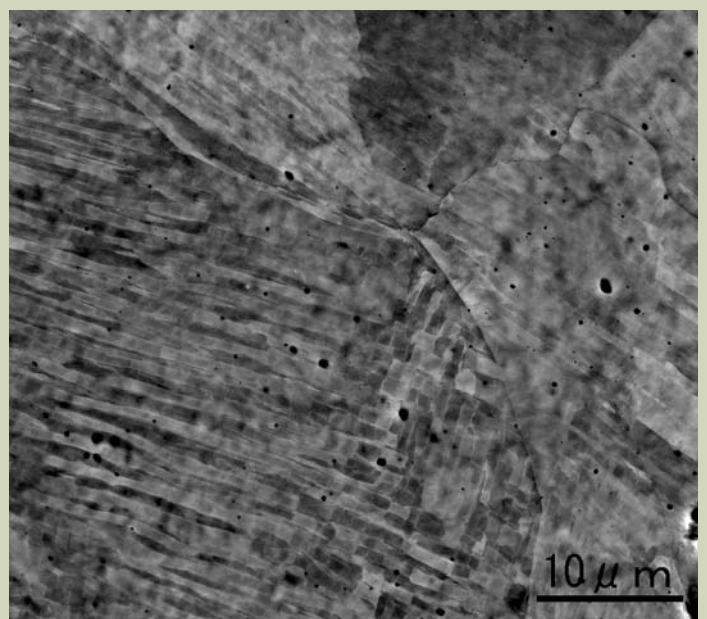


Fig. 2 SEM-BSE micrograph showing dislocation cell walls introduced to each crystal grain after 60% simple shear deformation in steel. A center part of the micrograph is a triple junction of grain boundaries.

nification in the same sample, as seen in Fig.4. The magnification of the photographs; (a) is 30,000 times and (b) is 50,000 times under conditions that WD is 4mm and the accelerating voltage is 25keV. In Fig.4 (a), the center area between the dislocation cell walls is satisfied with a strong channeling condition, resulting in a black contrast of the matrix. The incident electrons proceed to the

deeper region in the crystal and the characteristic contrast of a single dislocation will be white. With enlarging the figure, the single dislocation and its tangled morphology are remarkably observed in Fig.4 (b). The top of a screw dislocation on the sample surface is represented by a pair contrast of white and black, and the dislocation line expanding to the bulk is a white line with a gradient con-

trast. It was confirmed by TEM observation using the same sample that the morphology and density of dislocations and dislocation cell walls are almost similar between the data of SEM and TEM.

The ECCI contrast of the single dislocation is very sensitive to the orientation change of the sample. A series of SEM-BSE photographs with stage tilting conditions of 0,1,2,3

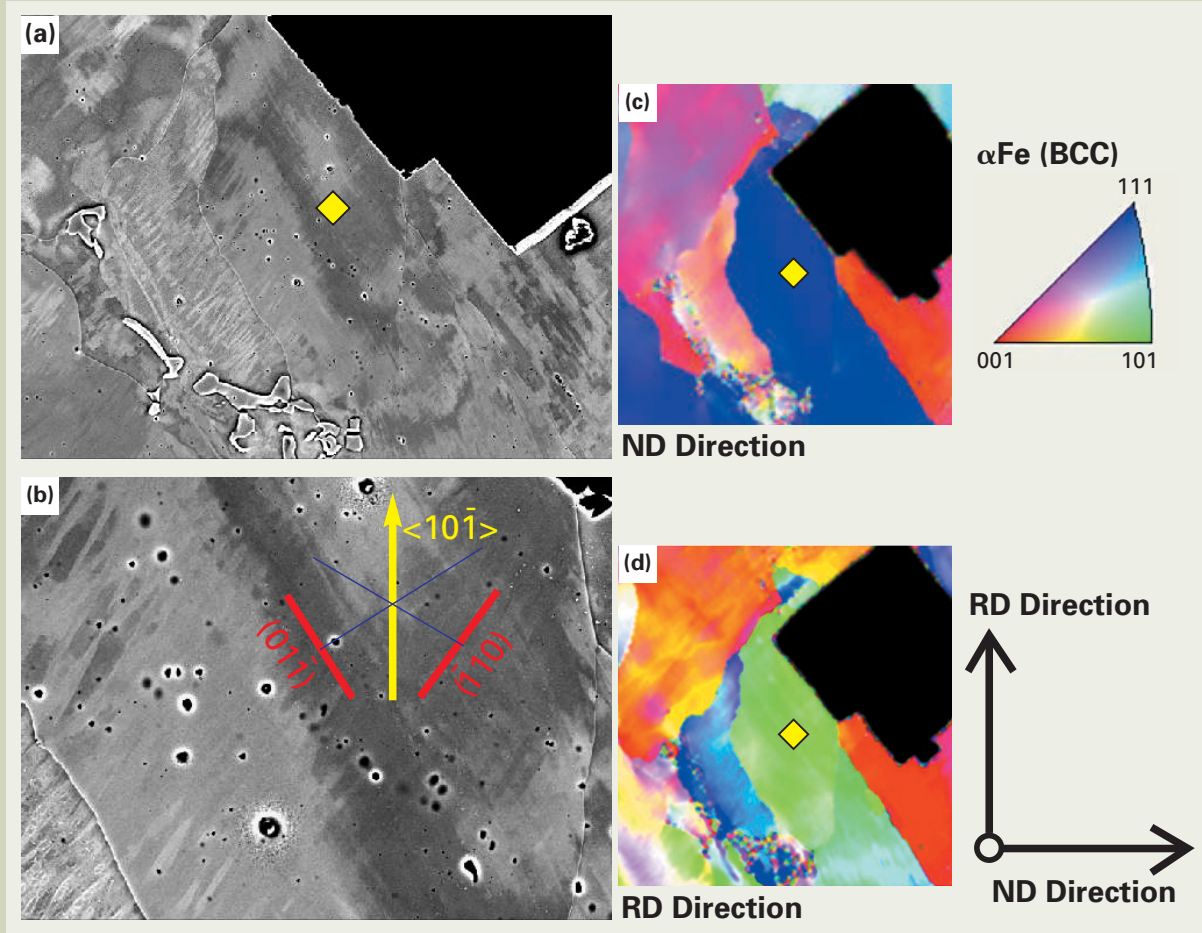


Fig. 3 Orientation analyses for dislocation cell walls using EBSD measurement for same sample investigated by SEM-ECCI method. Micrographs (a)(b) are BSE images, and (c)(d) are orientation mappings images taken from ND direction and RD direction, respectively. The small yellow squares are markings indicating the same grain.

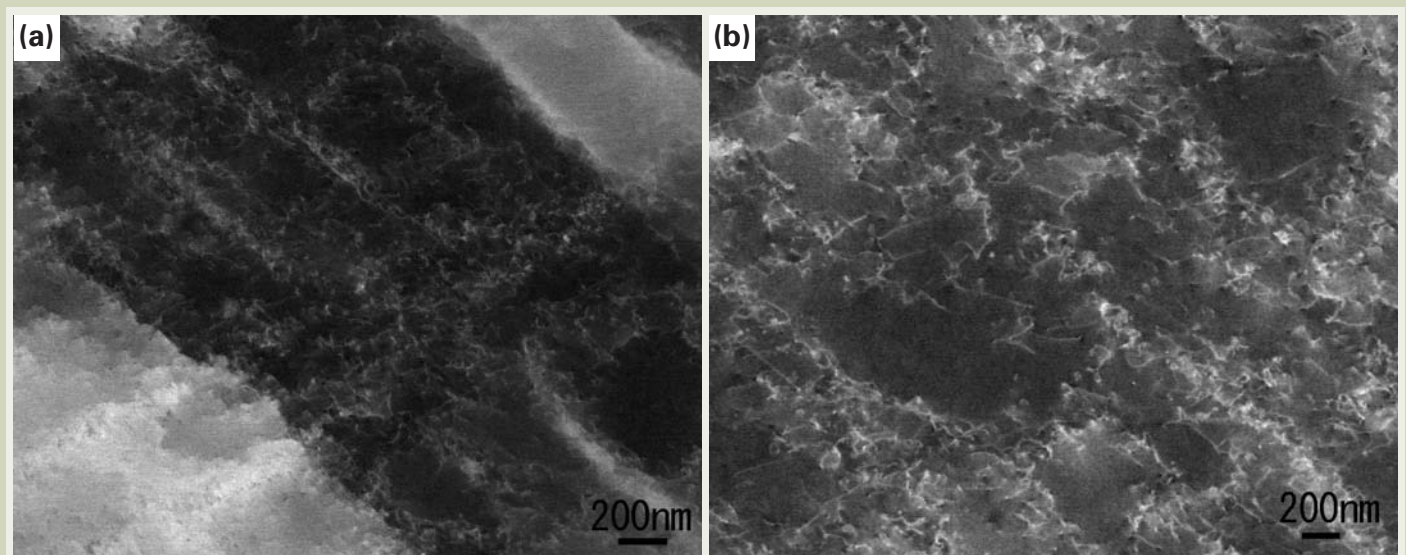


Fig. 4 SEM-BSE micrographs showing single dislocations distributed among dislocation cell walls, in which micrograph (b) is enlarged image of (a).

degrees, respectively in **Fig.5**(a)(b)(c) and (d). The tilting axis is parallel to the horizon line on the photograph. Since the incident beam is parallel to $\langle 111 \rangle$ direction on the grain observed, all dislocation lines must be imaged. The dislocations are screw one with the burgers vector of $\mathbf{b}=[111]$, that is not satisfied with the condition of $\mathbf{g} \cdot \mathbf{b}=0$ criteria. It is found that the dislocation contrast changes within one degree, where the Bragg's angle is about one degree under the accelerating voltage of 25keV. The detail of the contrast mechanism will be discussed in other paper.

Application of the ECCI Method for Other Defects in Steels

The ECCI method is useful to observe other defects, which are mainly investigated by conventional TEM. **Figure 6** is a SEM-BSE micrograph showing complex steel microstructure including ferrite and martensite. The area A is a martensite grain transformed from austenite, enlarged by the inserted micrograph (a). It is found by the SEM-BSE observation that the inner defect of the martensite composes of twined structure, which is identified to be a high carbon martensite. During the steel making process, the carbon enriches from a ferrite to an austenite phase in the complex phase region,

resulting in the different internal defect microstructure of the martensite, which is transformed from the austenite phase during the cooling. If the carbon concentration is low in the previous austenite phase, the internal defects of martensite becomes to be random dislocations, and on the other hand, it is known that the internal defect of the martensite phase changes from the dislocations to the internal twined microstructure with increasing of carbon content in the austenite phase. The SEM observation is an easy way to examine the internal microstructure of the martensite phase, which has been mainly carried out by the TEM observation. The present demonstration shows that such an examination will be possible using the recent ECCI method instead of the TEM one. When the sample is slightly tilted, the other dislocation image in the neighboring ferrite grain marked B appear with a slight change of the crystal orientation condition. With careful tilting experiment, it may estimate the difference of dislocation density depending on the amount of local deformation condition around the martensite grain. In addition, the advantage of the ECCI method is easy to investigate a large area with a heterogeneous microstructure such as the complex phases of ferrite and martensite with different internal defects.

It must be noticed here the sample preparation technique. The SEM-BSE image is not sensitive to the surface oxide film, which is another advantage of ECCI method, because the oxida-

tion of the metal is not avoided. In the purpose to observe the dislocation imaging, only surface residual stress after mechanical polishing is taken care for the sample preparation. After the bulk sample is mechanically polished and ground by the alumina polishing solution, the surface of the sample is performed by only the electrolytic polishing.

As a similar observation example, dislocation cell structures and mechanical twins of 30nm thickness have been observed by the ECCI method using a SEM-EBSD based setup system in twinning induced plasticity (TWIP) steels [13]. The advantage to use the EBSD system instead of ECP's to orientate the crystal into optimal diffraction conditions is proposed in the article. The recent advance of the BSE detector and corresponding improvement for the SEM system provide us the sufficient quality of dislocation images and other defects.

As another example showing a new application of the ECCI method instead of the TEM one, the grain boundary morphology and naturally introduced dislocations are indicated in **Fig.7**. The sample is a conventional ferrite steel with a bulk size, whose grain size is several tens of microns with random orientation, as seen in SEM-BSE micrograph of **Fig.7**(a). Under the observation with a high magnification as 50,000 times, there are some dislocations in a grain and the grain boundary in **Fig.7**(b). The sufficient contrast and resolution for the dislocations enable us to investigate

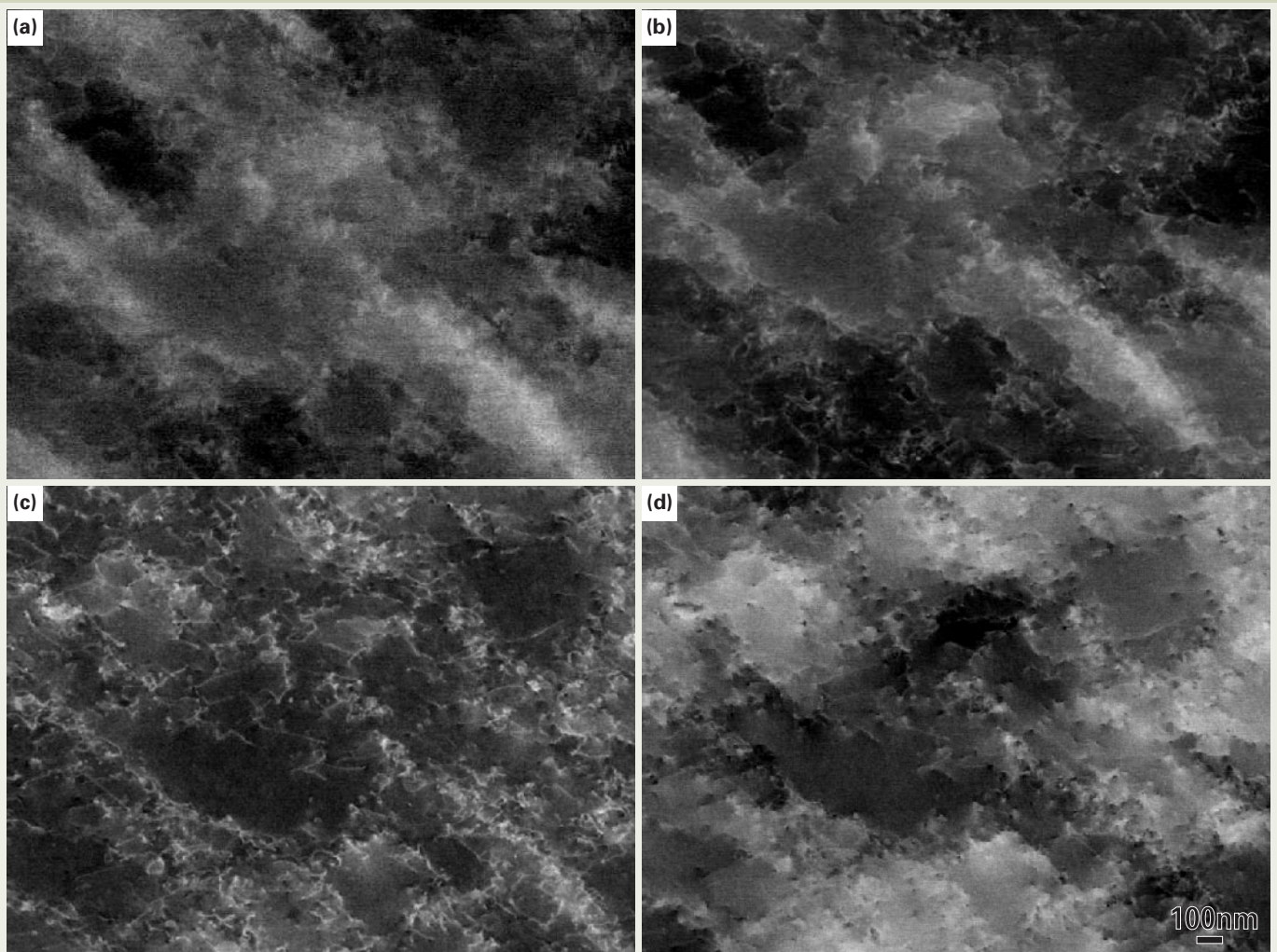


Fig. 5 Change of dislocation image contrast taken by ECCI method with different tilting conditions, (a) 0°, (b) 1°, (c) 2°, (d) 3°, respectively, based on the flat position of the SEM sample stage.

the generation and annihilation of a dislocation under the deformation process.

Summary

A single dislocation image using ECCI method has been clearly obtained using the conventional FE-SEM equipped with the super hybrid lens, which will be also useful for the magnetic material such as steel. Since the resolution of dislocation images is similar to that obtained by TEM, the advantage that wide area can be observed will be a powerful tool to understand the heterogeneity of microstructure under deformation in steel. In the present paper, it is demonstrated that the dislocation cell walls and single dislocation images are observed in the back-scatter geometry of ECCI method, where the sample is mounted on the flat position of the stage in SEM and incident electrons are irradiated perpendicular to the specimen surface. In this geometry, the sample shape and size are not restricted in comparison with the fore-scatter geometry, and several *in situ* observations will be utilized. However, the interpretation of the contrast mechanism for the ECCI method will be more difficult, because several kinds of back-scattering electrons in a material must be considered to understand the case of back-scatter geometry. The detail for the contrast origin and several kinds of imaging data for dislocations will be published in others.

At the present, the limitation of the observation for dislocations still remains because the contrast is strongly affected by the sample tilting condition. The two ways of ECCI methods, which are fore-scatter and back-scatter geometry, will be investigated to make clear the origin of the dislocation contrast in detail and also the diffraction controlling technique will be investigated for the application. Since it is demonstrated to obtain the sufficient contrast of disloca-

tion image using the conventional SEM, the improvement of the sample stage tilting system in SEM will be expected.

Acknowledgments

The authors acknowledge the technical support by SM Business Unit in JEOL to demonstrate the maximum ability of the new BSE detector in the JSM-7001F. The author also expresses the thanks to Dr. Uenishi and Dr. Ikematsu in Nippon Steel Corporation with the deformation experiments and useful discussions.

References

- [1] Wilkinson, A. J., Anstis, G. R., Czernuszka, J. T., Long, N. J. and Hirsh, P. B. "Electron channeling contrast imaging of interfacial defects in strained silicon-germanium layers on silicon", *Phil. Mag. A*, **68**, 59-80 (1993).
- [2] Wilkinson, A.J. and Hirsh, P.B. "The effects of surface stress relaxation on electron channeling contrast images of dislocations", *Phil. Mag. A*, **72**, 81-103 (1995).
- [3] Czernuszka, J.T., Long, N.J., Boyes, E.D. and Hirsh, P.B., "Imaging of dislocations using backscattered electrons in a scanning electron-microscope", *Phil. Mag. Lett.*, **62**, 227-232 (1990).
- [4] Dingley, D. "Progressive steps in the development of electron backscatter diffraction and orientation imaging microscopy", *J. of Microscopy*, **213**, 214-224 (2003).
- [5] Ahmed, J., Wilkinson, A.J. and Roberts, S.G., "Characterizing dislocation structures in bulk fatigued copper single crystals using electron channeling contrast imaging (ECCI)", *Phil. Mag. Lett.*, **76**, 237-245 (1997).
- [6] Ng, B.C., Simkin, B.A. and Crimp, M.A., "Application of the electron channeling contrast imaging technique to the study of dislocations associated with cracks in bulk specimens", *Ultramicroscopy*, **75**, 137-145 (1998).
- [7] Simkin, B.A., Crimp, M.A. and Bieler, T.R., "A factor to predict microcrack nucleation at γ - γ grain boundaries.", *Scripta Metall Mater.*, **49**, 149-154 (2003).
- [8] Crimp, M.A., Simkin, B.A. and Ng, B.C., "Demonstration of the $\mathbf{g} \cdot \mathbf{b} \times \mathbf{u}$ edge dislocation invisibility criterion for electron channeling contrast imaging", *Phil. Mag. Lett.*, **81**, 833-837 (2001).
- [9] Crimp, M.A., "Scanning Electron Microscopy Imaging of Dislocations in Bulk Materials, Using Electron Channeling Contrast", *Microscopy research and Tech.*, **69**, 374-381 (1996).
- [10] Picard, Y.N. and Twigg, M.E., "Diffraction contrast and Bragg reflection determination in foreshattered electron channeling contrast images of threading screw dislocations in 4H-SiC", *J. of Applied Phys.*, **104**, 124906 (2008).
- [11] Picard, Y.N., Twigg, M.E., Caldwell, J.D., Eddy, Jr. C.R., Mastro, M.A. and Holm, R.T. "Resolving the Burgers vector for individual GaN dislocations by electron channeling contrast imaging", *Scripta Materialia*, **61**, 773-776 (2009).
- [12] Uenishi, A, Teodosiu, C. and Nesterova, E.V., "Microstructural evolution at high strain rates in solution-hardened interstitial free steels", *Materials Science and Engineering A*, **400-401**, 499-503 (2005).
- [13] Gutierrez-Urrutia, I., Zaefferer, S. and Raabe, D. "Electron channeling contrast imaging of twins and dislocations in twinning-induced plasticity steels under controlled diffraction conditions in a scanning electron microscopy.", *Scripta Materialia*, **61**, 737-740 (2009).

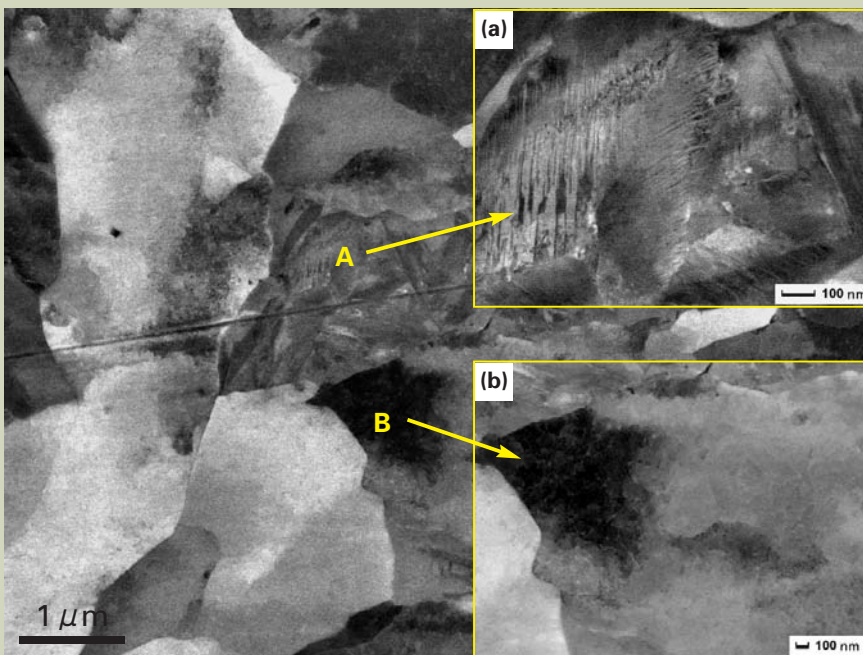


Fig. 6 SEM-BSE micrographs showing morphology of complex microstructure with martensite and ferrite phases in steel. Mark A indicates the martensite grain with internal defects of twinned microstructure as identified by the enlarged micrograph (a), and mark B indicates the locally deformed region in the ferrite grain next to the martensite, the tangled dislocations are seen in the enlarged micrograph (b).

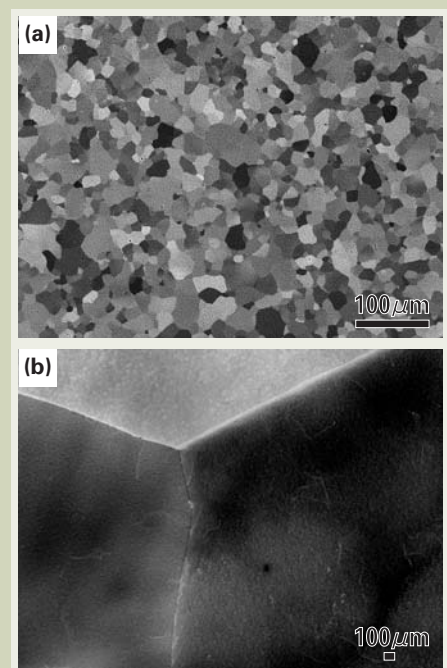


Fig. 7 SEM-BSE micrograph showing conventional polycrystalline steel with random orientation grains (a) and enlarged BSE micrograph taken by magnification of 50,000 times showing naturally introduced dislocations in a grain near to triple grain boundary (b).

Atmospheric Scanning Electron Microscopy (ASEM) Realizes Direct EM-OM Linkage in Solution: Aqueous Immuno-Cytochemistry

Chikara Sato

Biomedical Research Institute, National Institute of Advanced Industrial Science and Technology (AIST)

The JEOL ClairScope™ Atmospheric SEM (ASEM) is the next generation in environmental EM, inverting the traditional SEM column to view the sample from beneath. The open ASEM dish on the top of the column allows directly linked correlative microscopy in open solution: optical microscope (OM) images from above, immediately followed by EM of the same sample area at high resolution, from below. The 35 mm ASEM dish allows neuronal primary culture and efficient antibody labeling-washing cycles. Because the epitopes of cells are preserved in aqueous solution, we tested antibodies, including mouse monoclonal antibodies, used in immuno-fluorescence microscopy. All were successful, enabling observation at SEM resolutions. The resolution of the ASEM is 8 nm, which is advantageous for the observation of fine intracellular structures and bacteria. Observable depth is 2-3 μm at 30 kV, and tissue sections placed on the ASEM dish can be observed immediately. Stained with platinum blue, cell nuclei were especially prominent. This is applicable not only to basic biology, but also to intra-operative cancer diagnosis and detection of pathogens. The ASEM is also highly applicable in non-bioscience fields including materials sciences.

Introduction

Proteins in cells dynamically form molecular complexes with other proteins, which can then form higher-order supermolecular complexes and/or be integrated into cellular organelles. They change location by associating or dissociating with other proteins or molecules, including cytoskeletal proteins. Observation of subcellular supercomplexes and organelles in cells is important for understanding protein behavior and function. The cytoplasm is generally crowded with proteins, especially around the vesicular structures; solid substances, comprised mainly of high-molecular-weight complexes and attached water molecules, usually represent at least 30% of total intracellular weight. Therefore, localization microscopy using specific labeling is also necessary for the determination of protein distribution. For this, labeled probes such as antibodies, complementary oligonucleotides, lectins, and specific ligands can be directly conjugated with fluorescence, or labeled again with a secondary fluorescent tag for visualization by optical microscopy (OM). However, diffraction-limited OM has a resolution limit of approximately 200 nm. Recent super-resolution OM techniques go beyond this [1, 2], but they still do not have high enough resolution to locate protein distributions in fine subcellular structures or

organelles.

Localization microscopy at high resolution has been accomplished with various immuno-electron microscopy (immuno-EM) techniques, such as immuno-transmission electron microscopy (immuno-TEM), that have higher resolution than SEM [3]. However, since these methods require that the sample be placed in vacuum or extremely low air pressure, pretreatment of samples for protection usually requires significant amounts of time and effort. Various sample preparation methods, such as post-embedding, pre-embedding, and the replica method [4], have been developed for immuno-TEM, but the pretreatment of samples in post-embedding methods frequently includes dehydration and resin embedding, which can sometimes decrease antigenicity. Thin-sectioning of samples directly embedded in hydrophilic resin is possible without dehydration, though it requires considerable technical skill. Pre-embedding preserves antigenicity by labeling fully hydrophilic samples; however, the samples must then be dehydrated and embedded in resin, involving the possible shrinkage of delicate subcellular structures. Also, the thin-sectioning required by both pre- and post-embedding methods can restrict information to within a thin slice, if continuous-sectioning is not performed. Culture-substrate-parallel thin sectioning of attached cells is not easy in practice, though it can contain a great deal of information.

Since the first environmental cells were reported in 1944 [5], electron microscope

imaging in solution has been one of the most important goals for high-resolution imaging of cells and tissues. With the advent of new semiconductor technologies, tough, practically electron-transparent films have greatly improved environmental cells [6, 7]. Membrane windows are much stronger, enabling the development of various types of environmental cells with microelectrodes or microfluidic systems [7, 8].

Environmental cells have achieved significant breakthroughs in ligand- and affinity-labeled EM, visualizing the localizations of cellular proteins in solution. With Scanning TEM (STEM), the distribution of the epidermal growth factor (EGF) receptor in COS7 cells was determined by means of 10 nm gold-EGF labeling, at 4 nm resolution, using an environmental capsule holding aqueous samples between two electron-transparent films [6]. Mitochondria were labeled with 0.8 nm gold-streptavidin conjugate, and silver enhanced, enabling determination of their localization in HeLa cells using a SEM-based environmental capsule with windows [9]. Since the hydrophilic environment preserves sensitive epitopes, it should allow labeling with various antibodies. However, the types of cells applicable to these systems are somewhat limited, since only a very small volume of medium can be placed in the closed capsules.

Another trend has been the development of correlative microscopy, which combines various EM systems with OM [10, 11]. Among them, Sartori *et al.* focused on cryo-correlative microscopy [10]. For correlative microscopy

Higashi 1-1-1, Tsukuba, Ibaraki 305-8566, Japan

ti-sato@aist.go.jp

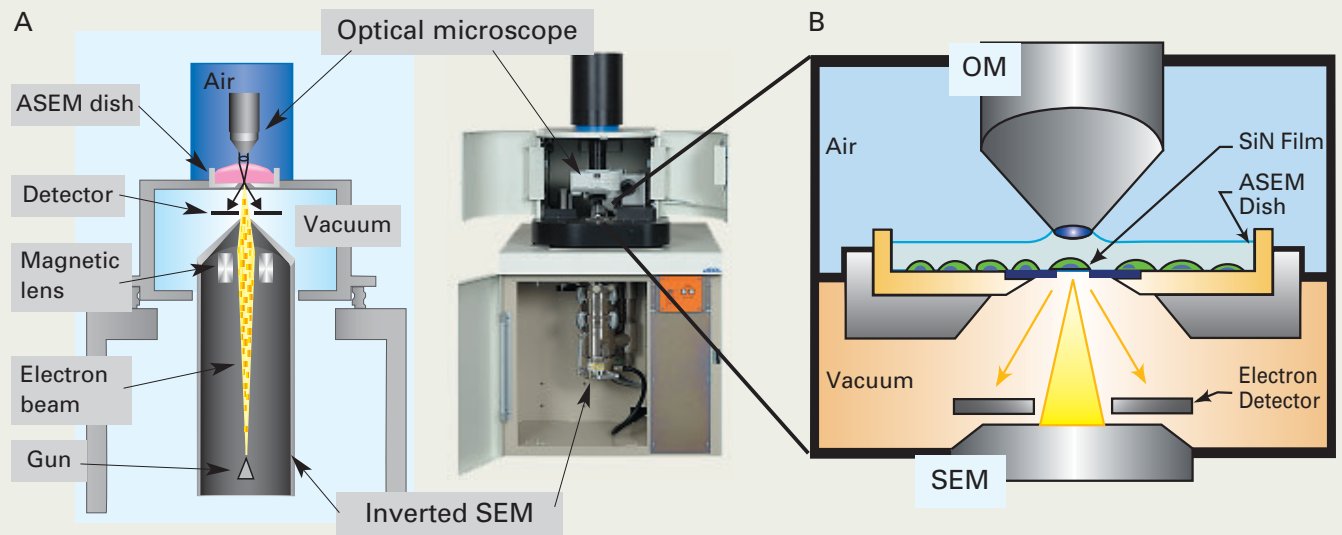


Fig. 1 Schematic diagrams of the ASEM system and the ASEM dish. (A) An Optical Microscope and a Scanning Electron Microscope are arranged in a column. The SEM is inverted, scanning the sample from below. The OM views the open culture dish from above. (B) The ASEM dish separates atmosphere from vacuum. Electrons penetrate the SiN film fabricated into its bottom plate; backscattered electrons are captured by the backscattered electron imaging (BEI) detector. The OM observes samples quasi-simultaneously through a water-immersion objective lens.

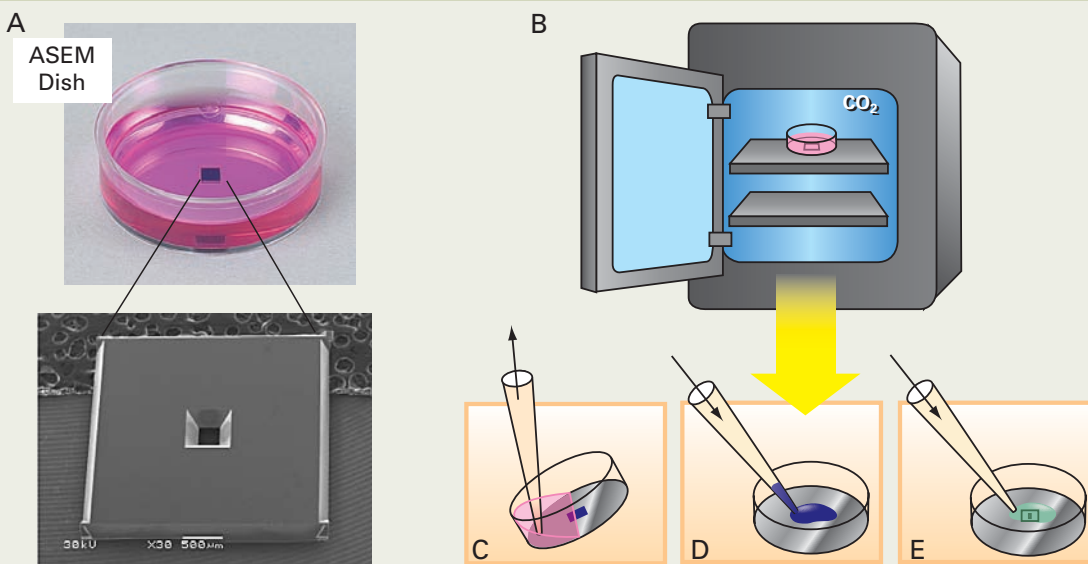


Fig. 2 Cell culture, staining and washing using the ASEM dish. (A) The 35 mm ASEM dish is a disposable plastic Petri dish with a SiN film window fabricated into a silicon chip set in the bottom plate. Below: bottom view of the silicon chip with SiN film window. (B) The ASEM dish, with various coatings, can be used for cell culture in a CO₂ incubator. (C - E) Cell fixation, washing, labeling, and staining are easy to perform with standard laboratory equipment.

in solution, Dukes *et al.* determined the distribution of EGF receptors tagged with EGF-quantum dots on COS7 cells, at a resolution of 3 nm, using STEM [12]. However, a simultaneous direct link between OM and EM is generally not easy. Immuno-correlation microscopy frequently requires tagging an epitope with both fluorescence and gold, which has been made possible by the development of many kinds of labeling systems, e.g., fluoro-nanogold, quantum dots, and sophisticated photo conversion [13-15] [16, 17].

Materials and Methods

The ASEM, with its inverted SEM, was developed simultaneously with the ASEM

dish, as described by Nishiyama *et al.* [18]. For our experiments, cells were cultured on an ASEM dish with or without polyethyleneimine coating, and fixed with 4% paraformaldehyde or 1% glutaraldehyde in PBS (pH 7.4). Except for non-staining or WGA-labeling experiments, cells were perforated with 0.1% or 0.5% Triton X-100. They were stained with heavy metal solution and washed three times. For immuno-EM, COS7 cells were labeled with anti- α -tubulin primary antibody. After fluoronanogold-secondary antibody attachment was confirmed using fluorescence OM, the gold was enlarged using gold sedimentation [19] and observed using the inverted SEM. Wheat germ agglutinin (WGA)-15 nm colloidal gold labeling was

performed as described [18].

Results

Configuration of the ASEM correlation microscope

The JEOL ClairScope™ Atmospheric SEM is the next generation in environmental EM; it inverts the traditional SEM column to view the sample from beneath. This maintains the vacuum necessary for the electron pathway under the thin membrane of the ASEM dish window (Fig. 1). The 35 mm ASEM sample dish is completely open to the atmosphere; it is a traditional plastic Petri dish except for the SiN film window in its

base (Fig. 2). The open configuration allows OM imaging from above, quickly followed by EM of the same sample area at high resolution, from below (correlative microscopy) (Fig. 1B). The optical axes of both microscopes are aligned and fixed to allow quasi-concurrent observation of the same area, while the sample stage can shift two-dimensionally.

This correlative OM/EM microscope has a practical target-size from 200 μm to 8 nm, mainly corresponding to the mesoscopic scale. It provides a fast, relatively easy-to-use way to

bridge the resolution gap between OM and nanoscale structural determination methods.

Preferential staining in solution

The 35 mm ASEM dish allows efficient staining and washing. We employed various traditional heavy-metal EM staining protocols for ASEM observation in solution, and compared them with non-stain controls (Fig. 3). In COS7 cells, uranyl acetate stains protein and nucleic acids. Platinum-blue stains nucleic acids, and especially in combination with 1% paraformaldehyde-

hyde fixation, specifically stains nuclei. Osmium tetroxide stains membranes, and emphasizes lipid droplets as spherical white dots in the cytoplasm. The endoplasmic reticulum, storing Ca^{2+} ions, is an important organelle for cell excitation and neuroplasticity. It was stained using platinum blue, and compared with ER-specific fluorescence-labeling using anti-protein disulfide isomerase antibody (Fig. 4).

Neuronal primary culture

The detachable ASEM dish has a 3 mL

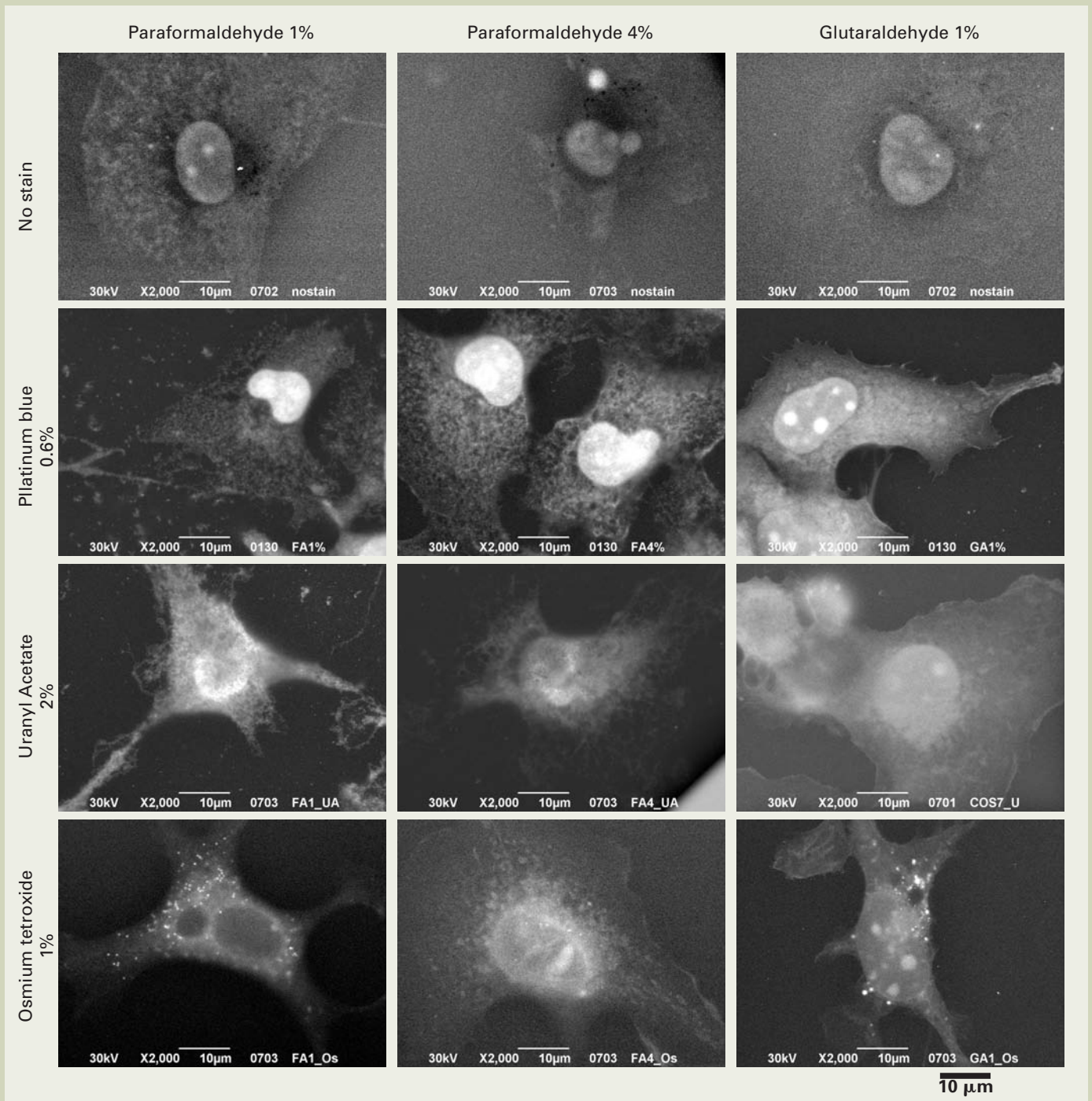


Fig. 3 Preferential staining using heavy metals. Optimum staining conditions for nuclei were determined using COS7. (A) Cells were fixed with different aldehyde buffers, and stained. Among the various staining reagents, platinum-blue especially emphasizes the nuclei. Within the platinum-blue stained groups, nuclei fixed with 1% paraformaldehyde appear at the highest contrast from the background. For comparison, cells were stained with uranyl acetate or osmium tetroxide. Osmium tetroxide staining emphasizes lipid droplets as spherical white dots in the cytoplasm.

capacity and can be used in a CO₂ incubator (Fig. 2). We successfully coated the dish using protocols for glass dishes, and accomplished a wide range of high-level primary culture on the SiN film (Fig. 5). The success with coatings is presumably because the surface of the SiN film is oxidized, creating a layer of SiO during the fabrication process.

Primary culture of neurons is generally difficult, making neurons inappropriate for environmental-cell systems. Cultured neurons on standard dishes can be observed by OM, but resolution is not sufficient for the

observation of molecular complexes or fine subcellular structures, including growth cones and spines. Growth cones were clearly observed using the ASEM at 30 kV acceleration voltage (Fig. 5), with an observable depth of 2-3 μm from the SiN film [20].

Observation of tissue surface

Using the ASEM, brain tissue was also visualized to a depth of 2-3 μm in solution (Fig. 6). A slab of goldfish brain was stained with

platinum-blue and placed section-down on the SiN film. The nuclei in the surface were clear, suggesting the applicability of the ASEM to intra-operative cancer diagnosis without cryo-sectioning.

Subcellular structure of bacteria

Filamentous bacteria used to ferment cellulose for alcohol were observed using the ASEM after staining with phosphotungstic acid. In solution, they manifest as connected

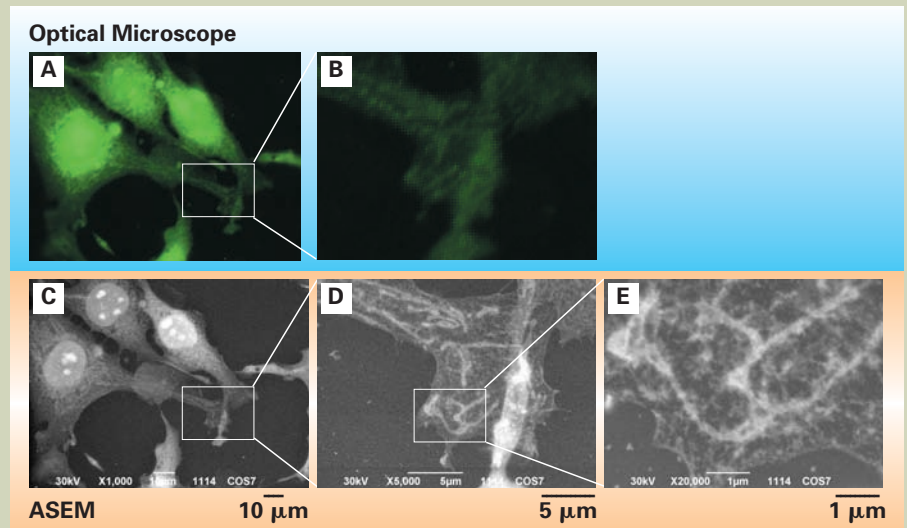


Fig. 4 Endoplasmic reticulum (ER) visualized using the ASEM. COS7 cells were fixed, perforated, and labeled with anti-protein disulfide isomerase IgG2b and with Alexa Fluor® 488-tagged secondary antibody, and imaged with OM. The cells were then stained with platinum-blue and imaged with the ASEM. (A) Fluorescent image. (B) enlargement. (C) EM image of the same cells. (D) ×5,000 magnification. (E) ×20,000.

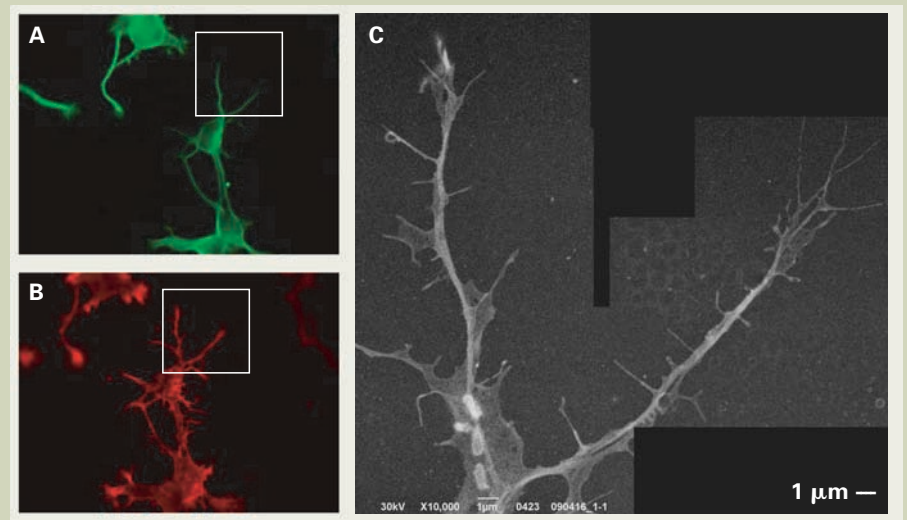


Fig. 5 Cerebral cortex dissociation culture. Neurites of primary-culture pyramidal neurons on day 1, isolated from E16 rat cerebral cortex. (A) Fluorescence microscope image of betaIII tubulin and (B) filamentous actin (F-actin) in neurites. (C) SEM of the neurites stained with platinum-blue. At ×10,000 magnification, filopodia and lamellipodia are moderate-density structures, while the backbone region of the neurite is a high-density area. White squares in A and B correspond to the SEM image in C. Neuron cultures were kindly prepared by Dr. Takashi Shiga (Tsukuba University).

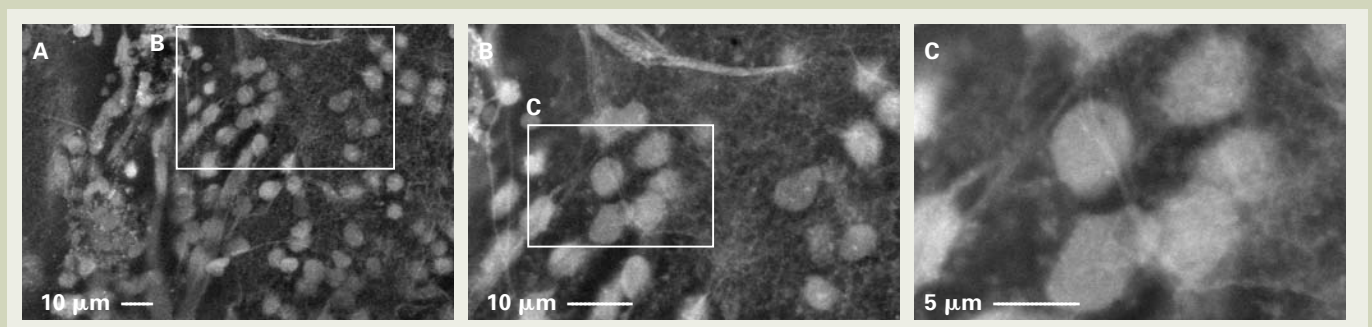


Fig. 6 Tissue sample stained to observe nuclei. A half-brain surgically resected from a goldfish, fixed with 1% paraformaldehyde and stained with platinum-blue. Tissue was laid section-down on the SiN film of the ASEM dish and observed using the ASEM. Surface nuclei are brightly distinguished from the background. (A) ×1,000 magnification. (B) ×2,000. (C) ×5,000. Outlines of nuclei are clear, without cryo-sectioning. Neurite-like fibers are also visible.

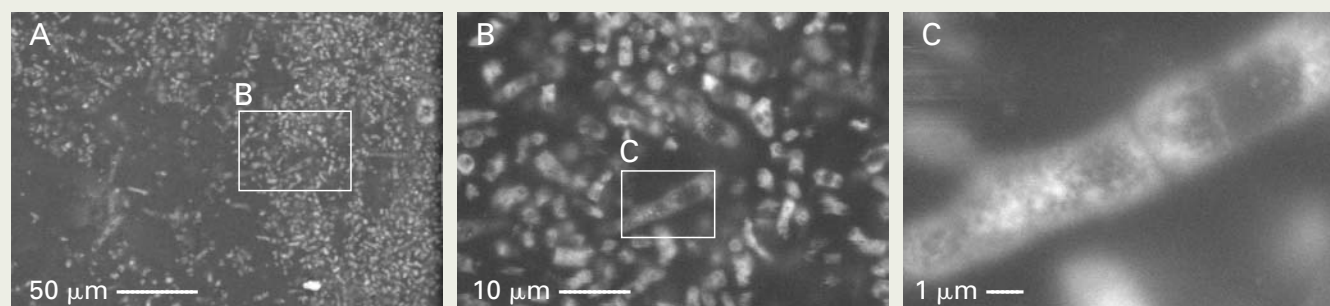


Fig. 7 Intracellular structure of bacteria. Filamentous bacteria used in the fermentation of cellulose for alcohol are stained with phosphotungstic acid, and observed as connected cells forming filaments in solution. Each cell includes fine, granular structures. Filamentous bacteria were kindly provided by Dr. Shigeki Sawayama (Kyoto University).

cells forming filaments. Each cell includes fine, granular structures, which could be involved in fermentation activity (**Fig. 7**).

WGA-labeled EM

Glycosylation is known to play an important role in embryonic development and cancer metastasis. We labeled surface glycans connected to membrane proteins, using lectin. COS7 cells labeled with 15 nm colloidal gold-conjugated WGA were observed using the ASEM (**Fig. 8**). White spots indicating gold signals were ubiquitously distributed over the whole cell, with higher concentrations on cell fringes. Gold signals were especially dense in the pseudopods, including filopodia and lamellipodia. These results correspond well with the expected distribution of the glycans. From the observable gap between gold particles, the resolution is estimated to be 8 nm.

Immuno-EM

The open ASEM dish allows the direct application of various immuno-cytochemical techniques and conditions developed for OM, including labeling and washing. Since epitopes are as well preserved in the fully hydrophilic environment (water solution) as with immuno-OM, samples labeled with a wide variety of antibodies are observed using the ASEM [21].

Cytoskeletal proteins are involved in cell morphology, protein trafficking, cell division [22, 23], and neuronal networking [24]. Tubulin, a typical cytoskeletal protein which makes up microtubules, was immunolabeled with fluoro-nanogold [13], followed by gold enhancement [19] (**Fig. 9**). Since the open structure of the ASEM dish allows efficient labeling and washing (medium change), the whole procedure can be finished within a few hours. Using the ASEM, microtubules were visualized as white lines extending from the center to the periphery of cells at low magnification (Figure 9 B). At higher magnifications, the lines were revealed to be uniform, distinguishable gold particles about 40 nm in diameter (Figure 9 C). It should be noted that background signals were extremely low in this immuno-EM method.

Discussion

Here, we describe dual-labeling of cellular

structures using the immuno-ASEM correlative microscope. Sparsely distributed epitopes can be observed with the fluorescence microscope, and a specific area targeted in the cell. Then, high resolution images can be captured using the inverted SEM. Since the ca. 40 nm gold particles, even after enhancement, are generally too small to observe at the low magnifications used for targeting, this is an efficient means to determine the distribution of proteins. Densely distributed epitopes can be efficiently observed by exploiting the ASEM's broad, $\times 100 - \times 100,000$ magnification range. Quasi-simultaneous correlative microscopy brings another benefit in that, using variously colored fluorescent transfection markers, cells expressing recombinant proteins can be targeted with the OM for SEM imaging. Since only a small percentage of recombinant plasmids are usually transfected into cells, this can be very useful.

Two other advantages are brought by the open ASEM dish: a large variety of cell types are easily culturable, and labeling-washing-staining cycles are quick and efficient. Culture conditions are stable, due to the large volume of the open dish and to the large surface area of the culture medium, which facilitates gas exchange in a CO₂ incubator. Throughput of immuno-EM can be very high, allowing the quick observation of variously conditioned cells, and facilitating drug screening. In this study, all pretreatments were carried out in aqueous buffer, facilitating antigen preservation. More than 50 different antibodies used for fluorescence optical microscopy were tested. Our success rate with these was 100%, enabling observation at SEM resolutions. It should be noted that half were mouse monoclonal antibodies.

Without any need for sectioning, immuno-ASEM images through a depth of a few μm from the SiN membrane. Decreased acceleration voltage reduces the imageable thickness [20], so the depth of the target can be determined by duplicated scans at lower acceleration voltages. This results in imaging comparable to confocal OM, though the ASEM has a fixed focal point.

Without thin-sectioning, the ASEM successfully depicted the cell nuclei of tissue samples, using platinum-blue staining. The size of nuclei is the most important indicator for intra-operative cancer diagnosis, and is traditionally examined using OM, with cryo-sectioning and staining with eosin and hematoxylin. The 15-30 minutes required for this method, however,

means that tumor excision is delayed. The ASEM has the potential to make diagnosis much quicker, since it does not require cryo-thin-sectioning, the most difficult and time-consuming part of the process.

Fast sample examination without time-consuming pretreatment is realized with the ASEM, and operation of the machine is relatively easy to learn, due to the fixed focal point (the height of the ASEM dish's SiN film is always the same). The ASEM is widely applicable not only to basic biology but also to drug discovery, intra-operative cancer diagnosis, pathogen diagnosis, food science, cosmetics, polymer chemistry, nanoscience, and materials-sciences.

Acknowledgements

I thank Dr. Toshihiko Ogura at the National Institute of Advanced Industrial Science and Technology (AIST), Mr. Hidetoshi Nishiyama and Mr. Mitsuo Suga (JEOL Ltd., Japan) for valuable discussions in the development of the ClairScope™. I express cordial thanks to Dr. Takashi Shiga (Tsukuba University) for neural primary cultures, and to Dr. Shigeki Sawayama (Kyoto University) for filamentous bacteria. I thank Dr. Yuusuke Maruyama for immuno-electron microscopy (AIST), Dr. Y. Watanabe (Yamagata Research Institute of Technology, Japan) and Y. Konyuba (JEOL Ltd., Japan) for the manufacture of SiN membranes; Mr. M. Koizumi, and Mr. K. Ogawa for the development and maintenance of the ClairScope™, and A. Kohtz, M. Sato, and S. Manaka (AIST) for technical assistance.

References

- [1] Huang, B., M. Bates, and X. Zhuang, "Super-resolution fluorescence microscopy" *Annu Rev Biochem*, **78**, 993-1016 (2009)
- [2] Hell, S.W., "Far-field optical nanoscopy" *Science*, **316**(5828), 1153-8 (2007)
- [3] Griffiths, G., "Fine structure immunocytochemistry, Springer-Verlag" Fine structure immunocytochemistry, Springer-Verlag, 1993.
- [4] Fujimoto, K., "Freeze-fracture replica electron microscopy combined with SDS digestion for cytochemical labeling of integral membrane proteins. Application to the immunogold labeling of intercellular junctional complexes" *J Cell Sci*, **108** (Pt 11),

Fig. 8 WGA-colloidal-gold labeling of COS cells; resolution of the ASEM. Cells were fixed with glutaraldehyde, and surface glycans were labeled with WGA-colloidal gold conjugates (15 nm in diameter). Using the ASEM, the gold was imaged through SiN film 100 nm in thickness at a magnification of $\times 5,500$ (A), $\times 20,000$ (B), and $\times 100,000$ (C), where (D) cropped from (C) exhibits a resolution of 8 nm.

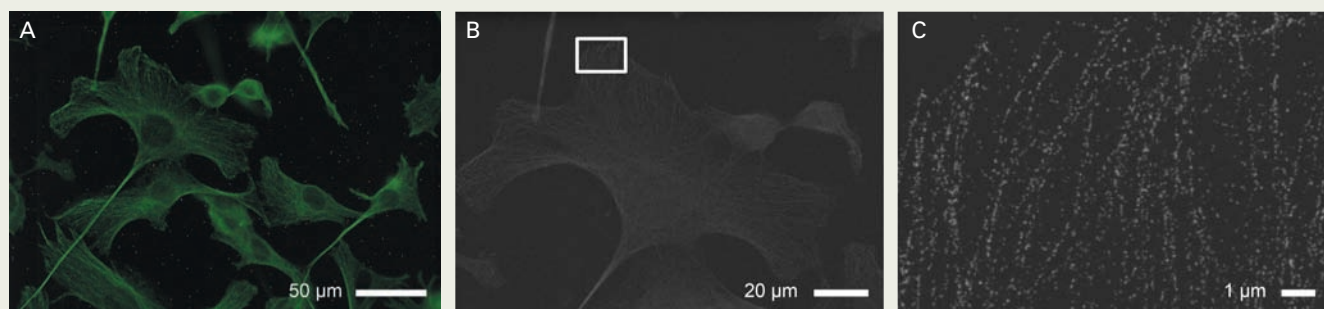
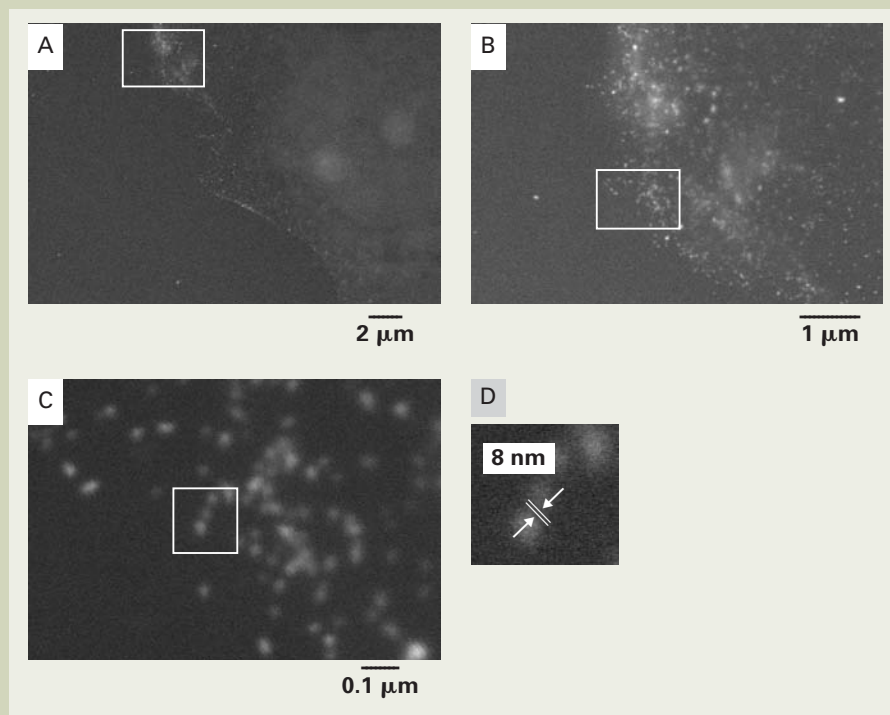


Fig. 9 Immuno-staining of microtubules. Immuno-EM of the cytoskeleton using the correlative ASEM: SEM and OM. C2C12 muscle progenitor cells fixed with aldehyde were labeled with anti-microtubule antibody, and further tagged with fluorescence and gold. Fluorescence (A) is directly compared with the SEM image in buffer at $\times 800$ (B) and at $\times 10,000$ (C).

- 3443-9 (1995)
- [5] Abrams, I.M. and J.W. McBain, "A Closed Cell for Electron Microscopy" *Science*, **100**(2595), 273-4 (1944)
- [6] de Jonge, N., *et al.*, "Electron microscopy of whole cells in liquid with nanometer resolution" *Proc Natl Acad Sci U S A*, **106**(7), 2159-64 (2009)
- [7] Williamson, M.J., *et al.*, "Dynamic microscopy of nanoscale cluster growth at the solid-liquid interface" *Nat Mater*, **2**(8), 532-6 (2003)
- [8] Ring, E.A. and N. de Jonge, "Microfluidic system for transmission electron microscopy" *Microsc Microanal*, **16**(5), 622-9.
- [9] Thiberge, S., *et al.*, "Scanning electron microscopy of cells and tissues under fully hydrated conditions" *Proc Natl Acad Sci U S A*, **101**(10), 3346-51 (2004)
- [10] Sartori, A., *et al.*, "Correlative microscopy: bridging the gap between fluorescence light microscopy and cryo-electron tomography" *J Struct Biol*, **160**(2), 135-45 (2007)
- [11] Agronskaia, A.V., *et al.*, "Integrated fluorescence and transmission electron microscopy" *J Struct Biol*, **164**(2), 183-9 (2008)
- [12] Dukes, M.J., D.B. Peckys, and N. de Jonge, "Correlative fluorescence microscopy and scanning transmission electron microscopy of quantum-dot-labeled proteins in whole cells in liquid" *ACS Nano*, **4**(7), 4110-6 (2010)
- [13] Powell, R.D., *et al.*, "A covalent fluorescent-gold immunoprobe: simultaneous detection of a pre-mRNA splicing factor by light and electron microscopy" *J Histochem Cytochem*, **45**(7), 947-56 (1997)
- [14] Giepmans, B.N., *et al.*, "The fluorescent toolbox for assessing protein location and function" *Science*, **312**(5771), 217-24 (2006)
- [15] Giepmans, B.N., *et al.*, "Correlated light and electron microscopic imaging of multiple endogenous proteins using Quantum dots" *Nat Methods*, **2**(10), 743-9 (2005)
- [16] Gaietta, G., *et al.*, "Multicolor and electron microscopic imaging of connexin trafficking" *Science*, **296**(5567), 503-7 (2002)
- [17] Sosinsky, G.E., *et al.*, "Markers for correlated light and electron microscopy" *Methods Cell Biol*, **79**, 575-91 (2007)
- [18] Nishiyama, H., *et al.*, "Atmospheric scanning electron microscope observes cells and tissues in open medium through silicon nitride film" *J Struct Biol*, **169**(3), 438-49 (2010)
- [19] Hainfeld, J.F.P., R. D.; Stein, J. K.; Hacker, G. W.; Hauser-Kronberger, C.; Cheung, A. L. M., and Schofer, C., "Gold-based autometallography" Proc. 57th Ann. Mtg., Microsc. Soc. Amer., Springer-Verlag, New York, NY, 1999: p. 486-487.
- [20] Suga, M., *et al.*, "Atmospheric Electron Microscope: Limits of Observable Depth" *Microsc Microanal*, **15**(Suppl 2), 924 (2009)
- [21] Murai, T., *et al.*, "Low cholesterol triggers membrane microdomain-dependent CD44 shedding and suppresses tumor cell migration" *J Biol Chem*, **286**(3) (1999-2007)
- [22] Fischer, M., *et al.*, "Rapid actin-based plasticity in dendritic spines" *Neuron*, **20**(5), 847-54 (1998)
- [23] Honkura, N., *et al.*, "The subspine organization of actin fibers regulates the structure and plasticity of dendritic spines" *Neuron*, **57**(5), 719-29 (2008)
- [24] Hirokawa, N., Y. Shiomura, and S. Okabe, "Tau proteins: the molecular structure and mode of binding on microtubules" *J Cell Biol*, **107**(4), 1449-59 (1998)

Information Derived from PGSE-NMR ~Ion Diffusion Behavior, Molecular Association, Molecular Weight / Composition Correlation of Synthetic Polymers~

Yasuhiro Hashimoto^{†,†††}, Mie Nayuki[†], Noriko Horiike[†], and Akira Yoshino^{††}

[†] Asahi Kasei Corporation, Analysis & Simulation Center

^{††} Asahi Kasei Corporation, Yoshino Laboratory

^{†††} Asahi Kasei Corporation, Strategic Planning & Development

Introduction

Pulse-Field Gradient Spin Echo NMR (PGSE-NMR) can be used to calculate self-diffusion coefficients of molecules. Since it is possible to determine the self-diffusion coefficient from each individual peak that can be observed in one-dimensional NMR spectra, we can evaluate the self-diffusion coefficients even for a mixture of multiple molecular species. We can also separate each signal by their diffusion coefficients using the DOSY method [1-4]. Further, it is an important point that the self-diffusion coefficients can be converted into information about the size and molecular weight of the molecules. This method also allows us to link the chemical composition information obtained from the one-dimensional NMR to the self-diffusion coefficients (molecular weight and molecule size) provided by PGSE NMR. Thus, these methods are expected to be very useful in a wide range of material analyses, as will be described below.

(1) Evaluation of ion diffusion in an electrolyte [5-8]

A principal function of an electrolyte is the conveyance of the ions. This conduction phenomenon can be evaluated using a direct physical parameter; the self-diffusion coefficient of the ion species. Even for a mixture of multiple ion species, the diffusion coefficients can be determined for each individual ion specie. For example, in the case of rechargeable lithium ion batteries, the movement of the lithium ions is particularly important, but this information cannot be obtained by assessing the ion conductivity measured for the dissociated

cations and anions as a whole. Thus the information had been obtained using PGSE-NMR methods.

(2) Evaluation of molecular association [9]

Upon association of molecules, the apparent molecular sizes will change, which should be observed as changes in the self-diffusion coefficients. Thus by applying DOSY method, molecular association can be detected.

(3) Evaluation of molecular weight / composition correlation [10-12]

The distribution of self-diffusion coefficients can be converted into the distribution of molecular masses. Furthermore, composition information obtained from the one-dimensional NMR spectra can be correlated with the diffusion coefficients, i.e. the molecular weight of the molecules. Thus, it is possible, for example, to use PGSE-NMR in applications where GPC-NMR is conventionally used, such as evaluating the correlation between the composition of a copolymer and its molecular weight

(4) Reaction tracking [13]

In situations where the size of the molecules changes, such as in synthesis reactions, reaction tracking can be performed by measuring the self-diffusion coefficients of the molecules using PGSE-NMR techniques. In contrast to GPC analysis, where the reaction must be stopped for analysis, this ability of PGSE-NMR to link the information of the self-diffusion coefficients with the information of chemical structures, obtained from the one-dimensional NMR spectra, eliminates the need to halt reactions midway to perform GPC analyses.

(5) Spectrum separation of mixtures

Even if the sample is a mixture of multiple

components, separation of the spectra by diffusion coefficients using DOSY is possible. Thus, there is no longer any need to isolate the components in advance using HPLC or any other separation method. Combining DOSY with other two-dimensional NMR methods like COSY, enables a detailed structure analysis even for complex mixtures.

This is not a complete list, and there are innumerable applications of combined analysis of self-diffusion coefficients and chemical structure information. The ability of PGSE-NMR to relate the structure (composition), physical properties, and performance of a wide variety of materials holds great potential. In 2006, we had acquired a JEOL JNM-ECA400 series NMR spectrometer and a probe capable of generating gradient fields up to 13 T/m, and have been evaluating a wide variety of samples, from liquids to solids. Here we report several examples of our recent applications of PGSE-NMR for material analysis, including ion diffusion in electrolytes, molecular association, and assessment of the molecular weight / composition correlation of synthetic polymers.

Evaluation of Ion Diffusion in Electrolytes

The ion conductivity of an electrolyte is determined by the number and mobility of the dissociated ions. As indicated by the Nernst-Einstein equation, ion conductivity is a function of the self-diffusion coefficients and the sum of the number of cations and anions present, as well as the degree of dissociation.

Using PGSE-NMR, the self-diffusion coefficients can be determined separately for the anions and cations. This makes it possible to evaluate the individual contribution of the cations and of the anions to the ion conductivity.

2-1, Samejima, Fuji-city, Shizuoka, 416-8501 Japan

E-mail : hashimoto.yv@om.asahi-kasei.co.jp

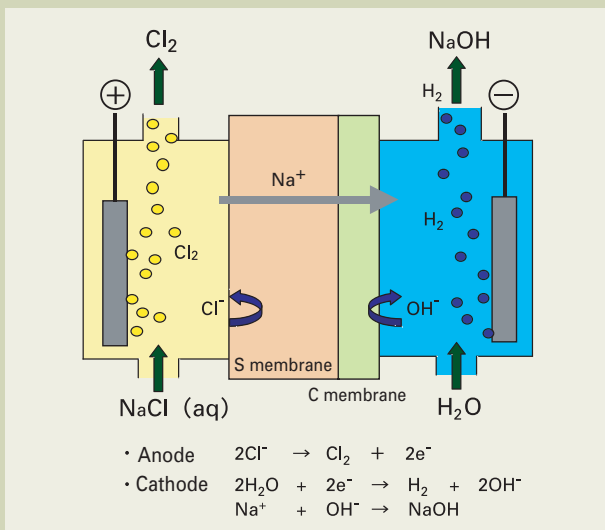


Fig. 1 Chlor-alkali electrolysis process.

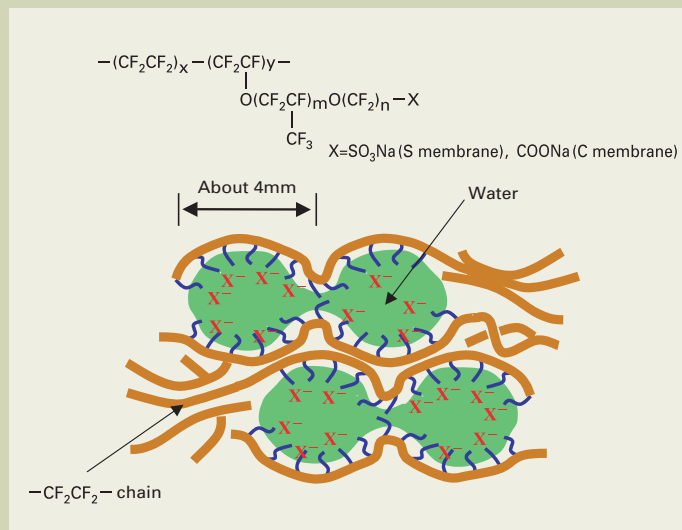


Fig. 2 Cluster structure and chemical structure of the perfluoro ion exchange membrane.

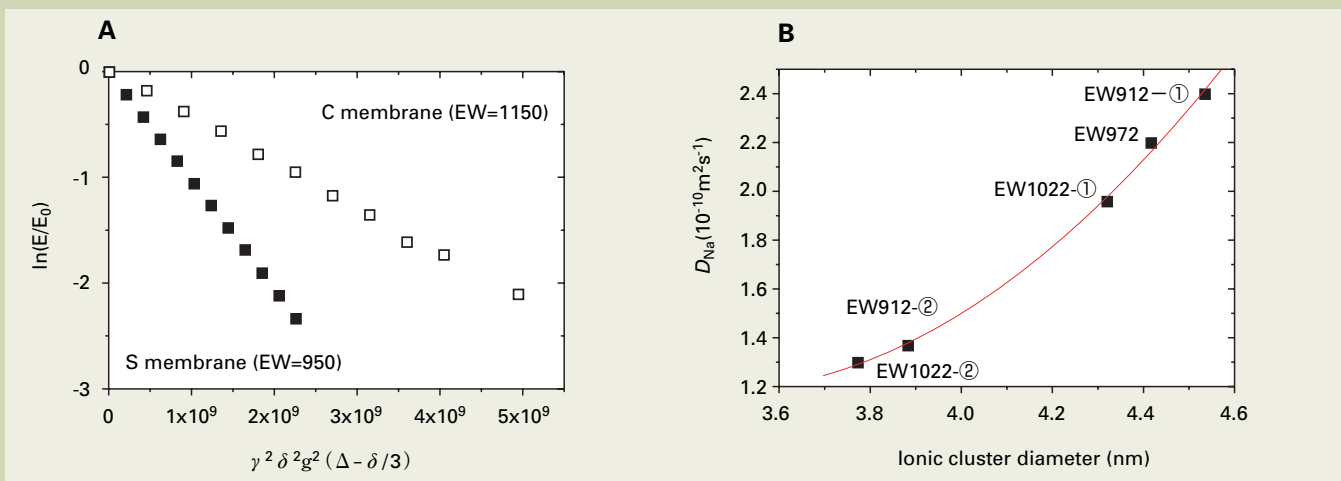


Fig. 3 (A) ^{23}Na - PGSE-NMR diffusion plot for the S membrane (EW = 950) and the C membrane (EW = 1150). S membrane: $D_{\text{Na}} = 1.0 \times 10^{-9} \text{ m}^2/\text{s}$, C membrane: $D_{\text{Na}} = 4.7 \times 10^{-10} \text{ m}^2/\text{s}$. Measurements were carried out with the membrane immersed in water at 90 °C. (B) Relationship between the cluster diameter, determined using SAXS, and the Na^+ self-diffusion coefficient, determined using PGSE-NMR, for membranes with different EW. Both SAXS and PGSE-NMR were performed with the membrane immersed in water at room temperature. ① and ② are polymers with the same EW, but having different membrane formation conditions to control the cluster diameter. In both cases, a PGSE Spin Echo (PGSE-SE) sequence was used for the measurements.

ty, which cannot be obtained by measuring the ion conductivity alone. In this way, it is possible to extract information about the degree of dissociation.

Here, we present diffusion data of Na^+ , Cl^- in chlor-alkali electrolysis, water in fuel cells, and Li^+ in a lithium ion battery.

Chlor-Alkali Electrolysis [14]

Chlor-alkali electrolysis is the process of producing chlorine and sodium hydroxide from NaCl aqueous solution by a membrane electrolysis (Fig. 1). As shown in Fig. 2, a fluorine-based electrolyte membrane, with a carboxylic acid group (C membrane) and a sulfonic acid group (S membrane), is commonly used. Due to the amphipathic nature, the exchange groups within the membranes form water-containing micelles (clusters), inside which the ions move. An important characteristic required for the membranes is the selective permeability of Na^+ cations and the blocking of anions. The structure of these clusters

may have an influence on the cation selectivity. We comprehensively evaluated the cluster structure using small-angle x-ray scattering (SAXS), and the self-diffusion coefficients of the cations and anions using PGSE-NMR.

Since both T_1 and T_2 are short (10 ms or less) for ^{23}Na , a long diffusion time (Δ) could not be used in the diffusion measurement. Furthermore, due to the small gyromagnetic ratio, it was necessary to apply a large magnetic field gradient to attenuate the signals. By using a 13 T/m gradient magnetic field probe, we were able to obtain a good ^{23}Na PGSE-NMR diffusion plot (Fig 3A).

Distinct difference were observed between the S membrane and the C membrane with regard to Na^+ diffusion (S membrane: $D_{\text{Na}} = 1.0 \times 10^{-9} \text{ m}^2/\text{s}$, C membrane: $D_{\text{Na}} = 4.7 \times 10^{-10} \text{ m}^2/\text{s}$). This small Na^+ self-diffusion coefficient in the C membrane was a result of the low water content and the small cluster diameter in the membrane. Using membranes for which the cluster diameter was controlled by changing the film-forming conditions and equivalent

weight (EW), the relationship between the cluster diameter (determined using SAXS) and the Na^+ diffusion coefficient (determined using PGSE-NMR) was clarified (Fig. 3B). It is clear that as the diameter of the clusters that form the path for Na^+ becomes larger, the speed of the Na^+ diffusion increases. The non-linearity in this relationship might be due to the fact that the increase in the cluster diameter does not only make the ion path larger, but also has an effect on the formation of networks and coupling among individual clusters. Furthermore, direct proportional relationship between these Na^+ diffusion coefficients and the ion conductivity were observed. This means that the Na^+ ion conductivity is in accordance with the previously mentioned Nernst-Einstein equation. This is in contrast to the fact that the observed relationship between the ion conductivity and the diffusion coefficient of water for the fuel cell membranes is not linear. This will be discussed later.

In order to evaluate the cation selectivity, we evaluated the diffusion of Na^+ (^{23}Na -NMR),

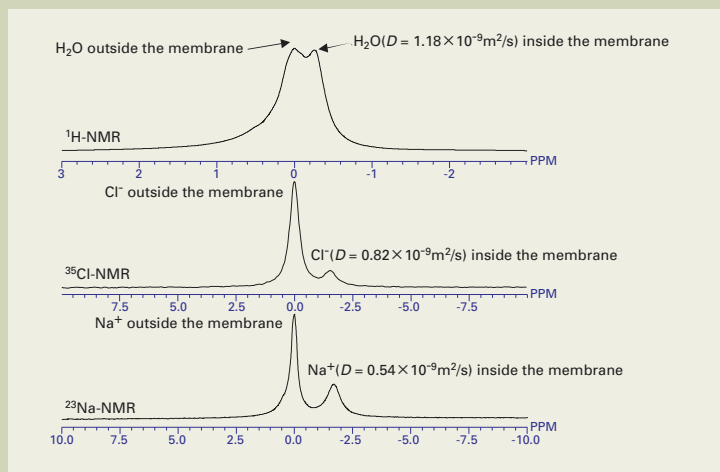


Fig. 4 Self-diffusion coefficient evaluated using PGSE- ^{23}Na -, ^{35}Cl -, ^1H -NMR. Measurements were performed with membranes immersed in 3.5N NaCl aqueous solution at 80 °C.

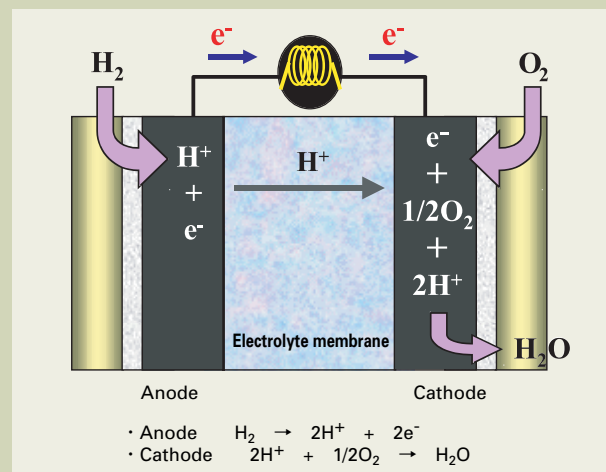


Fig. 5 Solid polymer fuel cell.

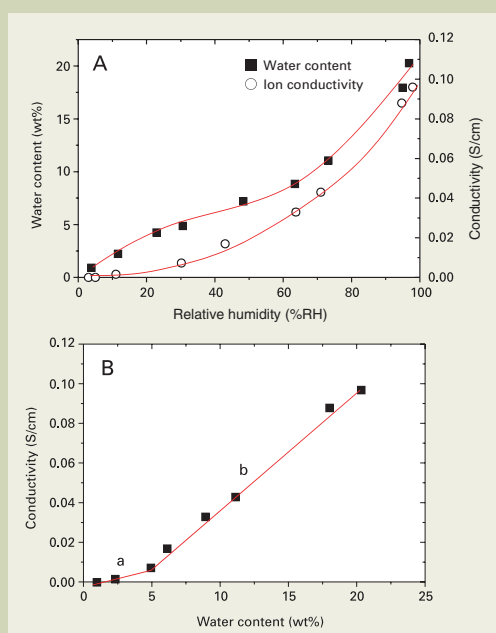


Fig. 6 (A) Dependency of the water content and ion conductivity of the electrolyte membrane on relative humidity. (B) Relationship between water content and ion conductivity. Membrane: S membrane (proton type), EW = 950.

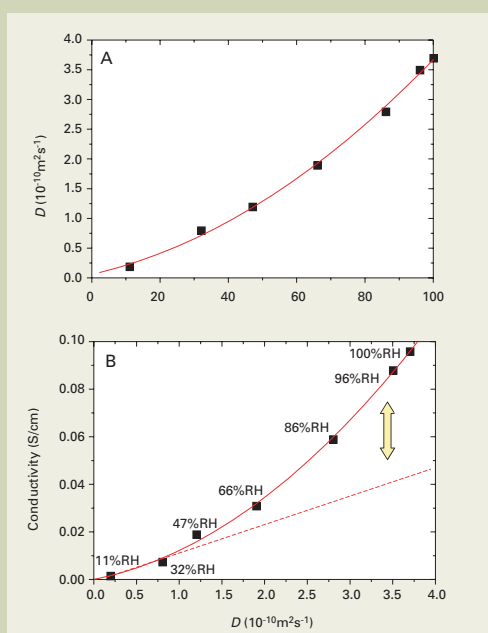


Fig. 7 (A) Dependency of the self-diffusion coefficient of water on relative humidity. (B) Relationship between the self-diffusion coefficient of water and ion conductivity. Membrane: S membrane (proton type), EW = 950, measured at room temperature.

Cl^- (^{35}Cl -NMR), and H_2O (^1H -NMR) using an S membrane soaked in NaCl (80 °C). ^{35}Cl is a low-frequency nucleus, and is outside the frequency range of a conventional probe (JEOL Ltd. TH5 probe), but we managed to perform the measurements by adjusting the tuning beyond the normal limit. The chemical shifts of the ions inside and outside the membrane were different in the spectra, and we were able to selectively evaluate the diffusion of the ions in the membrane (Fig. 4).

These results can be directly related to the electrolyte performance; such as the membrane resistance (Na^+ diffusion coefficient), cation selectivity (Na/Cl diffusion coefficient ratio), and the amount of water permeation (H_2O diffusion coefficient). The ion conductivity measurement can not give each parameter individually. This demonstrates the power of the PGSE-NMR method.

Polymer Electrolyte Fuel Cells [15]

An outline of a Polymer Electrolyte Fuel Cell (PEFC) is shown in Fig. 5. The polymers commonly used as the exchange membrane are sulfonate membranes. In PEFC, the H^+ in the membrane move from the anode to the cathode, accompanying water molecules. It is also known that the ion conductivity of the original fluorine type membranes depends on the relative humidity (Fig. 6A), with a rapid drop of the ion conductivity observed under low humidity. Therefore, it has been necessary to operate PEFC with the membranes in a high-humidity environment.

The relationship between ion conductivity and water content is shown in Fig 6B. As the water content becomes higher, the ion conductivity increases, revealing the importance of the presence of water. Furthermore, there is an

inflection point in the graph of this relationship, indicating the presence of two types of water; type **a**, which makes a small contribution to the ion conductivity, and type **b** with a large contribution. Thus, it was crucial to analyze the states of the water to understand the proton conduction phenomena.

Then we measured the diffusion coefficient of water under various humidity conditions in order to clarify the dependency of proton conductivity on humidity, and the results were analyzed along with information of the states of the water and the membrane cluster structure obtained from IR and SAXS measurements. All the PGSE-NMR, SAXS and IR measurements were performed *in-situ* while controlling the humidity. To achieve this, a saturated brine solution was sealed into the sample measurement cells. Since the saturation vapor pressure varies according to the type of salt, it is possible

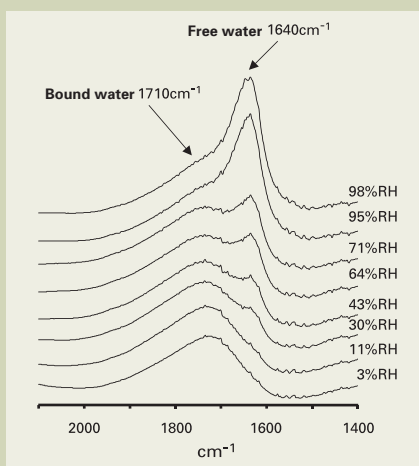


Fig. 8 IR spectra measured on varied relative humidity. Membrane: S membrane (proton type), EW=950, measured at room temperature.

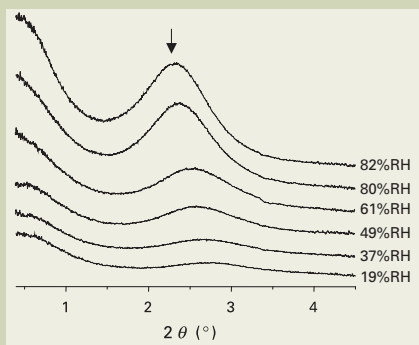


Fig. 10 SAXS profile measured at varied relative humidity. Membrane: Sulfonate membrane (proton type), EW = 950, measured at room temperature.

Fig. 11 The dependency of the cluster diameter determined using SAXS on relative humidity (A), and of the inter-cluster distance (B). Membrane: S membrane (proton type), EW = 950.

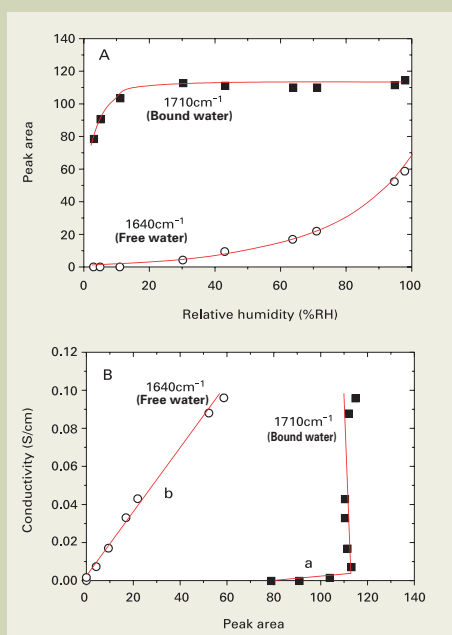
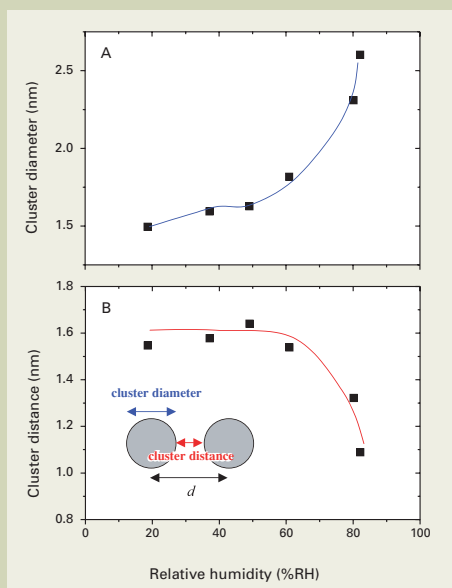


Fig. 9 (A) IR peak area for free and bound water at varied relative humidity. (B) Relationship between IR peak area and the ion conductivity. Membrane: S membrane (proton type), EW = 950.



to control the humidity inside the sample cell. The salts used include $\text{LiCl}\cdot\text{H}_2\text{O}$ (11% RH), $\text{CaCl}_2\cdot 6\text{H}_2\text{O}$ (32% RH), KNCS (47% RH), NaNO_2 (66% RH), NaCl (76% RH), KCl (86% RH), and K_2SO_4 (96% RH).

Fig. 7A shows the dependency of the self-diffusion coefficient of water in the membrane on humidity. As the humidity lowers, there is a rapid decrease in the diffusion coefficient of water, revealing that this is the source of the drop in the ion conductivity. Fig. 7B shows the correlation between the self-diffusion coefficient of water and the ion conductivity. In contrast to the previously mentioned direct linear relationship exhibited between the ion conductivity and the Na^+ diffusion coefficient for chlor-alkali electrolysis, the relationship in this case is represented by a curve. As the humidity rises, it appears that the increase in ion conductivity becomes greater than the rise of the

diffusion coefficient.

To further investigate the source of this change, the humidity dependency of the results of IR and SAXS were investigated. In the IR spectrum, two types of peaks were observed; in positions 1640 cm^{-1} and 1710 cm^{-1} (Fig. 8). The 1710 cm^{-1} peak corresponds to the water directly bonded to the sulfonate proton by hydrogen bonding (bound water). The 1640 cm^{-1} peak is assigned to the free water demonstrating the same behavior as bulk water [16]. Under conditions of low humidity, the amount of bound water increases rapidly as the humidity rises (up to about 30% RH). As the humidity rises above this level, there is no increase in the bound water (Fig. 9). In comparison, the free water steadily increases above 30% RH, with a rapid increase appearing at levels over 70% RH. The relationship between the ion conductivity and the amounts of free water and

bound water (IR peak areas) (Fig 9B), reveals that the increase in bound water at low humidity (see a in Fig 9B) only makes a slight contribution to the ion conductivity, while the growth of free water makes a large contribution to the increase in ion conductivity (see b in Fig 9B). This suggests that the water types a and b in Fig 6 discussed earlier originate from the bound and free water, respectively.

The cluster structure was analyzed using SAXS. The obtained peaks (indicated by the arrow \downarrow in Fig 10) were assigned to the scattering interference peaks for each cluster. The cluster distance (d) was determined from the scattering angle using the Bragg's formula. Furthermore, the cluster diameter was determined by assuming the clusters to be rigid-body spheres and performing fitting. The dependency of the SAXS profile on the relative humidity is shown in Fig. 10. It is clear that for this electrolyte membrane the cluster structure exhibits an extremely dynamic alternation dependent on the external environment. The increase in the peak intensity at high humidity may be due to the increase of the water content. Also, a shift of the peak to the low-angle side was observed, suggesting the growth of d . Fig 11A shows the cluster diameter, determined from the fitting with the SAXS profile dependent on relative humidity. We can observe a rapid increase in the cluster diameter at relative humidity of over 70% RH. Further, the value obtained by subtracting the cluster diameter from d (= separation between adjacent clusters) drops drastically as the relative humidity increases, revealing that the individual clusters are in close proximity (Fig 11B). These rapid changes at around 70% relative humidity correspond to the region of rapid increase in free water discussed earlier.

These results observed for the states of the water support the following conclusions with regard to the non-linear relationship between the ion conductivity and the diffusion coefficient shown in Fig 9B, and the dependence of the H^+ conduction mode on the relative humidity.

- In the range of 0 -30% RH, the water is directly bonded to the sulfonic acid group's proton by hydrogen bonding. This bound water has a low mobility and does not make a large contribution to the ion conductivity.
- In the range of 30 -70% RH, there is no increase in the bound water, and only a slight increase in free water. The free water makes a large contribution to the ion conductivity. However, since the amount of increase is small, there is no large increase in ion conductivity.
- In the range of 70 -100% RH, there is a sudden jump upward in the ion conductivity accompanying a rapid increase in the free water. We can see that the ion conductivity increases more than the corresponding rise of the diffusion coefficient in this range. At humidity levels below 60% RH the ion conduction phenomenon appears to be the H^+ movement accompanying water (Vehicle mechanism). In contrast, at humidity levels of over 70% RH, there is an increase in the free water and the diameter of the clusters makes the path for the ions larger. In addition, the individual clusters form a network, so it is believed that the ion conductivity is manifested as the H^+ hopping between water molecules (Grotthuss mechanism). This may

be the cause of the observed increase in ion conductivity exceeding the contribution of the diffusion coefficient under conditions of high humidity.

As demonstrated above, PGSE-NMR does not simply offer information on the self-diffusion coefficient; the results can be combined with those from IR and SAXS to perform a comprehensive analysis, even enabling interpretation of the proton conduction mechanism, making PGSE-NMR an extremely useful tool.

Rechargeable Lithium Ion Batteries [17]

The movement of the Li^+ ions is important for rechargeable batteries, but it is only possible to evaluate the total mobility of all ions (cations and anions) with ion conductivity measurements. PGSE-NMR can be used to evaluate the Li^+ and the anions separately, and calculations can be performed to determine the Li^+ transport number and degree of dissociation. Furthermore, as presented in the following example, it is possible to analyze not just the ion self-diffusion coefficients, but also the diffusion behavior. **Fig. 12** shows the diffusion plots for the self-diffusion coefficient of Li^+ within two types of polyketone electrolyte membranes with the varying diffusion time (Δ). The self-diffusion coefficient of Li^+ within the Type 1 electrolyte membrane does not exhibit any dependency on the diffusion time. In contrast, the Li^+ diffusion in the Type 2 membrane shows a clear dependency on the diffusion time. The value of the Li^+ self-diffusion coefficient was $D_{\text{Li}} = 5.6 \times 10^{-11} \text{ m}^2/\text{s}$ for Type 1, and $D_{\text{Li}} = 0.4 \times 10^{-11} \text{ m}^2/\text{s}$ ($\Delta = 500 \text{ ms}$) for the Type 2 membrane; so, the value of the Type 1 electrolyte membrane was more than 10 times greater than that of Type 2. Type 1 was an amorphous membrane, while Type 2 was a crystalline membrane. And because of this difference the two should show different diffusion behavior in which the amorphous material (Type 1) should show free diffusion of Li^+ and Type 2 material should pass through barriers, such as crystal sites. This may explain the non-uniform diffusion indicated by the self-diffusion coefficient becoming smaller as the diffusion time becomes longer. In this way, the ability of PGSE-NMR to obtain information on the ion diffusion behavior as well as the self-diffusion coefficients makes it possible to establish additional design parameters for membranes.

Evaluation of Molecular Association

The association of molecules should alter the apparent molecular size. And the self-diffusion coefficient is inversely proportional to the Stokes radius of the molecule. Therefore, it should be possible to detect the association by monitoring the self-diffusion coefficients. Here, we present an example of an analysis of a cyclodextrin inclusion complex.

Evaluation of Cyclodextrin Association [18]

Cyclodextrin (CD) is a cyclic oligosaccha-

ride composed of α 1-4 linked glucose molecules. A six-membered sugar ring is called α CD, a 7 sugar ring molecule, β CD, and the 8-sugar ring molecule, γ CD. The outside region of the CD ring is hydrophilic, while the interior is hydrophobic, and this feature gives CD the property of trapping and retaining a variety of compounds (guest molecules) inside its ring [19, 20] (**Fig. 13**). These inclusion complexes are widely used in the pharmaceutical, food product and chemical saccharide fields, taking advantage of the solubility, extended-release and masking effect properties.

Conventionally, the detection of the association of a CD host and a guest molecule was performed by methods like tracking changes in UV or 1-dimensional NMR spectra. The difficulty, however, is that these changes in the spectra do not necessarily indicate the inclusion directly. In comparison, a DOSY method allows us to obtain parameters that are related to the apparent molecular size, i.e. the diffusion coefficients, which should enable a more direct evaluation of the inclusion phenomenon. Upon association, the diffusion coefficient of the host and guest molecules should become identical.

First, we present an example of an analysis of the inclusion of para-nitrophenol (PNP) in α CD. DOSY measurements were performed against a sample mixture of these molecules in a 1:1 (mole ratio) in water (**Fig. 14B**). The results show that although the diffusion coefficient of PNP is smaller than that of PNP alone in an aqueous solution, it is not equal to that of α CD. Then, the mixture ratio of these two compounds was varied and DOSY measurements were performed. The results show that the diffusion coefficient of PNP was dependent on the mixture ratio; as the PNP fraction decreases, the value approaches the α CD dif-

fusion coefficient (**Fig. 14 A, B, C**). This suggests that in the time scale of DOSY measurements, a rapid exchange occurs between the free and CD associated PNP. Thus the average self-diffusion coefficients of the free and included PNP was observed. As the proportions of PNP and α CD were varied, the proportion of PNP captured in the α CD also changed, causing the alternation of the diffusion coefficient. At the lower PNP content, the percentage that was captured by the α CD was larger, and the observed value approached the α CD diffusion coefficient. In this way, by analyzing the variation in the diffusion coefficient relative to the PNP/CD ratio it is also possible to obtain information about the association constant. We also note that the self-diffusion coefficient of α CD was independent of changes in the mixture ratio. This is due to the fact that there is no significant change in the Stokes radius of α CD, even when associated with PNP.

Next, an example of the inclusion of 4,4'-biphenyl dicarboxylic acid sodium salt (BDC) in α CD will be shown. As can be seen from **Fig. 15A**, a diffusion coefficient value observed for BDC agrees with that of α CD. In addition, there are also peaks obtained that match the diffusion coefficients for the BDC and the α CD alone. This should correspond to the free molecules that are not involved in an inclusion complex. This indicates that unlike PNP, BDC is stably contained in the inclusion complex (does not show fast exchange). $^1\text{H-NMR}$ peaks corresponding to the CD-BDC complex was assigned by their diffusion coefficient. Then the molar proportion of BDC and α CD was clearly identified to be 1:2. The diffusion coefficient for the inclusion complex is smaller than that of the free α CD, which also suggests that the complex is not simply a 1:1 pairing of BDC and α CD; rather, a dimer

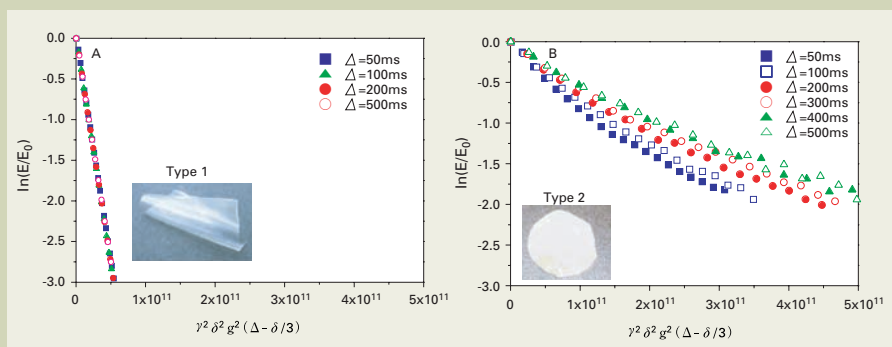


Fig. 12 Diffusion plot of ^7Li -PGSE-NMR measured at varied diffusion times for polyketone-type electrolyte membrane.
(A) Type 1 electrolyte membrane: $D_{\text{Li}} = 5.6 \times 10^{-11} \text{ m}^2/\text{s}$
(B) Type 2 electrolyte membrane: $D_{\text{Li}} = 0.4 \times 10^{-11} \text{ m}^2/\text{s}$ ($\Delta = 500 \text{ ms}$)

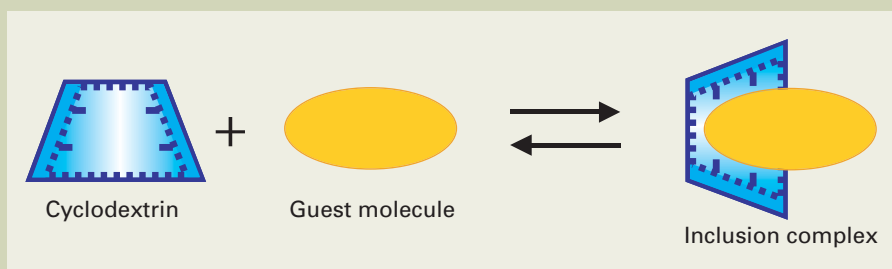


Fig. 13 Inclusion of a guest molecule in CD.

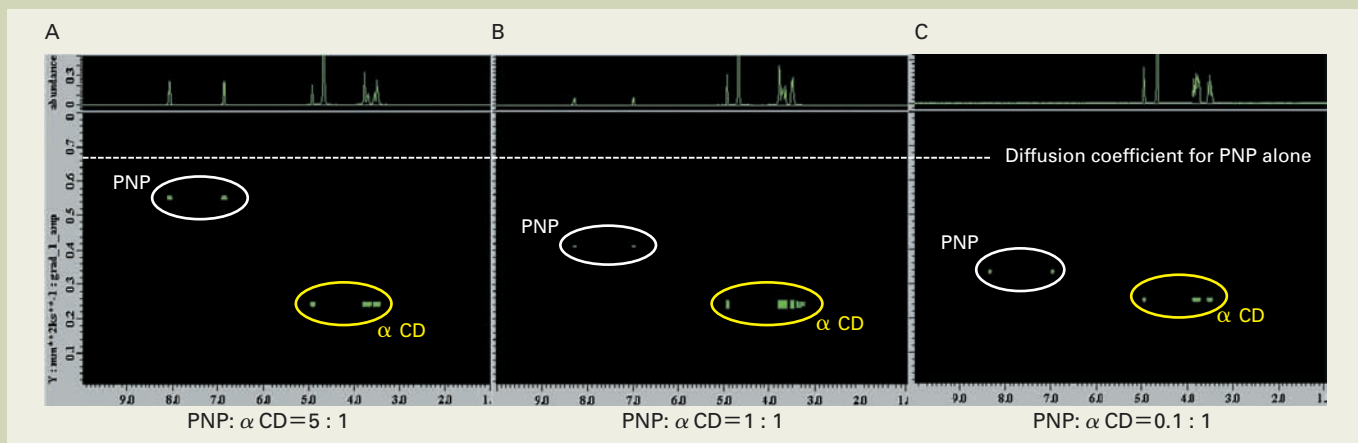


Fig. 14 ^1H -DOSY spectrum for a PNP- αCD inclusion complex. (A) PNP: αCD = 5:1 (mole ratio), (B) PNP: αCD = 1:1 (mole ratio), (C) PNP: αCD = 0.1:1 (mole ratio). DOSY measurements were performed at room temperature.

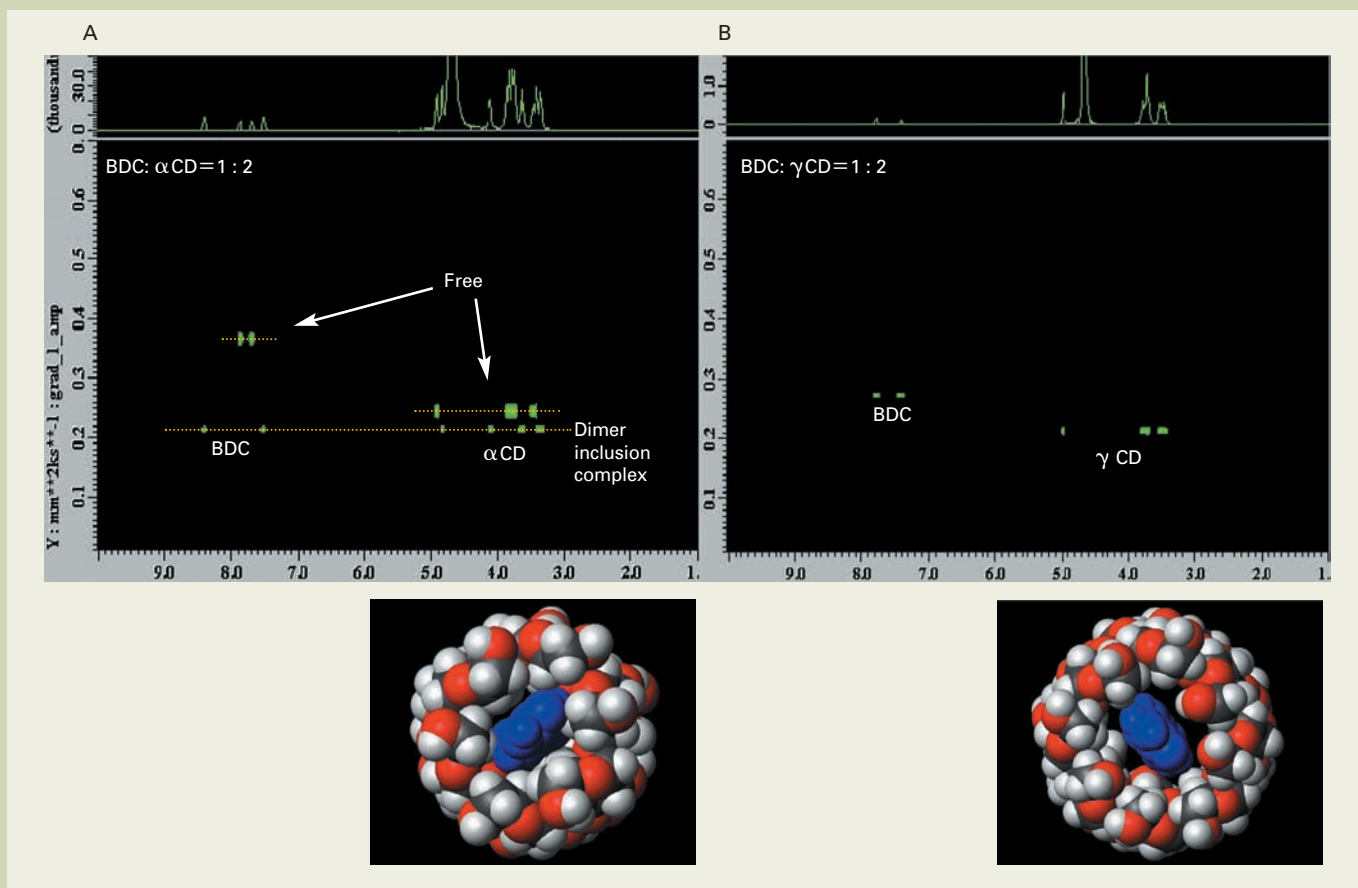


Fig. 15 ^1H -DOSY spectra. (A) BDC: αCD = 1:2 (mole ratio), (B) BDC: γCD = 1:2 (mole ratio).

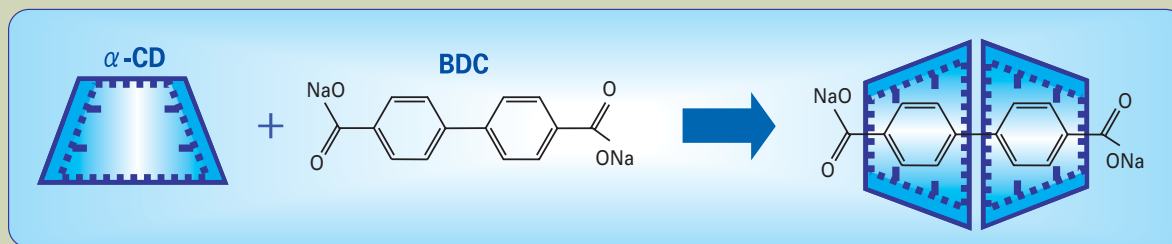


Fig. 16 Formation of the BDC and αCD dimer inclusion complex.

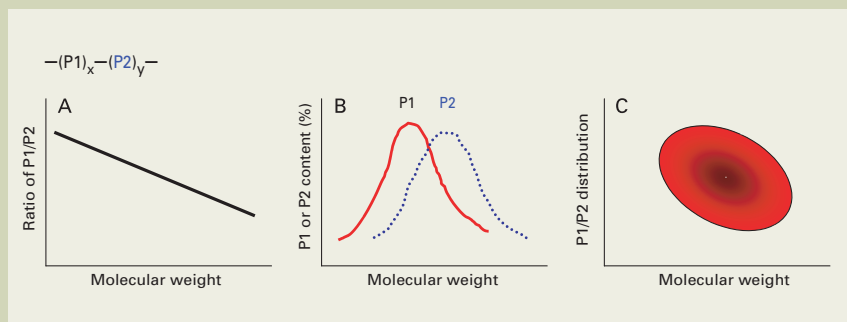


Fig. 17 Schematic drawing of the distribution of copolymer composition dependency on molecular weight.

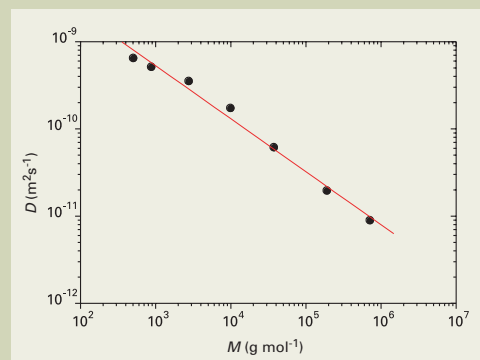


Fig. 18 Relationship between the molecular weight of polystyrene (M) and the self-diffusion coefficient (D). $D = (2.1 \times 10^{-8}) \times M^{-0.6}$

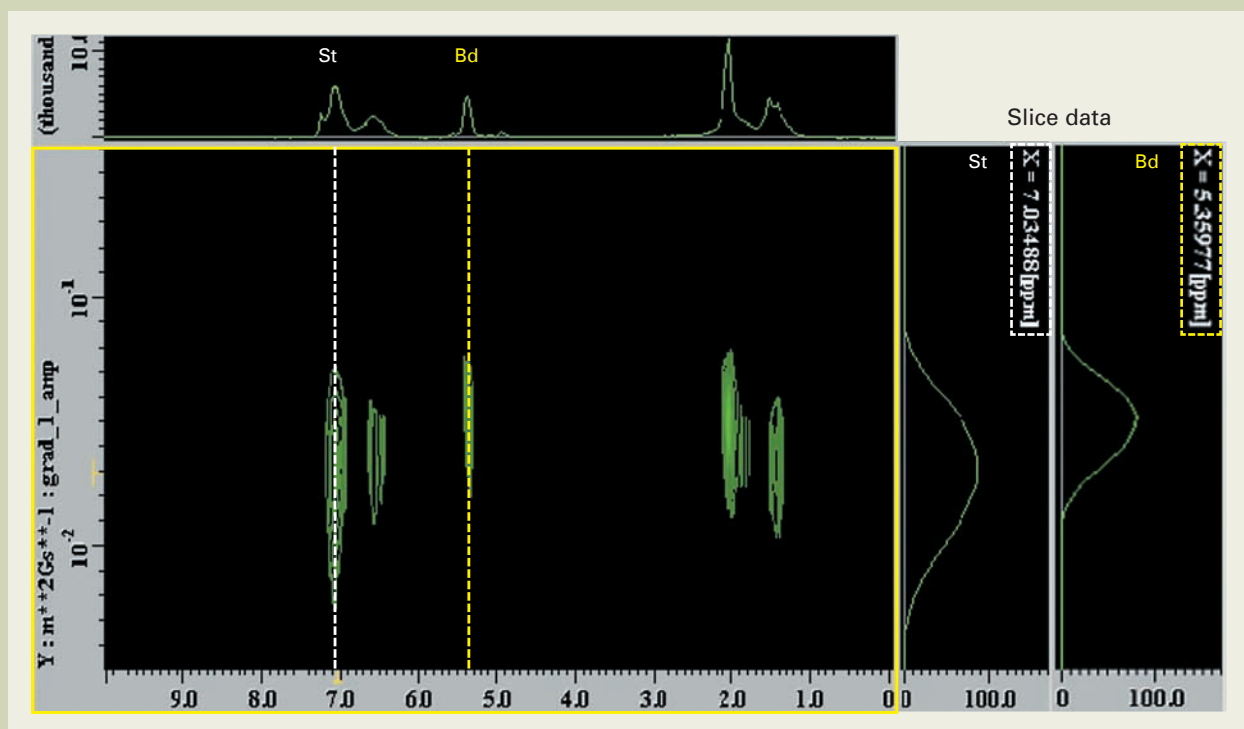


Fig. 19 ^1H -DOSY spectrum of styrene-butadiene copolymer. The sample was dissolved in CDCl_3 , and measurements were performed at room temperature.

inclusion complex, as illustrated in **Fig. 16**. This dimer structure is thought to be the reason for the stability of this inclusion complex. The trapping of the BDC molecules by 2 molecules of αCD in the solution also agrees with the results from X-ray structure analysis of the crystal [21].

In contrast, in the case of the BDC- γCD system, the diffusion coefficients do not match between BDC and γCD (Fig. 15B), unlike the BDC- αCD system. In the same way as observed for PNP- αCD , there appears to be rapid exchange in the time scale of the DOSY measurements. Since the inner diameter of γCD is large for the BDC, so the molecules do not fit precisely, and a stable complex is not formed.

We have presented an example of an analysis of CD association using DOSY, and have shown that the intuitive and straightforward assessment of molecular association is capable. Furthermore, this method also offers the ability to acquire comprehensive information such as the association constants, stability

(exchange), and the inclusion structure. In addition, because the time scale for the DOSY measurements is dependent on the diffusion time (Δ), as discussed for the evaluation of lithium diffusion above, by freely varying the time scale of the measurements, and tracking the Δ -dependence of the diffusion coefficient, it is possible to obtain information on the exchange rate of the complex.

Evaluation of Correlation between Molecular Weight and Composition of Synthetic Polymers

In the case of a synthetic copolymer composed of several monomer constituents, the composition ratio of the monomers is often used as a parameter to specify the structure of the polymer. However, the molecular mass dependency (**Fig. 17A, B**) or distribution (**Fig. 17C**) of this composition is also an important

parameter for the polymer properties. Thus, there is a strong demand for detailed analysis of the composition and structure. For example, for the molecular mass dependence of the composition, the conventional technique had been used to perform NMR analysis on each of the GPC fractions, or to apply a GPC-NMR method in which GPC and NMR are linked on-line. However, not only are these methods complicated and cumbersome, these methods also have the disadvantages that once a fractionated portion has been dried, it can no longer be dissolved in the solvent; or, as for GPC-NMR, it is necessary to use a costly NMR solvent as the eluent. In comparison, with DOSY the self-diffusion coefficient and its distribution can be determined for each individual peak from each component. Therefore, evaluation of the correlation between the molecular weight (diffusion coefficient) and the composition (NMR spectrum) is possible. Here we present an example of analysis of a styrene-butadiene copolymer using DOSY.

select the best method according to the information that is required.

Acknowledgements

We would like to express our sincere appreciation to Dr. Kikuko Hayamizu of the National Institute of Advanced Industrial Science and Technology (AIST) for guidance and advice on a wide range of areas related to the evaluation of ion self-diffusion coefficients, from measurement to data interpretation. We are also grateful to Mr. Satoshi Sakurai of JEOL Ltd. for invaluable assistance with the PGSE-NMR measurements, particularly the measurements for ^{23}Na and ^{35}Cl .

References

- [1] C. S. Johnson Jr., *Progress in Nuclear Magnetic Resonance Spectroscopy* **34**, 203 (1999).
- [2] K. Hayamizu, *Nihondenshi News* **38**, 2 (2006) (in Japanese)
- [3] S. Sakurai, JEOL Application Note NM146 (2002) (in Japanese)
- [4] S. Sakurai, JEOL Application Note NM134 (2000) (in Japanese)
- [5] K. Hayamizu, Y. Aihara, S. Arai and C. G. Martinez, *J. Phys. Chem. B* **103**, 519 (1999).
- [6] M. Saito, N. Arimura, K. Hayamizu and T. Okada, *J. Phys. Chem. B* **108**, 16064 (2004).
- [7] M. Saito, K. Hayamizu and T. Okada, *J. Phys. Chem. B* **109**, 3112 (2005).
- [8] K. Hayamizu, *Kobunshi Ronbunshu* **63**, 19 (2006).
- [9] S. Simova and S. Berger, *J. Incl. Phen.* **53**, 163 (2005).
- [10] K. Ute, *Kagaku* **54**, 69 (1999) (in Japanese)
- [11] K. Ute, *Kobunshi* **51**, 824 (2002) (in Japanese)
- [12] K. Ute, *Seisan to Gijutsu* **59**, 26 (2007) (in Japanese)
- [13] M. Nakakoshi, *Nihondenshi News* **38**, 10 (2006) (in Japanese)
- [14] Y. Hashimoto, N. Horiike and S. Yamazaki, Lecture Summary of 46th Annual Meeting of the NMR Society of Japan, 92 (2007) (in Japanese)
- [15] Y. Hashimoto, N. Sakamoto and H. Iijima, *Kobunshi Ronbunshu* **63** 166 (2006).
- [16] R. Buzzoni, S. Bordiga, G. Ricchiardi, G. Spoto and A. Zecchina, *J. Phys. Chem.* **99**, 11937 (1995).
- [17] Y. Hashimoto, N. Horiike, S. Yamazaki, H. Shobukawa and A. Yoshino, The 48th Battery symposium in Japan, 780 (2007).
- [18] N. Horiike, Y. Hashimoto and S. Yamazaki, Preprints for the Society of Polymer Science, Japan, 55, 3002 (2006).
- [19] A. Harada, J. Li and M. Kamachi, *Nature* **356**, 325 (1992).
- [20] A. Harada, J. Li and M. Kamachi, *Nature* **364**, 516 (1993).
- [21] S. Kamitori, S. Muraoka, S. Kondo and K. Okayama, *Carbohydrate Research* **312**, 177 (1998).

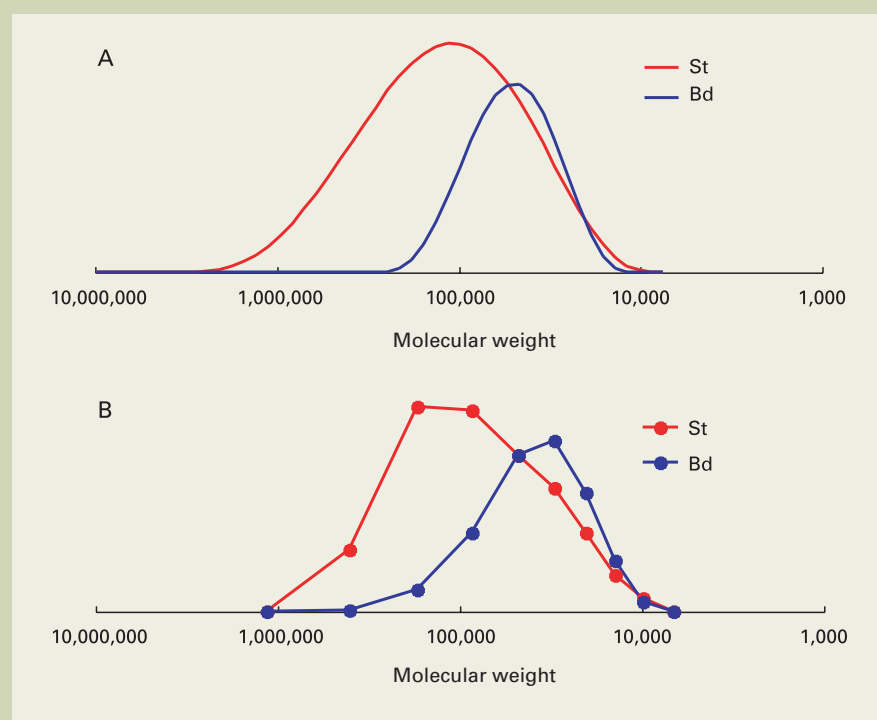


Fig. 20 Dependency on molecular weight of the styrene and the butadiene unit content. (A) As determined from the slices of the DOSY spectra of the styrene peak (7.1 ppm) and the butadiene peak (5.4 ppm). CONTIN protocol was used for the inverse Laplace transform. (B) As determined from the styrene / butadiene ratio from the ^1H -NMR of the GPC fraction (conventional method)

Correlation between Composition and Molecular Weight for Styrene-Butadiene Copolymer

The relationship between the molecular weight and the diffusion coefficient for standard polystyrene of differing molecular weights (usually used for GPC molecular weight calibration) is shown in Fig. 18. On the log-log plot, a nearly straight line is obtained. Using this relationship as the standard curve, calculation of the molecular weights from the obtained diffusion coefficients is possible. However, in the same way as the molecular weight calibration curves for GPC, when it is not possible to generate the calibration curve using the identical polymer as in the test sample, it is difficult to determine the true molecular weight. Therefore, it is necessary to keep in mind that the results will be a "polystyrene-equivalent weight", in the same way as for GPC.

We used DOSY on a styrene-butadiene copolymer to determine the dependency of the styrene / butadiene unit composition on the molecular weight (Fig. 19). The 7.1 ppm aromatic ring peak for the styrene unit, and the 5.4 ppm double-bond peak of the butadiene unit were used to obtain diffusion coefficients and the distribution. Using the calibration curve mentioned above, the molecular weight and its distribution were obtained for styrene and butadiene units individually. The results of the DOSY experiment were compared to the results of the conventional method in which NMR composition analysis was performed for each GPC fraction.

The comparison of the results from the conventional method (GPC fraction \rightarrow NMR) with the DOSY results is shown in Fig. 20. The results from these two methods are in close agreement, confirming the reliability of the DOSY method. It is clear that the high molecular weight components are styrene unit rich, with the components having a molecular weight of about 1,000,000 being nearly 100% styrene. In contrast, the low molecular weight components in the range of 100,000 to 300,000 have styrene and butadiene units in nearly equal proportions.

Applying the DOSY method in this way enables us to make detailed characterizations of a synthetic polymer. It is not only significantly simpler than the conventional methods, it is especially effective for analyzing compounds that become denatured when the fractions are concentrated and dried. For the styrene-butadiene copolymer used for this study, once the GPC fraction solution is dried, it cannot be re-dissolved, so care is required in the concentration process. DOSY does not have this disadvantage.

DOSY provides information about the dependency of the composition on the molecular weight, as shown in Fig. 17 A and B. The analysis of the composition distribution, however in Fig. 17 C is not possible. For such a case, a two-dimensional GPC-LC method, composed of a combination of GPC (molecular weight isolation) and LC (composition isolation), is required. The drawbacks are that it is not easy to define the LC conditions, and it is necessary to search for the optimal conditions for each sample. Therefore, it is necessary to consider and

Development of JEM-2800 High Throughput Electron Microscope

Mitsuhide Matsushita[†], Shuji Kawai[†], Takeshi Iwama[†], Katsuhiko Tanaka[†], Toshiko Kuba^{††} and Noriaki Endo[†]

[†] EM Business Unit, JEOL Ltd.

^{††} Electron Optics Sales Division, JEOL Ltd.

Introduction

In recent years, new material developments utilizing nanometer-order structure control technologies are actively being carried out, as well as product developments using these newly developed materials. In the process of developing these materials and products, it becomes indispensable to use a scanning-transmission and/or a transmission electron microscope ((S)TEM) for the methods of morphological observation and analysis of a local area. Furthermore, in high-tech industries such as the semiconductor industry, the (S)TEM is installed in the site near the production line as an analysis tool for improving the yield rate of production and analyzing defect causes, and the user is making full use of the (S)TEM at any time of the day and night. However, installation of the (S)TEM in such a site often causes problems from the viewpoints of cost and usability. In order to solve these problems, the JEM-2800 High Throughput Electron Microscope has been newly developed. This report describes the product concept and features of this instrument.

Product Concept

Table 1 shows the needs of (S)TEM for users in the semiconductor industry. The users in the semiconductor industry feel that the previous or present (S)TEM requires a professional and proper operator. The users also feel that the implementation cost of (S)TEM is higher compared with that of other instruments such as SEM.

On the other hand, the users hope that a future (S)TEM has a user interface allowing anyone to operate, and that the implementation

cost of the future (S)TEM is reduced, as well as in the future, (S)TEM can maintain a stable operating rate after installation. The users also hope to effectively apply the future (S)TEM to various data acquisitions such as 3D observation by Tomography. Based on these requirements, the JEM-2800 has been developed so that this new instrument can be accepted by many companies and research laboratories with keywords of “high throughput” and “high usability.”

Features

External view

Figure 1 shows an external view of the JEM-2800. The installation environment of a (S)TEM differs largely depending on environments of user sites. In addition, there are many cases where an installation room does not sufficiently meet the installation requirements of a (S)TEM. To overcome this situation, the microscope column of the JEM-2800 is covered with an enclosure so that the (S)TEM can be stably used. The enclosure is designed by taking account of smooth maintenance so that the down time can be minimized at the maintenance. The instrument height is about 2.6 m, making it lower compared with the general 200 kV TEM. The user sits at the front of the operation console shown to the right side of Fig. 1, and can perform all the operations of the instrument.

User interface

A user who used a SEM or a user who uses a (S)TEM for the first time often has an impres-

sion that the operation of the (S)TEM is difficult. In the JEM-2800, we have newly developed a graphical user interface (GUI) and operation panels so that the user can intuitively perform the necessary operations without cumbersome feeling. **Figure 2** shows the operation panels of this instrument. The left side of Fig. 2 shows the trackball for moving the specimen, the center of Fig. 2 shows the main operation panel, and the right side of Fig. 2 shows the panel for adjusting the specimen height (Z) and tilting the specimen. Although the number of knobs and switches is smaller compared with those of the operation panel of the conventional (S)TEM, the user can intuitively operate the instrument because appropriate functions are automatically assigned to these knobs and switches according to the state of the instrument.

Figure 3 shows the GUI of the instrument. The JEM-2800 GUI can display all the observation images such as (S)TEM and SEM images, set each observation condition, and display the operational status of each part of the JEM-2800 on a real-time basis. In addition, the user can operate the instrument under the environment of a bright room. Since the JEM-2800 enables you to simultaneously observe and record scanning images, such as STEM-BF image, STEM-DF image and SEM image, enhancement of throughput can be expected. Depending on the procedure of observation or analysis, it is sometimes required to frequently switch between TEM and STEM. In the JEM-2800, simply clicking the observation-mode switching buttons on the top left of the GUI enables you to easily switch the observation modes between TEM, STEM-BF, STEM-DF, SEM and Diffraction. In the case of switching image observation such as from TEM to

Table 1 Needs of STEM and TEM for users in the semiconductor industry.

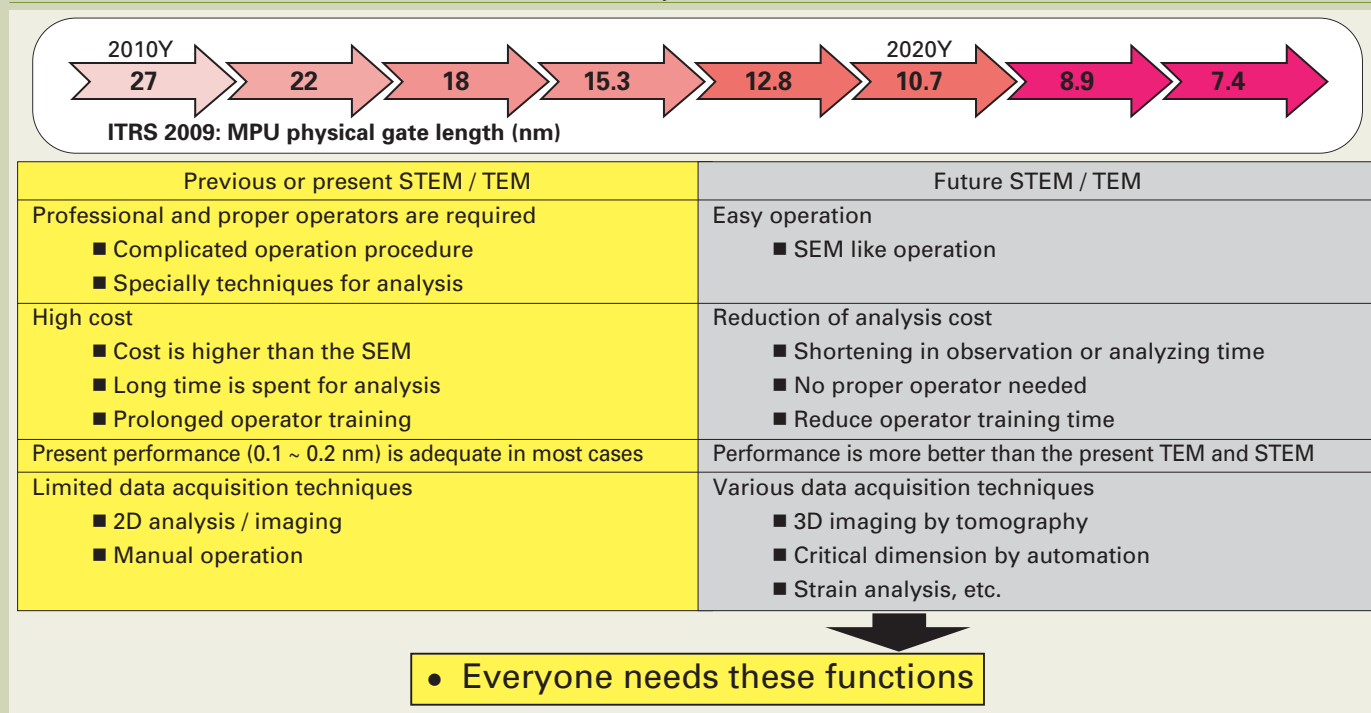


Fig. 1 External view of JEM-2800. Left-hand side of the figure is the microscope column in enclosure. Enclosure height is about 2.6 m. Right-hand side of the figure is an operation console. All operations are performed from the operation console.



Fig. 2 Operation panels of JEM-2800. Trackball panel, main operation panel and specimen height and tilt control panel are shown from the left-hand side. Main operation panel upper-side is used for alignment, and bottom-side is used for acquisition setting of images.

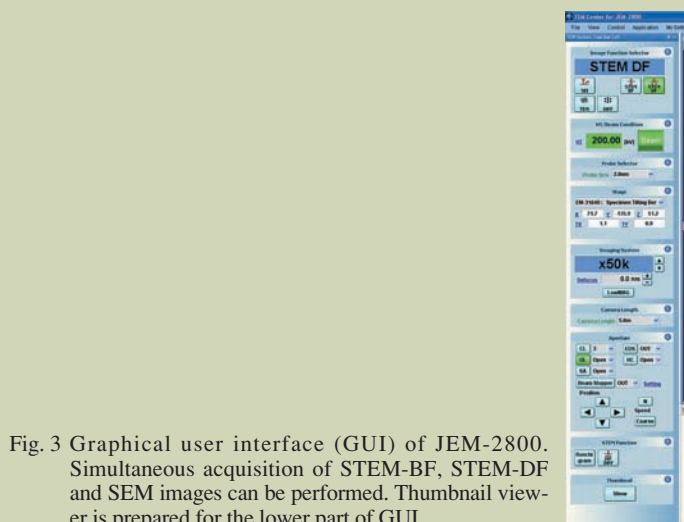


Fig. 3 Graphical user interface (GUI) of JEM-2800. Simultaneous acquisition of STEM-BF, STEM-DF and SEM images can be performed. Thumbnail viewer is prepared for the lower part of GUI.

STEM, the observation mode changes in about 10 seconds while keeping the same magnification and the same field of view, thus you can continue the observation without requiring the time for re-searching the observation field of view due to the switching of the observation mode.

Automatic functions

When performing the observation of multiple fields of view, it is necessary to repeat the same operation procedure. **Figure 4** shows the general operation flow of a (S)TEM. The JEM-2800 is provided with automatic adjustment functions for frequently used operations, including brightness & contrast adjustment, alignment of the specimen orientation (zone axis), focusing and

astigmatism correction. Alignment of the specimen orientation is to align the (crystal) zone axis of the specimen with respect to the presently observed field of view. Furthermore, automatic focusing and automatic astigmatism correction can be executed irrespective of the observation mode of TEM or STEM. These automatic functions help to greatly reduce cumbersome operations of the user and variations of the observation conditions.

Remote operation

There is also a need to observe an image or perform discussion while observing the image from a place different from the installation site of the (S)TEM. The JEM-2800 is provided with an optional remote operation function that

enables you to operate the instrument from a remote site. This optional function offers the same GUI and operation panel even in the remote site. If you arrange the respective operation panels and PCs in the (S)TEM main unit and the remote site, you can also perform the image observation and analysis in real time while performing discussion.

Navigation system JEM-Navi

A user who is unaccustomed to the (S)TEM operation often becomes confused on the operation procedure. In order to guide the user without miss-operations, the navigation system is built in the JEM-2800. **Figure 5** shows the example screen of the JEM-Navi. When the user reads the operation procedure and clicks a

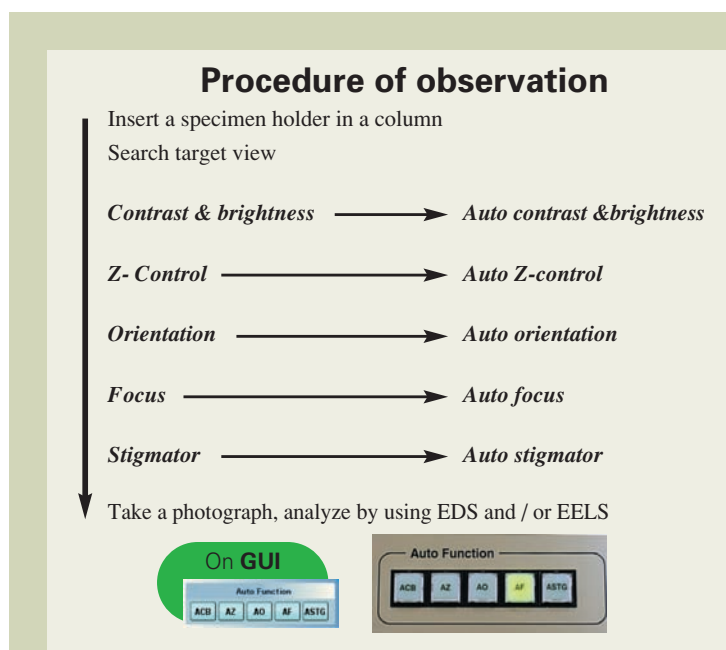


Fig. 4 General operation flow of TEM and STEM. Almost operation procedures can be performed automatically.

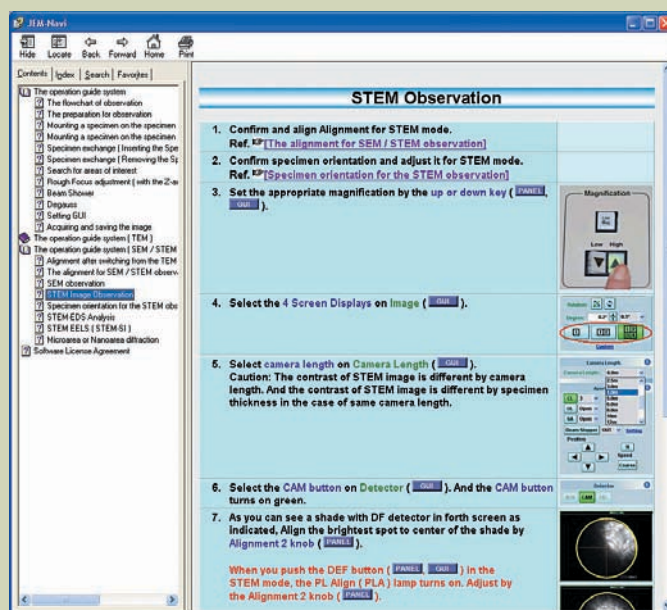


Fig. 5 Example screen of the operation navigator (JEM-Navi). Corresponding switch of operation panel and / or the portion of GUI blinks by clicking the link button of the operation navigator.

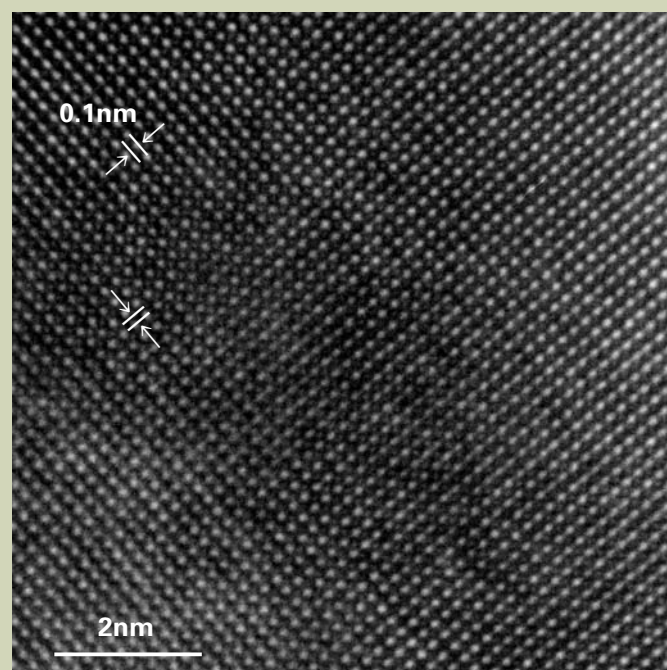


Fig. 6 High resolution TEM image of gold single crystal. Accelerating voltage is 200 kV.

link button in the document on the monitor screen, the software leads the user by blinking the lamp of switches or a portion of the screen that the user should operate. In the future, the main terms in the navigation document will be linked to the glossary; that is, clicking a term allows for displaying the explanation of the relevant term on the screen.

High-resolution image

The JEM-2800 enables you not only to provide high usability, but also to obtain high quality data. **Figure 6** shows a high-resolution TEM image of a gold single crystal acquired at an accelerating voltage of 200 kV. Lattice fringes with spacing of 0.1 nm are clearly visible in this image. **Figure 7** shows a high-resolution STEM image of a silicon single crystal that exhibits lattice fringes with spacing of 0.19 nm.

In recent years, there has been a high demand for high-resolution imaging even for soft materials such as porous material and macro-molecular material. The JEM-2800 meets this demand, enabling you to observe such a high-resolution image at an accelerating voltage of 100 kV even in the standard configuration. **Figure 8** shows a high-resolution TEM image of a gold single crystal acquired at an accelerating voltage of 100 kV. Lattice fringes with spacing of 0.14 nm can be visualized in this image.

On the other hand, there is also a high demand for observing an image with sufficiently good contrast. The JEM-2800 allows large change of the collection angles of the

STEM detector. **Figure 9** shows STEM images of a semiconductor device with different collection angles. They are a STEM-BF image, a STEM-LAADF image, and a STEM-HAADDF image from the left side of the figure. Many elements are used in the FET portion of recent semiconductor devices, and artificially controlled strain is introduced into the silicon substrate. The STEM-LAADF image can distinguish the elements different from the low-dielectric constant (Low-k) material portion since image contrast is different for each different element depending on the atomic number. Furthermore, in the silicon substrate portion, it is possible to clearly observe the portion into which the distortion is introduced with a contrast different from the surrounding portion free of distortion.

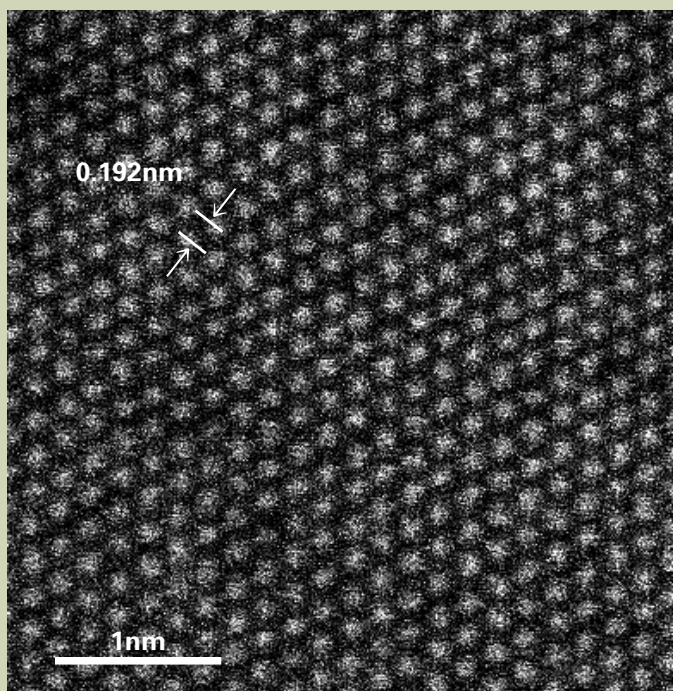


Fig. 7 High resolution STEM-DF image of silicon single crystal. Accelerating voltage is 200 kV.

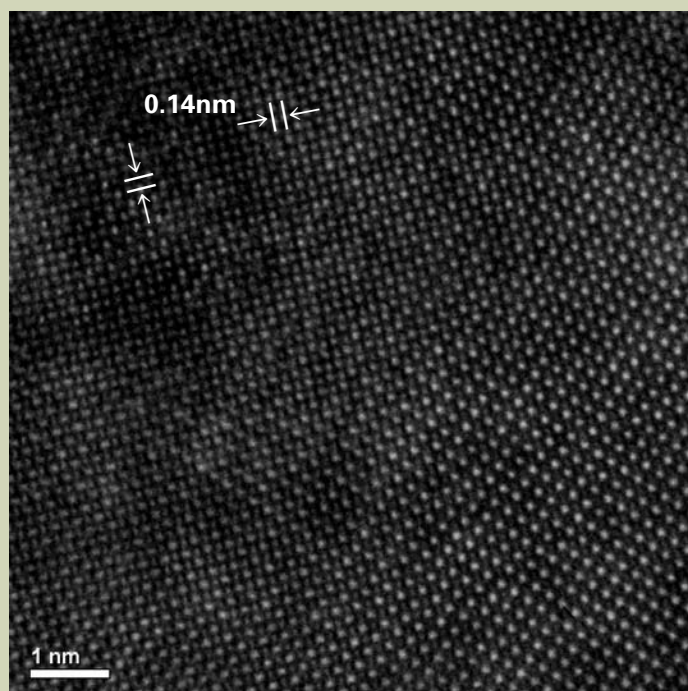


Fig. 8 High resolution TEM image of gold single crystal. Accelerating voltage is 100 kV.

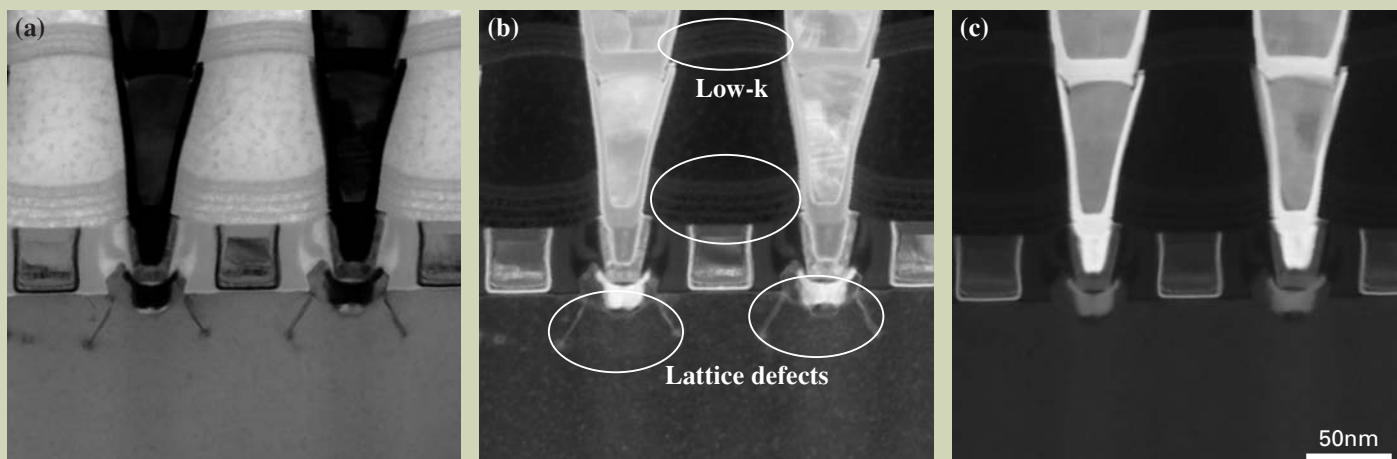


Fig. 9 STEM images of semiconductor device acquired by different collection angles. (a) < 11 mrad, (b) 14 to 63 mrad and (c) 46 to 208 mrad. Lattice defects and low-k layers are clearly observed in (a) STEM-BF image and (b) STEM-LAADF image.

High speed EDS analysis

One of the advantages to perform EDS analysis using a (S)TEM is that you can perform a high-resolution EDS analysis; in recent years, however, analysis speed-up is also requested. The JEM-2800 can install an SDD (silicon drift detector) of 100 mm² having a solid angle of 0.95 sr. With this installation, the instrument can provide detection sensitivity about as five or more times as that compared with a 50 mm² Si(Li) detector. In addition, as you can also change the illumination condition from a large current probe to a high-resolution probe, you can set the optimum analysis condition according to the size of the analysis area and the resolution required. **Figure 10** shows elemental mapping images of a semiconductor device acquired with EDS. It is seen that trace elements of hafnium and tantalum can be

detected. It is also found that spectral peaks of silicon and tungsten are clearly separated irrespective of their close characteristic X-ray energies to each other.

Furthermore, the JEM-2800 enables you to perform various analyses such as EELS, Tomography and local-distortion analysis in accordance with the needs of the user.

Data management system

Some companies also request to efficiently manage the observation images and analysis results. A data management system (ImageCenter) has been developed for the JEM-2800. **Figure 11** shows a schematic drawing of this data management system. The results of data acquired or analyzed by a (S)TEM are automatically unified in the

ImageCenter and managed in a lump. These data are read from each client to perform data processing. **Figure 12** shows the GUI displayed on a client site. Images and data can be searched using keywords such as photography date/time and photography conditions. After that, you can perform analysis or other tasks using the necessary software.

Summary

In the future, opportunities to use a (S)TEM will further increase in various fields. In such a circumstance, the JEM-2800 High Throughput Electron Microscope will contribute to more diversified fields since this instrument can provide all users with high performance and high throughput owing to its new various functions focused on high usability.

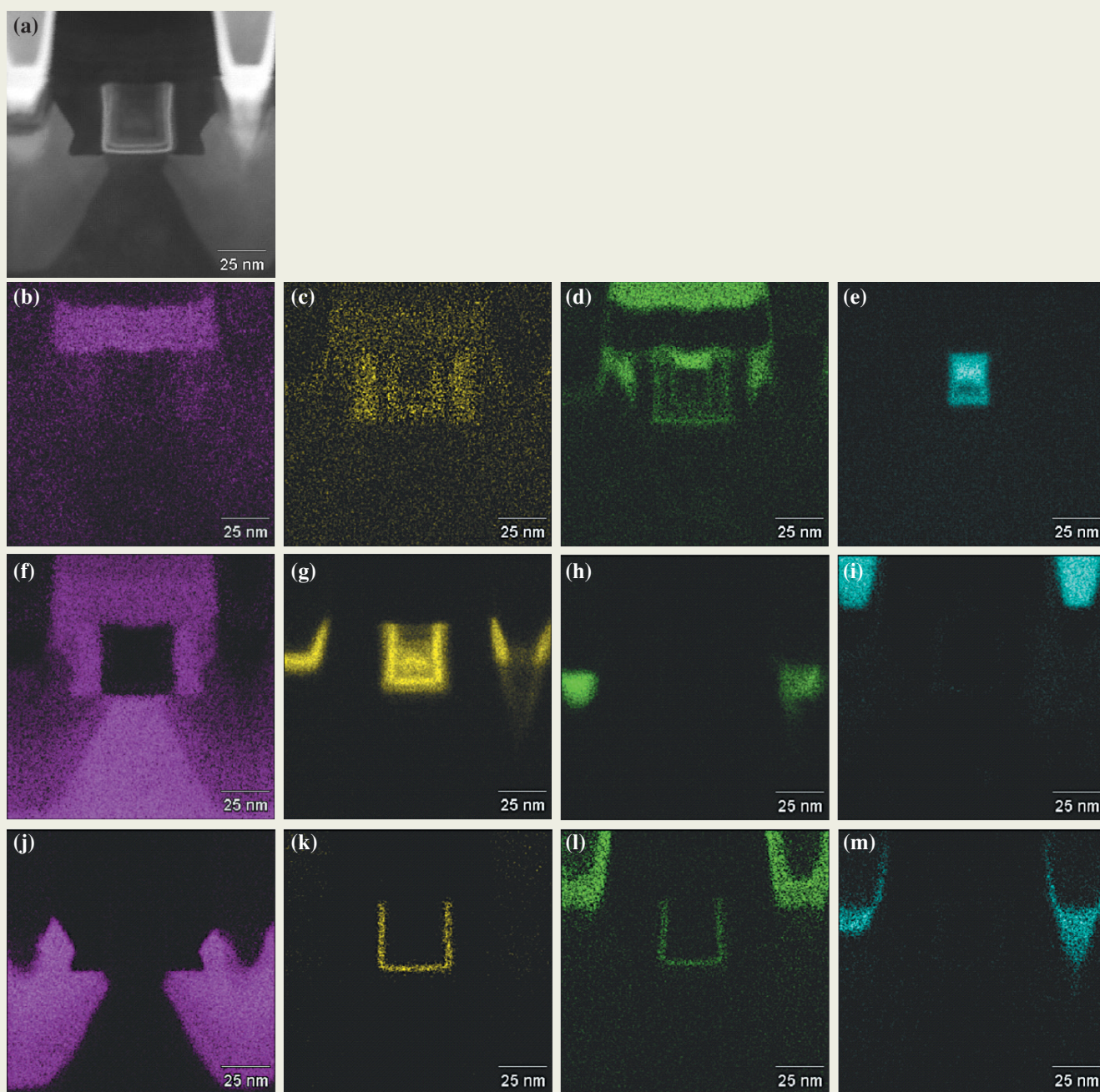


Fig. 10 EDS peak separated maps of 32 nm PMOS. (a) STEM-DF, (b) C-K, (c) N-K, (d) O-K, (e) Al-K, (f) Si-K, (g) Ti-K, (h) Ni-K, (i) Cu-K, (j) Ge-K, (k) Hf-L, (l) Ta-L and (m) W-L.

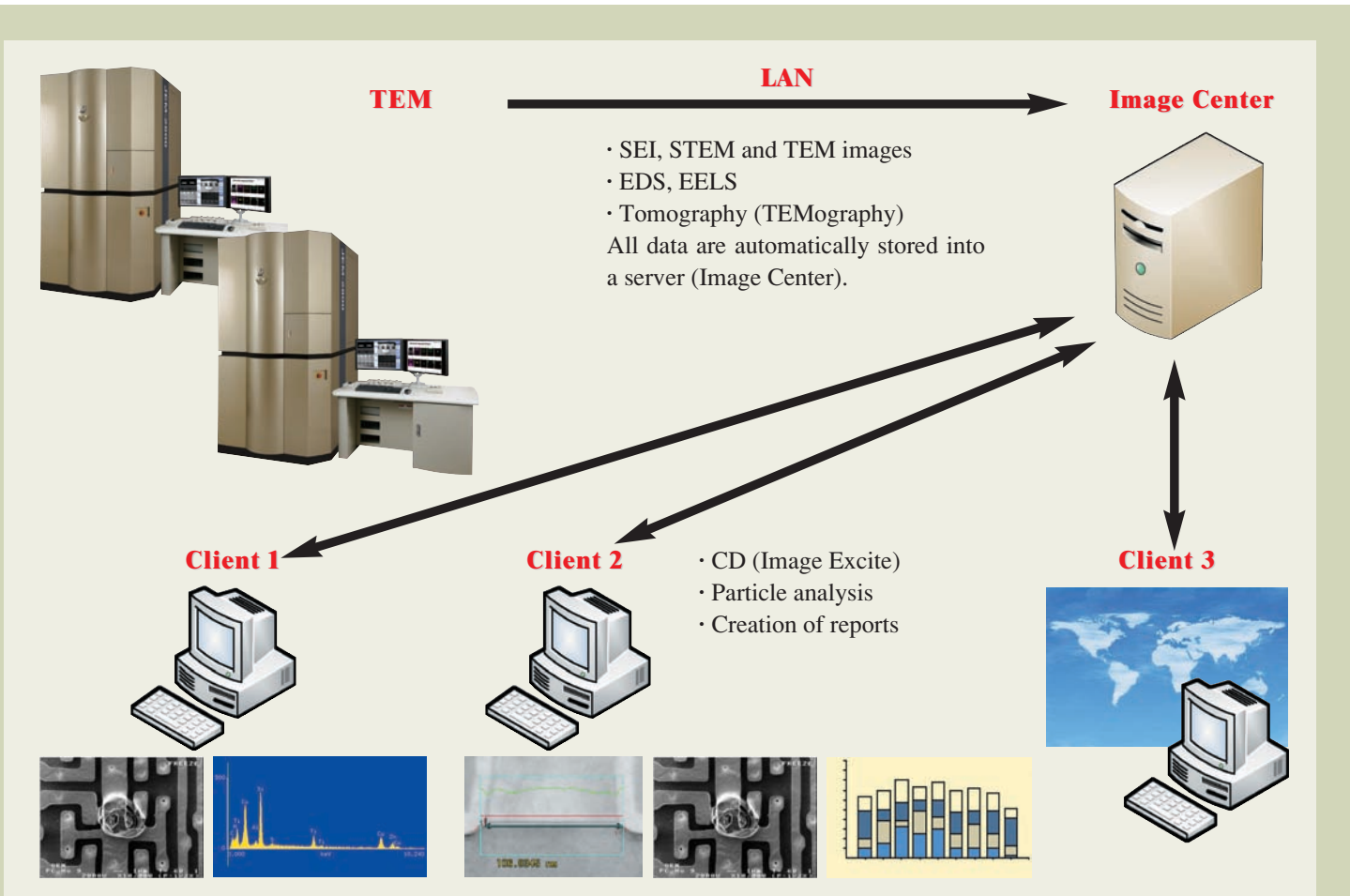


Fig. 11 Schematic drawing of TEM data management system. All the images and analysis data are stored in a file server (Image Center). Users can access Image Center from each client PC.

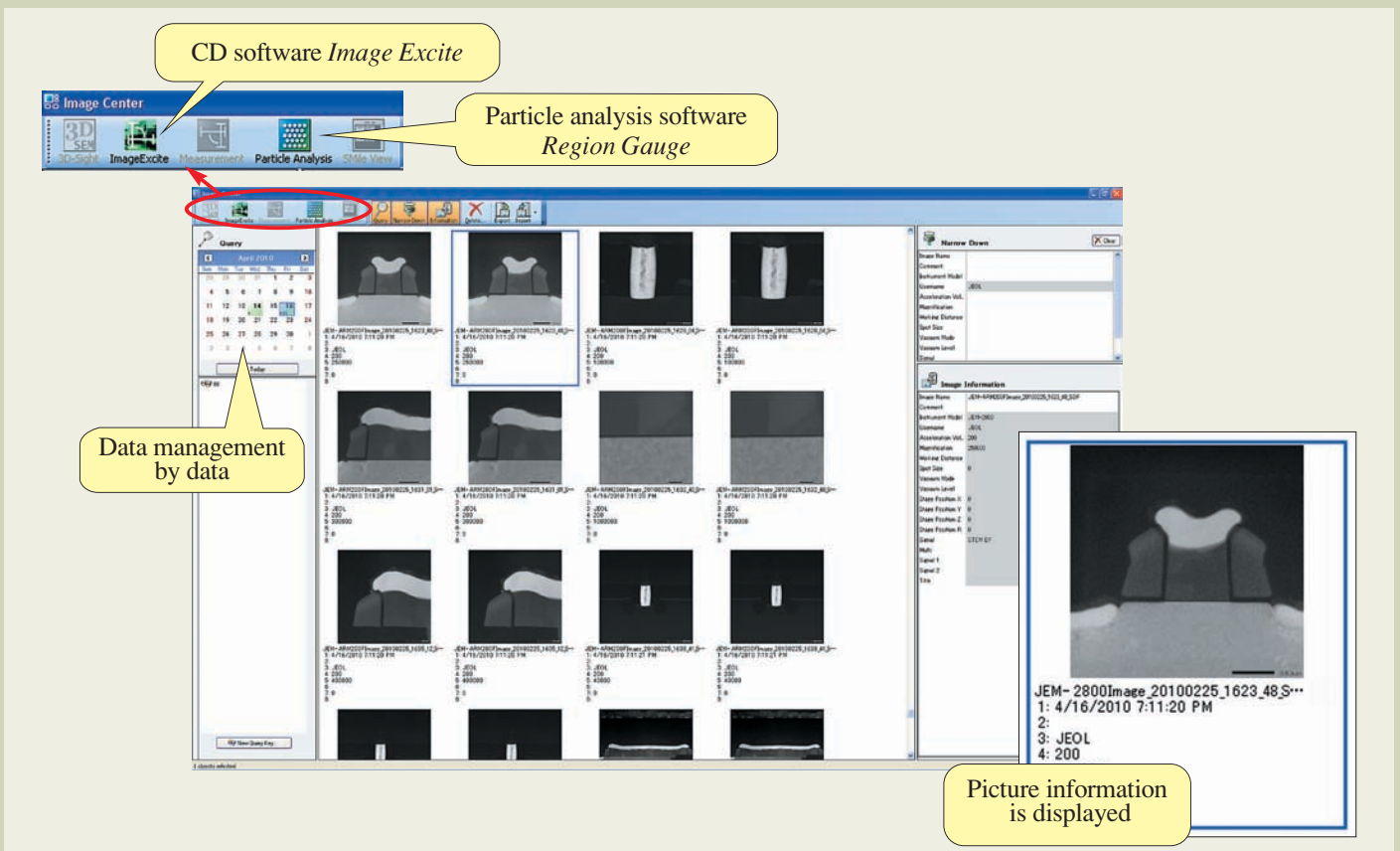


Fig. 12 Client GUI of Image Center. Stored images are shown. Data search can be performed by keywords such as date, specimen name, etc.

Introduction of New Products

High Throughput Electron Microscope JEM-2800

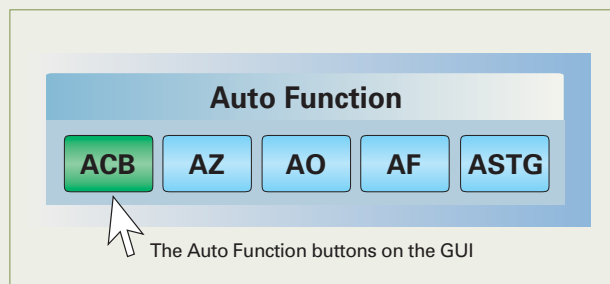
The JEM-2800 is a new transmission electron microscope that achieves nano-area analysis through Automation and Convenience, while being Easy-to-use so that expert results can be achieved by operators of any skill level.

The advanced electron optical system of the JEM-2800 makes it possible to perform high-resolution TEM and STEM imaging, EDS, EELS, tomography and in-situ observation on the same sample without sacrificing any of these capabilities. This next-generation TEM provides innovative solutions through its high performance and user-friendly operation.



Automation

The JEM-2800 can be operated using fully automatic functions for contrast, brightness, specimen Z position (height), crystal zone axis alignment, focus and astigmatism correction. Each function can be simply executed by pushing the corresponding button.



All - in - one

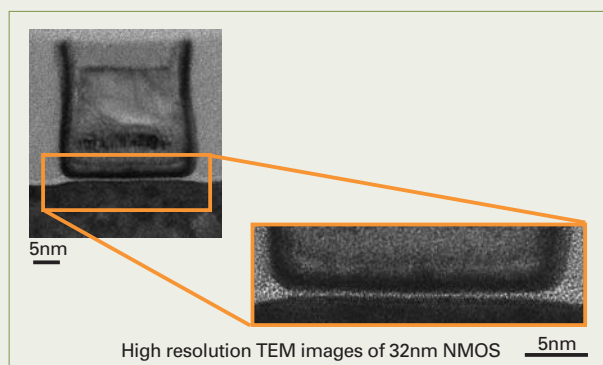
The JEM-2800 has the capability to observe TEM, STEM and SE (secondary electron) images along with electron diffraction patterns. In scanning mode BF-STEM, DF-STEM and SE images can be observed simultaneously. With the addition of EDS and EELS systems, microscope operation from initial search to final analysis can be performed seamlessly.

Quick Turn Around Time

These features combined enable for quick specimen observation and data collection, realizing quick turn around time between specimens.

Performance

The JEM-2800, with its new electron optic system, achieved both high resolution imaging and high speed analysis. A variety of preset beam data are available to insure the optimum settings for the sample or analyzing technique, enhancing the speed and accuracy of analysis. The microscope is image rotation free and positional shift of the area of view in the entire magnification range from low to high resolution imaging, and when the mode is switched between TEM and STEM. This includes rapid, easy imaging and analysis in all imaging modes.



JEM-Navi

The JEM-2800 incorporates a new operation navigation system, "JEM-Navi". This system makes the JEM-2800 easy to be used for operators with any level of skill.

Introduction of New Products

Thermal Field Emission Scanning Electron Microscope JSM-7800F

The new JSM-7800F has been developed to be an ultimate research tool suitable for institutions requiring a large variety of material research.

The newly developed super hybrid objective lens (SHL) provides the resolution of 0.8nm at 15kV and 1.2nm at 1kV. The SHL objective lens allows researchers to study magnetic samples at high magnification.

The in-lens thermal FEG produces an extremely stable probe current.

Addition to the observation of fine surface structures, the JSM-7800F enables researchers to analyze sub-micron structures with EDS, WDS, and EBSD.

Extreme resolution

The super hybrid objective lens provides extreme resolution of 0.8nm at 15kV and 1.2nm at 1kV.

With a very low incident electron energy, extremely fine surface structures are revealed.

The distribution of materials can be observed even at 0.5kV.

Fast and high precision analysis

The aperture angle optimizing lens keeps the electron probe small even at large probe currents.

A large probe current allows you to analyze samples quickly without sacrificing the precision and quality of the analyses. A variety of analytical systems including EDS, WDS, and EBSD are available.

Distortion free EBSD patterns are obtained for high precision crystal structure analysis.

High stability, consistency in acquired data

The in-lens thermal FEG produces an extremely stable probe current.

The Highest Performance is always available when you need it.

Results obtained by multiple users or on different days are consistent and easy to compare.

No limitation in specimens

The super hybrid lens is a field free lens at the analytical working distance.

Magnetic samples can be observed and analyzed at high magnification.

Non conductive samples are easily observed.

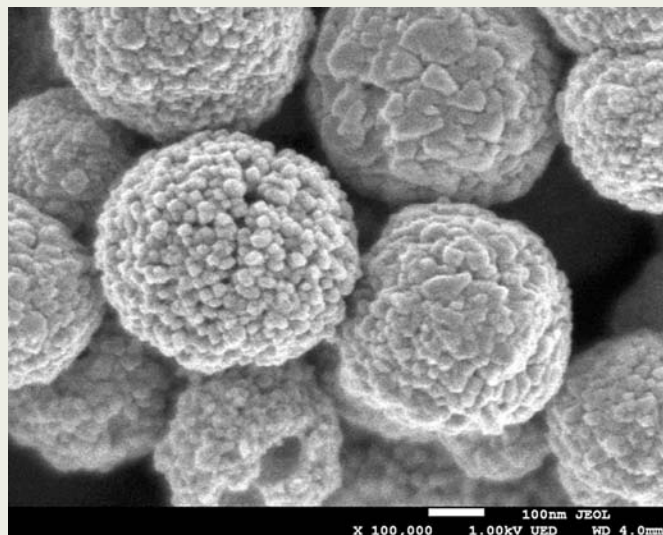
Come closer to the nano-world

The super hybrid objective lens brings you closer to the nano-world. The objective lens delivers superb high resolution even at extremely low electron energies. This is necessary to observe and analyze nano size structures.

The super hybrid objective lens can be used to observe and analyze magnetic materials at high magnifications.

Detectors

A variety of detectors can filter electrons from the specimen by energy and emission angle.



Fe₃O₄ nano-particle cluster

The SEM image courtesy of Dr. Takanari Togashi, Prof. Tadafumi Adschiri, Advanced Institute for Material Research, Tohoku University



Certain products in this brochure are controlled under the "Foreign Exchange and Foreign Trade Law" of Japan in compliance with international security export control. JEOL Ltd. must provide the Japanese Government with "End-user's Statement of Assurance" and "End-use Certificate" in order to obtain the export license needed for export from Japan. If the product to be exported is in this category, the end user will be asked to fill in these certificate forms.

JEOL JEOL Ltd.

1-2 Musashino 3-chome Akishima Tokyo 196-8558 Japan Sales Division Telephone:+81-42-528-3381 Facsimile:+81-42-528-3386

<http://www.jeol.com/>

ARGENTINA
COASIN S.A.C.I.y.F.
Virrey del Pino 4071,
1430 Buenos Aires
Argentina
Telephone: 54-11-4552-3185
Facsimile: 54-11-4555-3321

AUSTRALIA & NEW ZEALAND
JEOL(AUSTRALASIA) Pty.Ltd.
Suite 1, L2 18 Aquatic Drive
- Frenchs Forest NSW 2086
Australia
Telephone: 61-2-9451-3855
Facsimile: 61-2-9451-3822

AUSTRIA
LABCO GmbH
Dr.-Trittmel-Gasse 8,
A-3013 Pressbaum, Austria
Telephone: 43-2233-53838
Facsimile: 43-2233-53176

BANGLADESH
A.Q. CHOWDHURY SCIENCE & SYNERGY PVT. LTD.
House No. 12, Road No. 5A
Sector No. 11, Uttara Dhaka - 1230
Bangladesh
Telephone: 880-2-9980790, 8953450, 8953501
Facsimile: 880-2-8854428

BELGIUM
JEOL (EUROPE) B.V.
Planet II, Gebouw B
Leuvensesteenweg 542,
B-1930 Zaventem
Belgium
Telephone: 32-2-720-0560
Facsimile: 32-2-720-6134

BRAZIL
JEOL Brasil Instrumentos Cientificos Ltda.
Av. Itaberaba, 3563
02738-000 Sao Paulo, SP Brazil
Telephone: 55-11-3983 8144
Facsimile: 55-11-3983 8140

CANADA
JEOL CANADA, INC.
3275 Premier Rue #8,
St-Hubert, Quebec J3Y 8Y6, Canada
Telephone: 1-450-676-8776
Facsimile: 1-450-676-6694

CHILE
TECSIS LTDA.
Avenida Kennedy 5454 - Piso 5
Vitacura, Santiago, Chile
Telephone: 56-2-401-8520
Facsimile: 56-2-410-8541

CHINA
JEOL(BEIJING) CO., LTD.
Room B1010/1110, Wantong New World Plaza No. 2
Fuchengmenwai Street, Xicheng District,
Beijing 100037, P.R. China
Telephone: 86-10-6804-6321
Facsimile: 86-10-6804-6324

JEOL LTD., SHANGHAI OFFICE
Shanghai Equatorial Hotel Office Building 803,
65 Yanan Road West, Shanghai 200040, P.R. China
Telephone: 86-21-6248-4868/4487/4537/4404
Facsimile: 86-21-6248-4075

JEOL LTD., GUANG ZHOU OFFICE
N3104, World Trade Center Building
371-375, Huan Shi East-Road, Guang Zhou,
510095, P.R.China
Telephone: 86-20-8778-7848
Facsimile: 86-20-8778-4268

JEOL LTD., WUHAN OFFICE
Room 3216, World Trading Bldg,
686 Jiefang Street, Hankou, Wuhan, Hubei 430032
P.R.China
Telephone: 86-27-8544-8953
Facsimile: 86-27-8544-8695

JEOL LTD., CHENGDU OFFICE
1807A Zongfu Building,
NO. 45 Zhongfu Road, Chengdu, Sichuan, 610016
P.R. China
Telephone: 86-28-86622554
Facsimile: 86-28-86622564

CYPRUS
JEOL (EUROPE) SAS
Espace Claude Monet, 1 Allée de Giverny
78290, Croissy-sur-Seine, France
Telephone: 33-13015-3737
Facsimile: 33-13015-3747

EGYPT
JEOL SERVICE BUREAU
3rd Fl. Nile Center Bldg., Nawal Street,
Dokki, (Cairo), Egypt
Telephone: 20-2-3335-7220
Facsimile: 20-2-3338-4186

FRANCE
JEOL (EUROPE) SAS
Espace Claude Monet, 1 Allée de Giverny
78290, Croissy-sur-Seine, France
Telephone: 33-13015-3737
Facsimile: 33-13015-3747

GERMANY
JEOL (GERMANY) GmbH
Oskar-Von-Miller-Strasse 1a, 85386
Eching, Germany
Telephone: 49-8165-77346
Facsimile: 49-8165-77512

GREAT BRITAIN & IRELAND
JEOL (U.K.) LTD.
JEOL House, Silver Court, Watchmead,
Welwyn Garden City, Herts AL7 1LT, U.K.
Telephone: 44-1707-377117
Facsimile: 44-1707-373254

GREECE
N. ASTERIADIS S.A.
56-58, S. Trikoupi Str. P.O. Box 26140
GR-10022, Athens, Greece
Telephone: 30-1-823-5383
Facsimile: 30-1-823-9567

HONG KONG
FARMING LTD.
Unit 1009, 10/F, MLC Millennia Plaza
963 King's Road, North Point, Hong Kong
Telephone: 852-2815-7299
Facsimile: 852-2581-4635

INDIA
BLUE STAR LTD. (HQ: Mumbai)
Analytical Instruments Department,
Sahas' 41/2 Veer Savarkar Marg
Prabhadery Mumbai 400 025, India
Telephone: 91-22-6666-4000
Facsimile: 91-22-6666-4001

BLUE STAR LTD. (Delhi)
Analytical Instruments Department,
E-44/12 Okhla Industrial Area,
Phase-II, New Delhi 110 020, India
Telephone: 91-11-4149-4000
Facsimile: 91-11-4149-4005

BLUE STAR LTD. (Calcutta)
Analytical Instruments Department,
7, Hare Street Calcutta 700 001, India
Telephone: 91-33-2213-4133
Facsimile: 91-33-2213-4102

BLUE STAR LTD. (Chennai)
Analytical Instruments Department,
No. 46, Garuda Building,
Cathedral Road, Chennai 600 086, India
Telephone: 91-44-4244-4000
Facsimile: 91-44-4244-4190

INDONESIA
PT. TEKNOLABINDO Penta Perkasa
Komplek Gading Bukit Indah Blok I/11
Jl. Bukit Gading Raya Kelapa Gading Permai,
Jakarta 14240, Indonesia
Telephone: 62-21-45847057/58/59
Facsimile: 62-21-45842729

ITALY
JEOL (ITALIA) S.p.A.
Centro Direzionale Green Office
Via dei Tulipani, 1
20090 Pieve Emanuele (MI) Italy
Telephone: 39-02-9041431
Facsimile: 39-02-90414343

KOREA
JEOL KOREA LTD.
Dongwoo Bldg, 7F, 458-5, Gil-Dong,
Gangdong-Gu, Seoul, 134-010, Korea
Telephone: 82-2-511-5501
Facsimile: 82-2-511-2635

KUWAIT
Ashraf & CO. Ltd. W.L.L.
P.O.Box 3555 Safat 13036, Kuwait
Telephone: 965-1805151
Facsimile: 965-24335373

MALAYSIA
JEOL(MALAYSIA) SDN.BHD.(359011-M)
205, Block A, Mezzanine Floor,
Kelana Business Center,
97, Jalan SS 7/2, Kelana Jaya,
47301 Petaling Jaya, Selangor, Malaysia
Telephone: 60-3-7492-7722
Facsimile: 60-3-7492-7723

MEXICO
JEOL DE MEXICO S.A. DE C.V.
Av. Amsterdam #46 DEPS. 402
Col Hipodromo, 06100, Mexico D.F.
Mexico
Telephone: 52-5-55-211-4511
Facsimile: 52-5-55-211-0720

PAKISTAN (Karachi)
ANALYTICAL MEASURING SYSTEM (PVT) LTD.(AMS LTD.)
14-C Main Sehar Commercial Avenue Lane 4,
Khayaban-e-Sehar,
D.H.A-VII, Karachi-75500, Pakistan
Telephone: 92-21-35345531/35340747/35346057-8
Facsimile: 92-21-35345582

PANAMA
PROMED S.A.
Parque Industrial Costa del Este
Urbanizacion Costa del Este
Apartado 0816-01755, Panama, Panama
Telephone: 507-303-3100
Facsimile: 507-303-3115

PHILIPPINES
PHILAB INDUSTRIES INC.
7487 Bagtikan Street, SAV Makati,
1203 Metro, Manila Philippines
Telephone: 63-2-896-7218
Facsimile: 63-2-897-7732

PORTUGAL
Izasa Portugal Lda.
R. do Proletariado, 1
2790-138 CARNAXIDE, Portugal
Telephone: 351-21-424-73-00
Facsimile: 351-21-418-60-20

RUSSIA
JEOL LTD. Moscow Office
Krasnoproletarskaya Street, 16,
Bld. 2, Entrance 5, 127473, Moscow,
Russian Federation
Telephone: 7-495-748-7791
Facsimile: 7-495-748-7793

SAUDI ARABIA
ABDULREHMAN ALGOSAIBI G.T.C. (Riyadh)
King Abdulaziz Avenue,
P.O. Box 215, Riyadh 11411, Saudi Arabia
Telephone: 966-1-479-3000
Facsimile: 966-1-477-1374

SCANDINAVIA
SWEDEN
JEOL (Skandinaviska)AB
Hammarbacken 6A, Box 716, 191 27 Sollentuna
Sweden
Telephone: 46-8-28-2800
Facsimile: 46-8-29-1647

SERVICE & INFORMATION OFFICE
NORWAY
JEOL (Skandinaviska)AB
Lorenvangen 23, 0580 Oslo, NORWAY
Telephone: 47-2-2-64-7930
Facsimile: 47-2-2-65-0619

FINLAND
JEOL (Skandinaviska)AB
Ylakaupunkia 2, FIN-02360 Espoo, Finland
Telephone: 358-9-8129-0350
Facsimile: 358-9-8129-0351

SINGAPORE
JEOL ASIA PTE. LTD.
2 Corporation Road #01-12 Corporation Place
Singapore 618494
Telephone: 65-6565-9989
Facsimile: 65-6565-7552

SOUTH AFRICA
ADI Scientific (Pty) Ltd.
370 Angus Crescent,
Northlands Business Park, 29 Newmarket Road
Northridge, Randburg, Republic of South Africa
Telephone: 27-11-462-1363
Facsimile: 27-11-462-1466

SPAIN
IZASA S.A.
Argoneses, 13, 28100 Alcobendas,
(Poligono Industrial), Madrid, Spain
Telephone: 34-91-663-0500
Facsimile: 34-91-663-0545

SWITZERLAND
JEOL (GERMANY) GmbH
Oskar-Von-Miller-Strasse 1,
85386 Eching, Germany
Telephone: 49-8165-77346
Facsimile: 49-8165-77512

TAIWAN
JIE DONG CO., LTD.
7F, 112, Chung Hsiao East Road,
Section 1, Taipei, Taiwan 10023
Republic of China
Telephone: 886-2-2395-2978
Facsimile: 886-2-2322-4655

For Semiconductor Products:
JEOL TAIWAN SEMICONDUCTORS LTD.
11F-1, No. 346, Pei-Da Road, Hsin-Chu City 300,
Taiwan, Republic of China
Telephone: 886-3-523-8490
Facsimile: 886-3-523-8503

THAILAND
BECTHAJ BANGKOK EQUIPMENT & CHEMICAL CO., Ltd.
300 Phaholyothin Rd. Phayathai, Bangkok 10400,
Thailand
Telephone: 66-2-615-2929
Facsimile: 66-2-615-2350/2351

THE NETHERLANDS
JEOL (EUROPE) B.V.
Lireweg 4, NL-2153 PH Nieuw-Vennep,
The Netherlands
Telephone: 31-252-623500
Facsimile: 31-252-623501

TURKEY
TEKSER A.S.
Kayisdagi, Inonu Mah.Kartal Cad. No:55/3
34755 Atasehir / Istanbul, Turkey
Telephone: 90-216-5736740
Facsimile: 90-216-5736475

UAE
BUSINESS COMMUNICATIONS LLC. (Abu Dhabi)
P.O. Box 2534, Abu Dhabi UAE
Telephone: 971-2-6348495
Facsimile: 971-2-6316465

BUSINESS COMMUNICATIONS LLC. (Dubai)
P.O. Box 233, Dubai, UAE
Telephone: 971-4-2220186
Facsimile: 971-4-2236193

USA
JEOL USA, INC.
11 Dearborn Road, Peabody, MA 01960, U.S.A.
Telephone: 1-978-535-5900
Facsimile: 1-978-536-2205/2206

JEOL USA, INC. WEST OFFICE
5653 Stoneridge Drive Suite #110
Pleasanton, CA 94588, U.S.A.
Telephone: 1-925-737-1740
Facsimile: 1-925-737-1749

VENEZUELA
GOMSA Service and Supply C.A.
Urbanizacion Montalban III
- Residencias Don Andres - Piso 7 - Apartamento 74
Avenida 3, entre calles 7 y 6
Montalban, Caracas, Venezuela
Telephone: 58-212-443-4342
Facsimile: 58-212-443-4342

VIETNAM
TECHNICAL MATERIALS AND RESOURCES IMPORT-EXPORT JOINT STOCK
COMPANY(REXCO)
Hanoi Branch,
No. 13-Lot 12 Trung Yen, Trung Hoa Street, Cau Giay Dist, Hanoi, Vietnam
Telephone: 84-4-562-0516,17/562-0535
Facsimile: 84-4-853-2511